



**UNIVERSITY OF GAZIANTEP**

**130905**

**EFFECT OF NOISE ON MODE-LOCKED HYBRID SOLITON  
PULSE SOURCE**

**Ph. D. Thesis**

**SC. YÖS.  
BİLİMİN GELİŞTİRİLMESİNE**

**SUBMITTED TO**

**THE GRADUATE SCHOOL OF NATURAL AND APPLIED SCIENCES**

**IN**

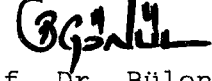
**ELECTRICAL & ELECTRONICS ENGINEERING**

**BY**

**NURAN DOGRU**

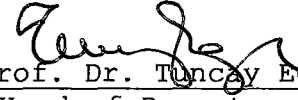
**May 2003**

Approval of the Graduate School of Natural and Applied Sciences



Prof. Dr. Bülent GÖNÜL  
Director

I certify that this thesis satisfies all the requirements as a thesis for the degree of Doctor of Philosophy.



Prof. Dr. Tuncay EGE  
Head of Department

This is to certify that we have read this thesis and that in our opinion it is fully adequate, in scope and quality, as a thesis for the degree of Doctor of Philosophy.



Prof. M. Sadettin ÖZYAZICI  
Supervisor

Examining Committee Members

Prof. Dr. Arif NACAROĞLU (Chairman)



Prof. Dr. M. Sadettin ÖZYAZICI



Prof. Dr. Engin TÜRE



Prof. Dr. Rauf MİRZABABAYEV



Assoc. Prof. Dr. Beşire GÖNÜL



## **ABSTRACT**

### **EFFECT OF NOISE ON MODE-LOCKED HYBRID SOLITON PULSE SOURCE**

**DOĞRU, Nuran**

**Ph. D. in Electrical and Electronics Engineering**

**Supervisor: Prof. Dr. M. Sadettin ÖZYAZICI**

**May 2003,120 pages**

The noise of hybrid soliton pulse source (HSPS) utilizing different fiber Bragg gratings (FBGs) such as uniform, Gaussian, linearly chirped uniform and linearly chirped Gaussian apodized are described by using electric field approach when HSPS is mode-locked. The HSPS system is made up of a multi-quantum well (MQW) semiconductor laser, a fiber and a FBG. The HSPS is modeled by a time-domain solution of the coupled-mode equations including spontaneous emission noise. These equations are converted into the transfer matrix form by using the piecewise-uniform approach. Relative intensity noise (RIN) is calculated using numerical solutions of these equations. Although transform-limited pulses over a wide tuning range around the fundamental mode-locking frequency are obtained from mode-locked HSPS with linearly chirped uniform and linearly chirped Gaussian apodized FBGs with low noise, mode-locked HSPS with uniform and Gaussian apodized FBGs can generate transform-limited pulses only over a limited tuning range. However, noise increases with increasing linewidth enhancement factor, gain saturation parameter and spontaneous coupling factor. A high noise level that generates a noise peak at the mode-locking frequency in the RIN spectrum makes the transform limited pulses unobtainable at the mode-locking frequency and therefore proper mode-locking range reduces. Noise is also extremely sensitive to the RF and DC currents. Carrier noise is important as spontaneous noise and inclusion of this noise source into the rate equations is necessary for accurate analysis of the noise. It is also found that RIN

reduction is possible for the mode-locked HSPS by selecting a suitable apodization function such as Gaussian and linear chirp rate.

**Keywords:** Hybrid soliton pulse source, mode-locked laser, fiber Bragg grating, multi-quantum well laser, relative intensity noise, spontaneous noise, carrier noise.



## ÖZ

### GÜRÜLTÜNÜN MOD-KİLİTLİ KARIŞIK SOLİTON DARBE KAYNAĞI ÜZERİNE ETKİSİ

**DOĞRU, Nuran**

**Doktora Tezi, Elektrik ve Elektronik Mühendisliği Bölümü**

**Tez Yöneticisi: Prof. Dr. M. Sadettin ÖZYAZICI**

**Mayıs 2003, 120 sayfa**

Düzensiz, Gaussian, doğrusal azalan düzensiz ve doğrusal azalan Gaussian pozlu gibi değişik fiber Bragg ızgara (FBG) kullanan karışık soliton darbe kaynağının (HSPS) mod-kilitli durumda gürültüsü elektrik alan yaklaşımı kullanılarak tanımlandı. HSPS bir çoklu kuantum kuyusu (MQW) yarı iletken laser, bir fiber dış kovuk ve bir FBG den meydana gelmektedir. HSPS spontane gürültüyü de içeren çiftli dalga denklemlerinin zaman domeninde çözümüyle modellendi. Bu denklemler parçalı doğrusal yaklaşımla aktarma matrisi şekline dönüştürüldü. Bağlı şiddet gürültüsü (RIN) bu denklemlerin sayısal çözümüyle hesaplandı. Doğrusal azalan adımli düzensiz ve doğrusal azalan adımli Gaussian pozlu FBGs kullanan HSPS ile düşük gürültüde geniş bir frekans aralığında çevirili-sınırlı darbeler elde edilmesine rağmen, mod-kilitli düzensiz ve Gaussian pozlu FBGs HSPS sadece sınırlı bir frekans aralığında çeviri-sınırlı darbeler üretebilir. Bununla birlikte, gürültü çizgigenişliği artma (linewidth enhancement) faktörü, kazanç doyuma (gain saturation) faktörü ve spontane kavrama (spontaneous coupling) faktörünün artmasıyla artmıştır. RIN spektrumunda, yüksek gürültü seviyesi çeviri-sınırlı darbelerin elde edilemeyeceği mod-kilitleme frekansında bir gürültü tepesi üretir ve bundan dolayı uygun mod-kilitleme aralığı azalır. Gürültü bir de aşırı derecede RF ve DC akımlarına duyarlıdır. Taşıyıcı gürültü spontane gürültü kadar önemlidir ve bu gürültünün oran denklemlerine dahil edilmesi gürültünün doğru analizi için gereklidir. Ayrıca,

Gaussian ve dođrusal azalan oranı gibi uygun pozlandırma fonksiyonlarını seçerek mod-kilitli HSPS ile RIN azaltılmasının mümkün olduđu bulundu.

**Anahtar kelimeler:** Karışık soliton darbe kaynađı, mod-kilitli laser, fiber Bragg ızgara, çoklu kuantum kırıy laseri, bađıl řiddet gürültüsü, spontane gürültü, taşıyıcı gürültü.

**Y.C. YÜKSEKÖĐRETİM BÜROLU  
BİRKÜMANTASYON MERKEZİ**

## **ACKNOWLEDGEMENTS**

In particular I am grateful to my supervisor Prof. Dr. M. Sadettin Özyazıcı for his guidance, suggestions and help during preparation of this work.

I would also like to thank Dr. Muhittin Sayın for his continuous support and help.



## TABLE OF CONTENTS

<b>ABSTRACT.....</b>	<b>iii</b>
<b>ÖZ.....</b>	<b>v</b>
<b>ACKNOWLEDGEMENTS.....</b>	<b>vii</b>
<b>LIST OF FIGURES.....</b>	<b>xi</b>
<b>LIST OF TABLES.....</b>	<b>xix</b>
<b>LIST OF SYMBOLS.....</b>	<b>xx</b>
<b>1. INTRODUCTION.....</b>	<b>1</b>
<b>2. MODEL OF FIBER BRAGG GRATING (FBG).....</b>	<b>7</b>
2.1 Introduction.....	7
2.2 Derivations of Coupled-Mode Equations.....	12
2.2.1 Model of Uniform FBG.....	12
2.2.2 Model of Chirped FBG.....	14
2.2.3 Model of Apodized FBG.....	17
2.3 Solutions of Coupled-Mode Equations.....	19
<b>3. RESULTS OF THE FIBER BRAGG GRATING MODEL.....</b>	<b>23</b>
3.1 Introduction.....	23
3.2 Design of FBG with Desired Peak Reflectivity.....	24
3.2.1 Uniform FBGs.....	24
3.2.2 Linearly Chirped Uniform FBGs.....	26
3.2.3 Gaussian Apodized FBGs.....	28
3.2.4 Linearly Chirped Gaussian apodized FBGs.....	29
3.3 Conclusions.....	31



<b>4. MODELING OF HYBRID SOLITON PULSE SOURCE (HSPS).....</b>	<b>32</b>
4.1 Introduction.....	32
4.2 Mode-Locked Lasers.....	35
4.3 Structure of the HSPS.....	40
4.4 Laser Diode Model.....	41
4.4.1 Nonradiative Recombination.....	42
4.4.2 Radiative Recombination and Spontaneous Emission.....	44
4.4.3 Carrier Rate Equations.....	44
4.4.4 Carrier Induced Refractive Index Change.....	45
4.5 Fiber Model.....	46
4.6 Grating Model.....	47
4.7 Laser-Fiber Interface.....	48
4.8 Boundary Conditions.....	50
<b>5. SPONTANEOUS AND CARRIER NOISE IN MODE-LOCKED HSPS....</b>	<b>51</b>
5.1 Introduction.....	51
5.2 Noise in the Laser .....	53
5.2.1 Spontaneous Emission Noise.....	53
5.2.2 Carrier Noise.....	55
5.3 Relative Intensity Noise.....	56
5.4 Mode-Locked HSPS Results for Different FBG Types.....	57
5.4.1 Output of HSPS for Linearly Chirped Gaussian Apodized FBG.....	57
5.4.2 Output of HSPS for Linearly Chirped Uniform FBG.....	60
5.4.3 Output of HSPS for Gaussian Apodized FBG.....	62
5.4.4 Output of HSPS for Uniform FBG.....	64
5.5 Conclusions.....	67
<b>6. RELATIVE INTENSITY NOISE (RIN) OF HSPS.....</b>	<b>68</b>
6.1 Introduction.....	68
6.2 Relative Intensity Noise (RIN) of HSPS.....	68
6.2.1 RIN of HSPS for Linearly Chirped Gaussian Apodized FBG...	68
6.2.2 RIN of HSPS for Linearly Chirped Uniform FBG.....	69
6.2.3 RIN of HSPS for Gaussian Apodized FBG.....	70

6.2.4	RIN of HSPS for Uniform FBG.....	71
6.3	Effects of RF and DC Currents on RIN of HSPS.....	73
6.3.1	Effects of RF and DC Currents on RIN of HSPS Utilizing Linearly Chirped Gaussian Apodized FBG.....	73
6.3.2	Effects of RF and DC Currents on RIN of HSPS Utilizing Linearly Chirped Uniform FBG.....	76
6.3.3	Effects of RF and DC Currents on RIN of HSPS Utilizing Gaussian Apodized FBG.....	78
6.3.4	Effects of RF and DC Currents on RIN of HSPS Utilizing Uniform FBG.....	81
6.4	The Important Noise Parameters.....	84
6.4.1	Linewidth Enhancement Factor.....	84
6.4.2	Gain Compression Factor.....	90
6.4.3	Spontaneous Coupling Factor.....	95
6.5	RIN Reduction in Mode-Locked HSPS.....	101
6.6	Conclusions.....	105
<b>7.</b>	<b>SUMMARY, CONCLUSIONS AND FUTURE WORK.....</b>	<b>106</b>
7.1	Summary.....	106
7.2	Conclusions.....	107
7.3	Future Work.....	109
	<b>REFERENCES.....</b>	<b>110</b>
	<b>VITA.....</b>	<b>117</b>

## LIST OF FIGURES

Figure 2.1. The transverse holographic method for writing fiber gratings.....	9
Figure 2.2. Refractive index variation of uniform FBG (average is $n_{co}=1.46$ ).....	13
Figure 2.3. Refractive index variation of chirped FBG (average is $n_{co}=1.46$ ).....	15
Figure 2.4. Refractive index variation of Gaussian apodized FBG a) Uniform pitch, b) linearly chirped (minimum level is $n_{co}=1.46$ , $m=1$ for both).....	19
Figure 3.1. Reflectivity and group delay characteristics for uniform FBG with 0.5 peak reflectivity.....	25
Figure 3.2. Reflectivity and phase characteristics for uniform FBG with 0.5 peak reflectivity.....	25
Figure 3.3. Reflectivity and group delay characteristics for uniform FBG with 0.99 peak reflectivity.....	26
Figure 3.4. Reflectivity, phase and group delay characteristics for linearly chirped uniform FBG with 0.5 peak reflectivity.....	27
Figure 3.5. Reflectivity, phase and group delay characteristics for linearly chirped uniform FBG with 0.99 peak reflectivity.....	27
Figure 3.6. Reflectivity, phase and group delay characteristics for Gaussian apodized FBG with 0.5 peak reflectivity.....	28
Figure 3.7. Reflectivity, phase and group delay characteristics for Gaussian apodized FBG with 0.99 peak reflectivity.....	29
Figure 3.8. Reflectivity, phase and group delay characteristics for linearly chirped Gaussian apodized FBG with 0.5 peak reflectivity.....	30

<b>Figure 3.9. Reflectivity, phase and group delay characteristics for linearly chirped Gaussian apodized FBG with 0.99 peak reflectivity.....</b>	<b>31</b>
<b>Figure 4.1. Energy level diagram illustrating (a) absorption, (b) spontaneous emission and (c) stimulated emission.....</b>	<b>33</b>
<b>Figure 4.2. Light output-current characteristic of an ideal semiconductor laser.....</b>	<b>34</b>
<b>Figure 4.3. The composite semiconductor laser cavity.....</b>	<b>37</b>
<b>Figure 4.4. Schematic of HSPS.....</b>	<b>40</b>
<b>Figure 4.5. Physical model of the laser-fiber interface.....</b>	<b>48</b>
<b>Figure 4.6. Section model of the laser-fiber interface and field reflections.....</b>	<b>49</b>
<b>Figure 5.1. Noise diagram in laser.....</b>	<b>54</b>
<b>Figure 5.2. Output intensity and field spectrum of mode-locked HSPS for linearly chirped Gaussian apodized FBG without noise at the mode-locking frequency of 2.5 GHz.....</b>	<b>58</b>
<b>Figure 5.3. Output intensity and field spectrum of mode-locked HSPS for linearly chirped Gaussian apodized FBG with spontaneous noise at the mode-locking frequency of 2.5 GHz.....</b>	<b>58</b>
<b>Figure 5.4. Output intensity and field spectrum of mode-locked HSPS for linearly chirped Gaussian apodized FBG with carrier noise at the mode-locking frequency of 2.5 GHz.....</b>	<b>59</b>
<b>Figure 5.5. Output intensity and field spectrum of mode-locked HSPS for linearly chirped Gaussian apodized FBG with spontaneous and carrier noise at the mode-locking frequency of 2.5 GHz.....</b>	<b>59</b>
<b>Figure 5.6. Output intensity and field spectrum of mode-locked HSPS for linearly chirped uniform FBG without noise at the mode-locking frequency of 2.5 GHz.....</b>	<b>60</b>

Figure 5.7. Output intensity and field spectrum of mode-locked HSPS for linearly chirped uniform FBG with spontaneous noise at the mode-locking frequency of 2.5 GHz.....	61
Figure 5.8. Output intensity and field spectrum of mode-locked HSPS for linearly chirped uniform FBG with carrier noise at the mode-locking frequency of 2.5 GHz.....	61
Figure 5.9. Output intensity and field spectrum of mode-locked HSPS for linearly chirped uniform FBG with spontaneous and carrier noise at the mode-locking frequency of 2.5 GHz.....	62
Figure 5.10. Output intensity and field spectrum of mode-locked HSPS for Gaussian apodized FBG without noise at the mode-locking frequency of 2.1 GHz.....	62
Figure 5.11. Output intensity and field spectrum of mode-locked HSPS for Gaussian apodized FBG with spontaneous noise at the mode-locking frequency of 2.1 GHz.....	63
Figure 5.12. Output intensity and field spectrum of mode-locked HSPS for Gaussian apodized FBG with carrier noise at the mode-locking frequency of 2.1 GHz.....	63
Figure 5.13. Output intensity and field spectrum of mode-locked HSPS for Gaussian apodized FBG with spontaneous and carrier noise at at mode-locking frequency of 2.1 GHz.....	64
Figure 5.14. Output intensity and field spectrum of mode-locked HSPS for uniform FBG without noise at the mode-locking frequency of 2.6 GHz.....	65
Figure 5.15. Output intensity and field spectrum of mode-locked HSPS for uniform FBG with spontaneous noise at the mode-locking frequency of 2.6 GHz.....	65
Figure 5.16. Output intensity and field spectrum of mode-locked HSPS for	

uniform FBG with carrier noise at the mode-locking frequency of 2.7 GHz.....	66
Figure 5.17. Output intensity and field spectrum of mode-locked HSPS for uniform FBG with spontaneous and carrier noise at the mode-locking frequency of 2.6 GHz.....	66
Figure 6.1. RIN spectrums of HSPS for linearly chirped Gaussian apodized FBG.....	69
Figure 6.2. RIN spectrums of HSPS for linearly chirped uniform FBG.....	70
Figure 6.3. RIN spectrums of HSPS for Gaussian apodized FBG.....	71
Figure 6.4. RIN spectrums of HSPS for uniform FBG.....	72
Figure 6.5. RIN spectrums of HSPS for linearly chirped Gaussian apodized FBG including spontaneous noise with different RF current for a DC current of 6 mA.....	73
Figure 6.6. RIN spectrums of HSPS for linearly chirped Gaussian apodized FBG including spontaneous and carrier noise with different RF current for a DC current of 6 mA.....	74
Figure 6.7. RIN spectrums of HSPS for linearly chirped Gaussian apodized FBG including spontaneous noise with different DC current for a RF current of 20 mA.....	75
Figure 6.8. RIN spectrums of HSPS for linearly chirped Gaussian apodized FBG including spontaneous and carrier noise with different DC current for a RF current of 20 mA.....	75
Figure 6.9. RIN spectrums of HSPS for linearly chirped uniform FBG including spontaneous noise with different RF current for a DC current of 6 mA.....	76
Figure 6.10. RIN spectrums of HSPS for linearly chirped uniform FBG including spontaneous and carrier noise with different RF current	

for a DC current of 6 mA.....	77
<b>Figure 6.11. RIN spectrums of HSPS for linearly chirped uniform FBG including spontaneous noise with different DC current for a RF current of 20 mA.....</b>	<b>77</b>
<b>Figure 6.12. RIN spectrums of HSPS for linearly chirped uniform FBG including spontaneous and carrier noise with different DC current for a RF current of 20 mA.....</b>	<b>78</b>
<b>Figure 6.13. RIN spectrums of HSPS for Gaussian apodized FBG including spontaneous noise with different RF current for a DC current of 6 mA.....</b>	<b>79</b>
<b>Figure 6.14. RIN spectrums of HSPS for Gaussian apodized FBG including spontaneous and carrier noise with different RF current for a DC current of 6 mA.....</b>	<b>79</b>
<b>Figure 6.15. RIN spectrums of HSPS for Gaussian apodized FBG including spontaneous noise with different DC current for a RF current of 20 mA.....</b>	<b>80</b>
<b>Figure 6.16. RIN spectrums of HSPS for Gaussian apodized FBG including spontaneous and carrier noise with different DC current for a RF current of 20 mA.....</b>	<b>80</b>
<b>Figure 6.17. RIN spectrums of HSPS for uniform FBG including spontaneous noise with different RF current for a DC current of 6 mA.....</b>	<b>81</b>
<b>Figure 6.18. RIN spectrums of HSPS for uniform FBG including spontaneous and carrier noise with different RF current for a DC current of 6 mA... </b>	<b>82</b>
<b>Figure 6.19. RIN spectrums of HSPS for uniform FBG including spontaneous noise with different DC current for a RF current of 20 mA.....</b>	<b>83</b>
<b>Figure 6.20. RIN spectrums of HSPS for uniform FBG including spontaneous and carrier noise with different DC current for a RF current of 20 mA.....</b>	<b>83</b>

Figure 6.21. RIN spectrum of HSPS with linearly chirped Gaussian apodized FBG for different $\alpha_h$ with spontaneous noise.....	85
Figure 6.22. RIN spectrum of HSPS with linearly chirped Gaussian apodized FBG for different $\alpha_h$ with both spontaneous and carrier noise.....	86
Figure 6.23. RIN spectrum of HSPS with linearly chirped uniform FBG for different $\alpha_h$ with spontaneous noise.....	86
Figure 6.24. RIN spectrum of HSPS with linearly chirped uniform FBG for different $\alpha_h$ with both spontaneous and carrier noise.....	87
Figure 6.25. RIN spectrum of HSPS with Gaussian apodized FBG for different $\alpha_h$ with spontaneous noise.....	88
Figure 6.26. RIN spectrum of HSPS with Gaussian apodized FBG for different $\alpha_h$ with spontaneous and carrier noise.....	88
Figure 6.27. RIN spectrum of HSPS with uniform FBG for different $\alpha_h$ with spontaneous noise.....	89
Figure 6.28. RIN spectrum of HSPS with uniform FBG for different $\alpha_h$ with both spontaneous and carrier noise.....	89
Figure 6.29. RIN spectrum of HSPS with linearly chirped Gaussian apodized FBG for different $\epsilon$ with spontaneous noise.....	90
Figure 6.30. RIN spectrum of HSPS with linearly chirped Gaussian apodized FBG for different $\epsilon$ with both spontaneous and carrier noise.....	91
Figure 6.31. RIN spectrum of HSPS with linearly chirped uniform FBG for different $\epsilon$ with spontaneous noise.....	92
Figure 6.32. RIN spectrum of HSPS with linearly chirped uniform FBG for different $\epsilon$ with both spontaneous and carrier noise.....	92
Figure 6.33. RIN spectrum of HSPS with Gaussian apodized FBG for	



different $\epsilon$ with spontaneous noise.....	93
Figure 6.34. RIN spectrum of HSPS with Gaussian apodized FBG for different $\epsilon$ with spontaneous and carrier noise.....	93
Figure 6.35. RIN spectrum of HSPS with uniform FBG for different $\epsilon$ with spontaneous noise.....	94
Figure 6.36. RIN spectrum of HSPS with uniform FBG for different $\epsilon$ with both spontaneous and carrier noise.....	94
Figure 6.37. RIN spectrum of HSPS with linearly chirped Gaussian apodized FBG for different $\beta_{sp}$ with spontaneous noise.....	95
Figure 6.38. RIN spectrum of HSPS with linearly chirped Gaussian apodized FBG for different $\beta_{sp}$ with both spontaneous and carrier noise.....	96
Figure 6.39. RIN spectrum of HSPS with linearly chirped uniform FBG for different $\beta_{sp}$ with spontaneous noise.....	97
Figure 6.40. RIN spectrum of HSPS with linearly chirped uniform FBG for different $\beta_{sp}$ with both spontaneous and carrier noise.....	97
Figure 6.41. RIN spectrum of HSPS with Gaussian apodized FBG for different $\beta_{sp}$ with spontaneous noise.....	99
Figure 6.42. RIN spectrum of HSPS with Gaussian apodized FBG for different $\beta_{sp}$ with spontaneous and carrier noise.....	99
Figure 6.43. RIN spectrum of HSPS with uniform FBG for different $\beta_{sp}$ with spontaneous noise.....	100
Figure 6.44. RIN spectrum of HSPS with uniform FBG for different $\beta_{sp}$ with both spontaneous and carrier noise.....	100
Figure 6.45. RIN spectrum of HSPS with low spontaneous noise ( $\beta_{sp}=5 \times 10^{-5}$ ).....	102
Figure 6.46. RIN spectrum of HSPS with high spontaneous noise	

$(\beta_{sp}=20 \times 10^{-5})$ .....103

Figure 6.47. RIN spectrum of HSPS with high noise including spontaneous  
and carrier noise ( $\beta_{sp}=20 \times 10^{-5}$ ).....104



## LIST OF TABLES

Table 3.1. Standard parameters for the FBG model.....	23
Table 5.1. Standard parameters for the HSPS mode-locking program.....	52
Table 6.1. Effects of varying $\alpha_h$ for linearly chirped Gaussian apodized FBG.....	84
Table 6.2. Effects of varying $\alpha_h$ for linearly chirped uniform FBG.....	84
Table 6.3. Effects of varying $\beta_{sp}$ for linearly chirped Gaussian apodized FBG.....	95
Table 6.4. Effects of varying $\beta_{sp}$ for linearly chirped uniform FBG at the mode-locking frequency of 2.5 GHz.....	98
Table 6.5. Effects of varying $\beta_{sp}$ for linearly chirped uniform FBG at the mode-locking frequency of 2.4 GHz.....	98

## LIST OF SYMBOLS

<b>AR</b>	<b>Anti-reflection coating</b>
<b>HR</b>	<b>High reflectivity coating</b>
$a_0$	<b>Differential gain</b>
$\alpha$	<b>Loss</b>
$\alpha_{int}$	<b>Total internal loss</b>
$\alpha_c$	<b>Cladding loss</b>
$\alpha_h$	<b>Linewidth enhancement factor</b>
<b>B</b>	<b>Bimolecular recombination coefficient</b>
$\beta$	<b>Propagation constant</b>
$\beta_0$	<b>Bragg propagation constant</b>
$\beta_{sp}$	<b>Spontaneous emission parameter</b>
<b>C</b>	<b>Chirp parameter</b>
$dt$	<b>Time step size</b>
$dz$	<b>Distance step size</b>
$\delta$	<b>Deviation from real part of propagation constant (<math>\beta - \beta_0</math>)</b>
$\delta n$	<b>Amplitude of refractive index perturbation</b>
$\Delta n$	<b>Carrier induced refractive index change</b>
$\Delta z$	<b>Length of section</b>
<b>E</b>	<b>Electric field</b>
$\epsilon$	<b>Gain saturation parameter</b>
$f_m$	<b>Mode locking frequency</b>
<b>F</b>	<b>Forward propagating field</b>
$F_N$	<b>Carrier noise</b>
<b>FBG</b>	<b>Fiber Bragg grating</b>
<b>FWHM</b>	<b>Full-width at half maximum of a function or curve</b>
<b>HSPS</b>	<b>Hybrid soliton pulse source</b>
$\Phi$	<b>Chirp function</b>
<b>g</b>	<b>Gain</b>

$\gamma$	(Defined)
$\eta$	Field coupling factor between laser and fiber
$I_{rf}$	Amplitude of RF current
$I_{dc}$	DC bias current
$I_{th}$	Threshold current
$j$	complex number ( $\sqrt{-1}$ )
$k$	Wavevector
$\kappa$	Coupling factor
$\kappa_p$	Peak of Gaussian $\kappa$ variation
$L_1$	Length of laser
$L$	Length of grating*
$L_c$	Length of external cavity
$L_H$	Half-width of the apodization function profile
LED	Light Emitting Diode
$\lambda$	Operating wavelength
$\lambda_o$	Bragg wavelength
$\Lambda$	Pitch of the grating
$m$	Modulation index
$M$	Number of grating sections
$M_B$	Order of Bragg grating
$n$	Refractive index
$n_{eff}$	Effective refractive index (modal index)
$n_{co}$	Refractive index of unmodified fiber core
$n_l$	Refractive index of laser cavity (active region)
$N$	Electron density
$N_o$	Transparency carrier density
$\pi$	pi constant (3.14...)
$\rho$	Reflectivity (field)
$\rho_p$	Desired peak reflectivity (field)
$r_1$	Field reflectivity of left facet (HR coating)
$r_2$	Field reflectivity of right facet (end of grating)
$r_3$	Field reflectivity of AR coating
$R$	Reverse propagating field

$R_{sp}$	Spontaneous emission rate
$s$	Spontaneous emission into the fields
$s_f$	Spontaneous emission noise into the forward wave
$s_r$	Spontaneous emission noise into the reverse wave
$t$	Time
$\sigma$	DC coupling coefficient
$\hat{\sigma}$	DC “self-coupling” coefficient
$\tau_n$	Carrier lifetime
$\Gamma$	Confinement factor
$z$	Space variable in Cartesian coordinates
RIN	Relative intensity noise
TBP	Time-bandwidth product

EC YÜKSEKÖĞRETİM KURULU  
DOKÜMANLARI MERKEZİ

## **CHAPTER 1**

### **INTRODUCTION**

The noise characteristics of semiconductor laser diodes are among the fundamental properties of the lasers and have important implications in the practical applications of laser. There has been a great deal of both theoretical and experimental studies on these characteristics. Operating characteristics of a semiconductor laser are strongly affected by external optical feedback. As it has been observed long ago [1], external optical feedback can significantly affect the performance of a semiconductor laser. In optical communication systems, unintentional reflection can easily occur, e.g. due to the fiber pigtailed in fiber-optic communication systems or from the front end of the optical fiber if this is not properly tapered. Optical feedback provided by a grating reflector or an external mirror can be used in order to select a distinct longitudinal mode, to achieve considerable linewidth narrowing or to tune the emission frequency of a laser.

In the past, relative intensity noise (RIN) was studied in detail with respect to the change of external cavity length and the reflectivity of the external mirror [2]. It was investigated for different feedback levels [3-4] by using rate equations with Langevin noise sources for external cavity lasers. A frequency noise characteristic of a semiconductor laser, taking into account multiple reflections in the external cavity, was also described in weak and strong feedback for these lasers [5] that a grating reflector or an external mirror provides optical feedback. In these studies, it is found that there are five phenomenologically distinct operating regimes, ranging from weak to strong feedback levels. The first four regimes are weak to moderate feedback levels, where feedback was seen as a perturbation on the intrinsic diode lasing field. The RIN is low for weak to moderate levels of feedback but increases tremendously in regime four. In regime three, the frequency noise spectrum is suppressed for low frequencies that indicate strong linewidth narrowing [6]. A wealth of dynamics

ranging from RIN suppression to coherence collapse in a chaotic state has been observed within these feedback levels [7]. Strong optical feedback (regime five) also causes significant reduction of the RIN provided that single-mode operation is maintained [8-9]. In the fifth regime, strong external feedback is used to control the lasing medium. These studies showed that feedback from a highly frequency-selective external cavity leads to stable, single mode operation. Experimentally it was also shown that these lasers are stable over further extraneous secondary feedback [10]. This led to the increase in research on strong feedback external cavity lasers for optical communication systems. Several strong feedback external cavity lasers frequency selective schemes have been reported in literature, including;

1. feedback from a grating [11]
2. feedback from a high-Q narrow-band resonator [12]
3. the feedback from a Fiber Bragg Grating (FBG) reflector [13]

In this thesis, FBG is used as an external cavity in strong external cavity laser. The strong feedback can only be obtained with an anti-reflection (AR) coating of one laser facet as in our model.

Many theoretical models for quantum noise and modulation response of lasers with feedback have been described in the literature. However many of these models concentrate only on weak feedback conditions. Ferreira *et. al.* [14] were the first to conduct a detailed study of both noise and modulation performance under strong feedback conditions. However, their treatment underestimated the importance of including retarded field components to represent the significant external cavity delay. They also excluded chip and package parasitic and nonlinear distortion effects. Recently, several other groups have conducted research on strong feedback induced effects such as bistability, self-pulsations and anomalous spectral behavior including subharmonic generation and the appearance of narrow peaks centered around the harmonics of the cavity resonance in noise and modulation spectra [15-17].

Actively mode-locked semiconductor lasers with strong external cavity FBGs are interesting short optical pulse sources for high-speed optical communication, because generated pulses have low timing jitter and large locking range at a fixed control wavelength. Active mode- locking is accomplished by applying a current waveform



to the gain section, including a DC bias close to the threshold value plus an RF component that can be varied in amplitude and frequency at a frequency equal to the inverse round trip period. The hybrid soliton pulse source (HSPS) is one such device, developed as a pulse source for soliton transmission system [18]. Using linearly chirped FBG in the HSPS results in a tunable system over the range of mode-locked frequencies, as the cavity length is wavelength dependent [18]. Because of this property and its very high power, HSPS becomes a very attractive pulse source for high-speed soliton transmission systems.

The refractive index of the fiber material changes nonlinearly with the optical intensity. This nonlinearity of the refractive index can be used to compensate the pulse broadening effect of dispersion in optical fibers. Intensity dependent refractive index induces chirp in the pulses by means of a phenomenon known as self-phase modulation. This chirp opposes the chirp generated by dispersion. If the magnitudes of these chirps are made equal to each other by correctly selecting the shape and peak power of the pulse, a shape preserving pulse known as the fundamental soliton develops. Depending on the amount of chirp generated by self-phase modulation, the pulses will either be broadened or compressed (higher-order solitons). Actually, a soliton is a special solution of nonlinear Schrodinger equation in the wavelength region of anomalous dispersion. Fortunately, the anomalous dispersion in optical fibers happens at longer wavelengths where the loss is also minimum. The use of solitons can eliminate the dispersion limit on high capacity, and the use of Erbium doped fiber amplifiers (EDFA) can eliminate the attenuation limit on the repeater spacing. In turn, very long distance and very high bit-rate optical fiber transmission would be possible.

Generation of solitons in optical fibers has been experimentally shown in the past, first by using color center lasers. Because of their disadvantages (bulky and expensive), their use is ruled out, leaving the space to the ideal light source for optical communication systems; semiconductor lasers. Compared with the other laser types, laser diodes have the highest efficiency, lower power electrical excitation, smaller size, more suitable for interfacing with other semiconductor devices or optical fibers, and their ability of being directly modulated or mode-locked at very high frequencies.

The requirements for a practical optical pulse source for use in soliton transmission systems can be split into two major categories. The first, and most important, is the performance, which sets very stringent requirements on all major operating parameters of the source. The second, which has a large bearing on the possible commercialization of soliton based communications systems, is the cost and reliability of a source.

The major parameters of a pulse source are its operating wavelength, repetition frequency, pulsewidth, pulse shape and time-bandwidth product (TBP). Control of the operating wavelength is critical to allow soliton propagation, particularly in systems employing wavelength division multiplexing, where multiple channels are placed close together and the required channel spacing must be kept constant. The use of sliding guiding optical filters to control soliton transmission [19] also requires specific operating wavelengths in multiple wavelength systems. The repetition rate of the source must be exactly the same as the clock rate in the transmission system, for example 2.48832 GHz or twice and four times this rate for standard Synchronous Optical Network (SONET) applications. This represents a severe restriction for standard mode-locked lasers, which have a fixed cavity length and typically only operate over a very small frequency range. The fixed cavity length determines the operating frequency, which is close to the cavity resonance frequency (inverse of round trip time). Small deviations from this frequency take the device off resonance and stop the mode-locking action. It is also important when using a mode-locked laser as the source that the device operates at its fundamental cavity frequency, to maintain coherence between all pulses in the output waveform. When operating at a harmonic of the fundamental cavity frequency a more complex laser design may be necessary, as described in [20]. The required pulsewidth depends on the operating bit-rate of the transmission system. Shorter pulsewidths require higher average power levels for soliton propagation, while longer pulses tend to interact with neighboring pulses. Pulsewidths are typically chosen to occupy approximately 1/5 of the operating bit period, giving a range from 20 ps to 80 ps, for systems operating from 10 GBit/s to 2.5 GBit/s. The optimum pulse shape for a standard soliton transmission system would be  $\text{sech}^2$  in shape, to match the soliton shape. However, it has been shown that other symmetrical pulse shapes, such as Gaussian shaped pulses will also work [20]. In systems with sliding guiding filters, the optimum pulse shape is more

complex due to the interaction between the pulses and filters. It is unlikely that a pulse source can produce the optimum shape precisely. One major restriction on the pulse source is that the output waveform must be transform limited, or close to transform limited, to allow optimum system operation. In order to be transform-limited pulse, the TBP of the pulse must lie in the range of 0.3 to 0.5 [21], which is TBP of  $\text{sech}^2$  and Gaussian pulses, respectively. This restriction is reduced somewhat in systems employing sliding-frequency guiding filters, which are more tolerant to lower fidelity pulse waveforms.

The realization of long distance soliton based transmission systems requires a reliable stable source of transform limited pulses of the correct pulsewidth and at the wavelength peak of erbium-doped fiber amplifier chain (1.55  $\mu\text{m}$ ). A practical system may operate at 2.488 GHz with pulsewidth of around 50 ps. The HSPS has been experimentally demonstrated in the mode-locking regime at 2.5 GHz [18]. A model for the mode-locked HSPS has already been reported by Ozyazici *et. al.* [22] and a more completed scheme including the grating parameters and the laser diode drive conditions on the response of the HSPS has been investigated in [23].

Although many theoretical models for modulation response and mode locking performance of strong feedback external cavity lasers have been described in the literature [24-25], no studies have been made showing noise characteristics of these lasers at the mode-locked condition. The main purpose of this thesis is to determine the effect of noise on mode-locked HSPS.

In this thesis, it is described that how the spontaneous and carrier noise affects the output pulse of mode-locked HSPS utilizing different FBGs such as uniform, Gaussian apodized, linearly chirped uniform and linearly chirped Gaussian apodized and RIN spectrum of HSPS. The most effective noise parameters are also investigated in this work.

FBGs are reviewed in Chapter 2, including FBG fabrication techniques, fundamental properties of FBGs and their usage in optical communication systems. This chapter is devoted to modeling of FBGs where coupled-mode equations are derived for uniform, chirped and apodized gratings. These equations are then written in a compact form to be used in modeling of any type of (uniform, chirped, apodized,

both chirped and apodized) grating. In order to investigate the nonuniform grating types, the coupled-mode equations are converted to a transfer matrix model using the piecewise-uniform approach. In this approach it is assumed that a nonlinear grating is assumed to be consist of many small uniform gratings having a finite length. The length of each uniform section is assumed to be much larger than the biggest period of the corrugation. The solution of the coupled-mode equations for any type of grating is also given in Chapter 2.

The results obtained using the FBG model are given in Chapter 3. The results of uniform, linearly chirped uniform, Gaussian apodized, and linearly chirped Gaussian apodized gratings with 0.5 and 0.99 peak reflectivity are given and explained.

Mode locking in semiconductor lasers and active mode-locking technique is reviewed in Chapter 4. A complete mathematical model of the mode-locked HSPS is given in this chapter. The laser diode model, fiber and grating models are explained. An in depth explanation of the fiber to laser coupling and antireflection coating, and their effects on the counter-propagating fields are followed by the boundary conditions at the ends of the external cavity.

Results of mode-locked HSPS with noise are given in Chapter 5. In this chapter, spontaneous noise, carrier noise and RIN are explained. Then mode-locked pulses are analyzed for different types of gratings with spontaneous noise and carrier noise.

RIN spectrums of mode-locked HSPS with FBGs are presented in Chapter 6. Firstly, RIN spectrums of all of FBGs are given using standard laser diode parameters. Then the effect of bias currents and drive parameters of the laser diode on RIN is determined.

In Chapter 7, results obtained from the mode-locked HSPS with noise using different FBGs are concluded. The main conclusion is that RIN reduction is possible for the mode-locked HSPS by selecting a suitable apodization function such as Gaussian and linear chirp rate.

## **CHAPTER 2**

### **MODEL OF FIBER BRAG GRATING (FBG)**

#### **2.1 Introduction**

Optical fibers have been developed to the point where they are now synonymous with modern telecommunication and optical sensor networks. A major drawback to the evolution of optical fiber-based networks has been the reliance on bulk optics for conditioning and controlling the guided light beam. The necessity of coupling light out the waveguides to perform, for example, reflection, diffraction, and filtering (spatial, polarization, etc.) is an inherently lossy process. Moreover, coupling light in and out of fiber significantly increases the number of high-quality, bulk optic components, often requiring stringent tolerance on optical alignment, thus making conceptually simple systems complicated and expensive in practice. Replacing a bulk optic mirror or beam splitter with a fiber equivalent can dramatically increase system stability and portability, while reducing overall size, thus pushing laboratory-based experiments into real world environments. The most successful fiberized technology to date is the optical fiber laser and amplifier and fused tapered coupler. The intrinsic low loss nature of these components and their compatibility with integrated optic waveguide structures have made them indispensable to the continued development of optical systems as a whole.

With the significant discovery of photosensitivity in optical fibers, a new class of in fiber component has been developed, called the FBG. This device can perform many of the aforementioned primary functions, such as reflection and filtering, in a highly efficient, low loss manner. FBGs are set to revolutionize telecommunications, and will also, have a critical impact on the optical fiber sensor field. This is a comparatively simple device and in its most basic form consists of a periodic modulation of the index of refraction along the fiber core.

The Bragg grating is also capable of coupling light from a propagation mode to another mode that has a propagation constant that matches the spatial periodicity of the grating. This may result in coupling between the forward and backward propagation core modes, or between the fundamental core mode and cladding or radiation modes. This property may be employed in fiber amplifiers to selectively out couple unwanted wavelengths, giving uniform spectral gain.

A FBG is an optical fiber for which the refractive index in the core is perturbed forming a periodic or quasi-periodic index modulation profile. A narrow band of the incident optical field within the fiber is reflected by successive, coherent scattering from the index variations. When the reflection from a crest in the index modulation is in phase with the next one, maximum mode-coupling or reflection occurs. Then the Bragg condition is fulfilled, i.e.

$$\lambda_B = 2n_{eff} \Lambda \quad (2.1)$$

where  $\lambda_B$  is the Bragg wavelength,  $n_{eff}$  is the effective modal index and  $\Lambda$  is the perturbation period. By modulating the quasi-periodic index perturbation in amplitude and (or) phase, we may obtain different optical filter characteristics.

In the most general case, the index perturbation  $\delta n(z)$  takes the following form for the phase and amplitude-modulated periodic waveform

$$\delta n(z) = \delta n_0(z) \left[ 1 + m \cos \left( \frac{2\pi z}{\Lambda} + \Phi \right) \right] \quad (2.2)$$

Both the average refractive index and the envelope of the grating modulation, and therefore the modal index  $n_{eff}$ , usually vary along the grating length. The contrast, which is determined by the visibility of the UV fringe pattern, is given by the parameter  $m$ . The local reflectivity  $\rho(z)$  is the complex ratio of the forward and backward going wave amplitudes. The coupling coefficient  $\kappa$  is given by

$$\kappa = \frac{\pi}{\lambda} \delta n g(z) \quad (2.3)$$

where  $g(z)$  is an apodization function, typically a Gaussian or raised-cosine weighting.

The formation of permanent gratings by photosensitivity in optical fiber was first demonstrated by Hill *et. al.* in 1978 [26]. Photosensitivity means that exposure of UV light leads to a rise in the refractive index of certain doped glasses. Typical values for the index change are ranging between  $10^{-6}$  to  $10^{-3}$ , dependent on the UV-exposure and the dopants in the fiber. By using techniques as hydrogen loading [27], an index change as high as  $10^{-2}$  can be obtained. The physical mechanism behind photosensitivity is not yet fully understood.

Fiber gratings are nowadays usually fabricated by a variant of the transverse holographic method first proposed by Meltz *et. al.* [28]. By exposing the fiber to a UV interference pattern from the side, the pattern is "printed" into the fiber [29], see Figure 2.1. Only the core is usually doped (for example with germanium), and consequently the grating is only formed in the core and not in the cladding. In order to write nonuniform gratings with advanced characteristics, one can use the scheme suggested by Stubbe *et. al.* [30].

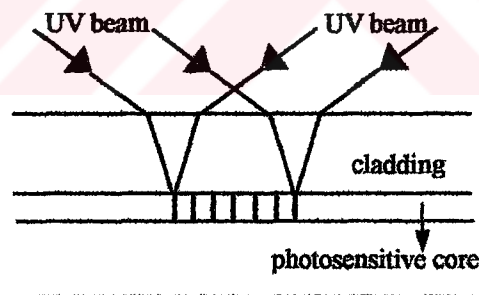


**Figure 2.1** The transverse holographic method for writing fiber gratings. Two coherent UV beams produce an interference pattern in the fiber. The periodicity of the resulting grating is dependent on the angles of the incident beams

The other method is known as the phase-mask method, in which fine slits are made in a phase mask mounted on a silica substrate by exposing it to an electron beam or the like. For light passing through the mask, the 0-order light traveling straight ahead is almost entirely suppressed, so that the interference produced by the  $\pm 1$ -order light can be formed on the fiber. The relationship between the period of the phase mask  $\Lambda_{\text{mask}}$  and the period of the fiber grating  $\Lambda_{\text{FBG}}$  may be shown as

$$\Lambda_{mask} = 2\Lambda_{FBG} \quad (2.4)$$

Thus when it comes to producing fiber gratings of different wavelengths, this method has disadvantage of requiring several masks according to the period of the grating, making for higher cost than with the holographic method. However it achieves more stable characteristics and is better suited to mass production, and is therefore the method generally adopted for the manufacture of optical fiber gratings.

The optical characteristics of fiber gratings are determined by three parameters: the magnitude of perturbation in the refractive index, the period of the grating, and its length. The magnitude of refractive index perturbation and grating length in the main greatly influence reflectance and bandwidth. The period of the grating, on the other hand, determines the center wavelength, and it is also possible, by varying its magnitude in the longitudinal direction, to realize various types of gratings.

Because a FBG can be designed to have an almost arbitrary, complex reflection response, it has a variety of applications, well described by Hill and Meltz among others [29]. For telecommunications, the probably most promising applications have been dispersion compensation [30] and wavelength selective devices [31]. Examples of the latter are filters for Wavelength Division Multiplexing (WDM) [32]. FBGs have also become popular as sensing devices, ranging from structural monitoring to chemical sensing [33]. Any changes in the fiber properties, such as strain, temperature, or polarization, which varies the modal index or grating pitch, will change the Bragg wavelength. Another noteworthy application of fiber gratings is to use them as reflectors for fiber lasers [34].

Conventional Bragg gratings (not fiber) have been used with laser diodes for many years. With formation of FBGs, initially the grating was etched into the surface of a side polished fiber, and now UV-induced Bragg gratings are used. A simple but effective means of controlling the laser wavelength is by incorporating a Bragg grating in the pigtail of the diode laser. This technique is favorable when compared to other types of feedback techniques such as distributed feedback (DFB) or distributed Bragg reflector (DBR) due to low cost and the simple manufacturing procedure. One problem with the DBR laser is the precise control of the laser



wavelength. For instance, production of a DBR laser with a specified precision of wavelength less than 1 nm is very difficult. However, FBG s can be manufactured precisely to any required wavelength. With the antireflection coating on the laser diode chip, the lasing wavelength can be selected anywhere in the gain bandwidth by choosing an appropriate Bragg resonant wavelength of the grating.

There are two important advantages of single mode FBG lasers over the conventional FBG lasers and over the conventional DFB and DBR lasers. One of them is their relative insensitivity to the changes in temperature and drive current. The other advantage is the ability to perform direct high-speed modulation with a very low level of chirp

FBGs have also been used to provide feedback for active mode-locked semiconductor lasers. Mode-locking in these systems is accomplished by modulating the injection current of the laser at the characteristics frequency of the optical cavity, which is determined by the position of the FBG. The reflection profile of the grating limits the number of modes that can oscillate and thus determines the duration of the mode-locked pulses. This type of laser diodes with uniform FBG has been shown to produce transform-limited pulses (~19 ps) at very high output levels. This device has the disadvantage of operating at very specific conditions and showed spectral instabilities when operating conditions were changed. The use of a linearly chirped FBG has not only overcome this spectral instability problem [18], but also resulted in a tunable system over the range of mode-locked frequencies, as the cavity length was wavelength dependent. With this device, transform-limited pulses (~50 ps) with repetition rates up to 2.5 GHz have been demonstrated.

There are several methods employed to model a grating. The starting point of these models is the Maxwell's equations. Starting from these equations, phase and amplitude for the waves inside a grating can be calculated assuming weak guidance. The most well known technique that relies on this assumption is the couple- mode theory [35]. In this approach, a set of first order differential equations is considered for the amplitude of the fields along the fiber. This set of equations has analytical solutions for the uniform grating with periodical sinusoidal index variation.

A complex grating structure can have a nonuniform period and/or amplitude of the refractive index along the grating. The coupled-mode approach in the most general case, and for complicated grating structures, involves the numerical solution of two coupled differential equations, since analytic solutions are only possible for the uniform gratings [36].

The transfer matrix method (TMM) [37] has also been developed for the purpose of grating analysis. In this method the grating is divided into sections, with the length of each one being much bigger than the biggest period of the corrugation. In each small section, the period and the peak of the refractive index can be assumed to be constant. A transfer matrix corresponding to a uniform grating describes each of these sections and an overall structure is characterized by global matrix obtained as the product of the individual matrices. This approach is suitable for periodic and aperiodic structures, as well as for long gratings.

## 2.2 Derivation of Coupled- Mode Equations

Coupled- mode equations can be used to model the electric field traveling in both directions inside a grating [38-39], and a coupled cavity laser such as DFB or DBR [40-48]. Although the solution of these equations are obtained by following the procedure for a planar waveguide [39], it has been shown that they are also valid for the fiber Bragg gratings having cylindrical core [48-49].

### 2.2.1 Model of Uniform FBG

Assume that the refractive index of the fiber core varies along the propagation direction shown in Figure 2.2 as

$$n(z) = n_{co} + \delta n \cos(2\beta_o z) \quad (2.5)$$

where  $n_{co}$  is the refractive index of the unmodified fiber core (usually taken as 1.46),  $\delta n$  is the peak of the index variation ( $\delta n \ll n_{co}$ ).  $\beta_o$  is the Bragg propagation constant given by

$$\beta_o = \frac{M_B \pi}{\Lambda} = \frac{2\pi}{\lambda_o} n_{co} \quad (2.6)$$

where  $\Lambda$  is the period (or pitch) of the periodic structure,  $\lambda_o$  is the Bragg wavelength and  $M_B$  stands for the order of the grating. In practice  $M_B = 1$  and  $M_B = 2$  are commonly used, and  $M_B = 1$  is considered in this work.

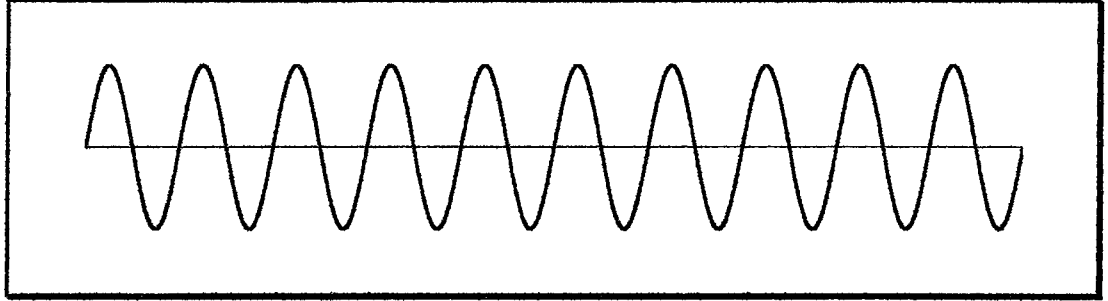


**Figure 2.2** Refractive index variation of uniform FBG (average is  $n_{co} = 1.46$ )

Neglecting the lateral and transverse variations of the lasing field as well as the phase factor  $\exp[j(\omega t - \beta z)]$  (the slowly varying envelope approximation), the wave Equation reduces to

$$\frac{\partial^2 E}{\partial z^2} + [n(z)k]^2 E = 0 \quad (2.7)$$

where  $k$  is the wave vector given as  $2\pi/\lambda$ . The square term can be written as

$$[n(z)k]^2 = \beta^2 + 4\beta\kappa \cos(2\beta_o z) \quad (2.8)$$

where  $\Delta n^2$  is neglected since it is very small and

$$\beta = \frac{2\pi}{\lambda} n_{co}, \quad \kappa = \frac{\pi \delta n}{\lambda} \quad (2.9)$$

It is now assumed that the propagation constant  $\beta$  is close to the Bragg propagation constant  $\beta_o$

$$\beta = \beta_o + \delta \quad (2.10)$$

where  $\delta \ll \beta_0$ . The term  $\delta$  denotes the deviation of the real part of the propagation constant from the Bragg condition.

Assuming that the field inside the grating consists of a forward-propagating field  $F(t,z)$  and a reverse propagating field  $R(t,z)$  [38–42]. The field inside the HSPS can be given as:

$$E(z) = F e^{-j\beta_0 z} + R e^{j\beta_0 z} \quad (2.11)$$

Due to the presence of the Bragg propagation constant in the phase factors, the functions  $F$  and  $R$  will have comparatively weak  $z$  dependence. Inserting equations (2.8) and (2.11) into (2.7), neglecting the second derivatives of  $F$  and  $R$  due to the weak  $z$  dependence, as well as the higher order phase terms (i.e.  $\exp(-3\beta_0 z)$  and  $\exp(+3\beta_0 z)$ ) and collecting the terms with identical phase factors leads to

$$-2j\beta_0 F' + (\beta^2 - \beta_0^2)F + 2\beta\kappa R = 0 \quad (2.12)$$

$$2j\beta_0 R' + (\beta^2 - \beta_0^2)R + 2\beta\kappa F = 0$$

Since  $\delta \ll \beta_0$ ,

$$\beta^2 - \beta_0^2 \cong 2\beta_0 \delta \quad (2.13)$$

Putting this equation into equations (2.12) and assuming  $\beta/\beta_0 \cong 1$ , coupled-mode equations in (2.12) can be separately rewritten as [38],

$$-F' - j\delta F = j\kappa R \quad (2.14)$$

$$R' - j\delta R = j\kappa F \quad (2.15)$$

### 2.2.2 Model of Chirped FBG

If the pitch of the grating varies along the propagation direction  $z$  as shown in Figure 2.3, the grating is called chirped grating. In this case, the refractive index given in equation (2.5) is no longer valid and an extra phase term must be introduced in the refractive index equation

$$n(z) = n_{\infty} + \delta n \left[ 1 + m \cos \left( \frac{2\pi}{\Lambda(z)} z \right) \right] \quad (2.16)$$

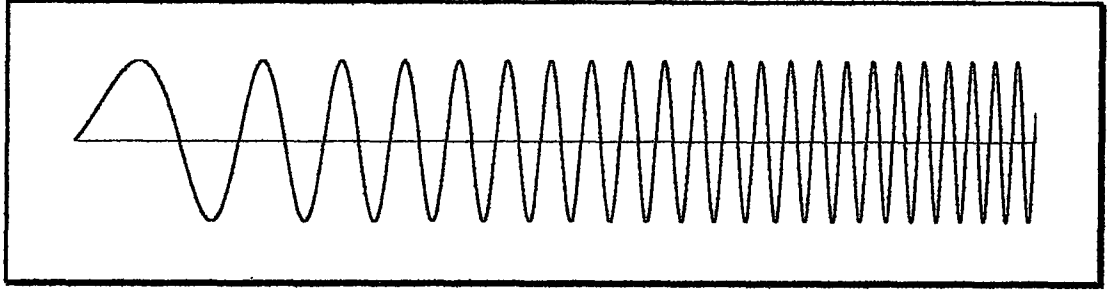


**Figure 2.3** Refractive index variation of chirped FBG (average is  $n_{\infty} = 1.46$ )

Here  $\delta n$  represents the “dc” index change spatially averaged over a grating period (slowly varying envelope function of the induced change in index) and  $m$  is the visibility of the index change, which is also called the modulation index of the grating. In this work,  $m$  is considered to lie between 0 (no grating) and 1 (perfectly balanced interferometer). The grating pitch is accepted to be linearly chirped such that the operating wavelength  $\lambda_o$  corresponds to the center of the grating and the wavelength is chirped by  $C = d\lambda_o/dz$  (nm/cm) around the center. This variation can be denoted as

$$\lambda(z) = \lambda_o + \frac{d\lambda_o}{dz} z = \lambda_o + C z \quad (2.17)$$

and since

$$\Lambda(z) = \frac{\lambda(z)}{2n_{\infty}} = \frac{\lambda_o + C z}{2n_{\infty}} \quad (2.18)$$

the phase term in equation (2.16) can be rewritten as

$$\frac{2\pi}{\Lambda(z)} z = \frac{4\pi n_{\infty}}{\lambda_o + C z} z \quad (2.19)$$

Rewriting the denominator in terms of  $\lambda_o$  and expanding as Taylor series gives

$$\frac{2\pi}{\Lambda(z)} z = \frac{4\pi n_{co}}{\lambda_o \left(1 + \frac{Cz}{\lambda_o}\right)} z \cong 2\beta_o \left(1 - \frac{Cz}{\lambda_o}\right) z \quad (2.20)$$

In this expansion, it is assumed that  $Cz \ll \lambda_o$ , since  $C$  is a few nm/cm,  $z$  is a few cm for full length of grating and Bragg wavelength  $\lambda_o$  is considered to be 1550 nm. Replacing the phase term in equation (2.16) with the one given above, equation (2.16) can be rewritten as

$$n(z) = n_{co} + \delta n \left[ 1 + m \cos \left( 2\beta_o z - \frac{4\pi n_{co}}{\lambda_o^2} C z^2 \right) \right] \quad (2.21)$$

If the chirp in the phase term is included, equation (2.21) can be rewritten as

$$n(z) = n_{co} + \delta n \left[ 1 + m \cos(2\beta_o z + \Phi) \right] \quad (2.22)$$

where  $\Phi$  is the grating chirp defined by

$$\Phi = -\frac{4\pi n_{co}}{\lambda_o^2} C z^2 \quad (2.23)$$

Assuming the field in the grating as

$$E(z) = F e^{-j\left(\frac{\pi}{\Lambda(z)}\right)z} + R e^{j\left(\frac{\pi}{\Lambda(z)}\right)z} \quad (2.24)$$

$$E(z) = F e^{-j(\beta_o z + \Phi/2)} + R e^{j(\beta_o z + \Phi/2)}$$

and following the same procedure as the one followed in Section 2.2.1 with

$$\left[ n(z) k \right]^2 = \beta^2 + 4\beta\kappa \left[ \frac{1}{m} + \cos(2\beta_o z + \Phi) \right] \quad (2.25)$$

and the new ac coupling coefficient

$$\kappa = \frac{\pi \delta n}{\lambda} m \quad (2.26)$$

coupled-mode equations for the linearly chirped FBG can be obtained as

$$\begin{aligned} -F' - j \left( \delta + \frac{2\kappa}{m} - \frac{1}{2} \frac{d\Phi}{dz} \right) F &= j\kappa R \\ R' - j \left( \delta + \frac{2\kappa}{m} - \frac{1}{2} \frac{d\Phi}{dz} \right) R &= j\kappa F \end{aligned} \quad (2.27)$$

In this derivation the following assumptions are made due to  $\delta \ll \beta_0$  and  $Cz \ll \lambda_0$ :

$$\frac{\beta}{\left( \beta_0 + \frac{1}{2} \Phi' \right)} \cong 1, \quad \frac{\left( \beta_0 + \frac{1}{4} \Phi' \right)}{\left( \beta_0 + \frac{1}{2} \Phi' \right)} \cong 1 \quad \text{and} \quad \frac{\beta_0}{\left( \beta_0 + \frac{1}{2} \Phi' \right)} \cong 1 \quad (2.28)$$

After defining the “period-averaged” dc coupling coefficient as

$$\sigma = \frac{2\kappa}{m} \quad (2.29)$$

the term inside the parenthesis in equation (2.27), defined as the dc *self-coupling* coefficient [49], can be written as

$$\hat{\sigma} = \delta + \sigma + \frac{4\pi m_{\infty}}{\lambda_0^2} Cz \quad (2.30)$$

where the derivative of the chirp is calculated from equation (2.23). Putting equation (2.30) into (2.27), a set of equations similar to (2.14) and (2.15) can be obtained

$$-F' - j\hat{\sigma}F = j\kappa R \quad (2.31)$$

$$R' - j\hat{\sigma}R = j\kappa F \quad (2.32)$$

### 2.2.3 Model of Apodized FBG

In order to avoid the significant side-lobes in the grating reflectivity (to have a better reflection spectrum) and thus to reduce the oscillations in the group delay, the refractive index profile along the grating can be apodized during the writing process. There are several apodization functions as Gaussian, Hamming, Blackman, Hanning,

Keiser etc. Some other functions resulting in good grating characteristics (a flat region at the grating center and a constant slope decaying characteristic toward the grating's edges) are tanh, sinc and Cauchy,

$$\kappa(z)=\kappa_p \{1+\tanh[X(1-2K^Y)]\} \quad (2.33)$$

$$\kappa(z)=\kappa_p \operatorname{sinc}^X\left(\frac{1}{2}K^Y\right) \quad (2.34)$$

$$\kappa(z)=\kappa_p \frac{1-K^2}{1-(KX)^2} \quad (2.35)$$

respectively. In these functions  $K = 2z/L$  and,  $X$  and  $Y$  are constants.

Since the fiber gratings are frequently written by a Gaussian laser beam [49], and thus have an approximately Gaussian profile, we assume that the grating is Gaussian apodized, unless otherwise stated, which is formulated as

$$\kappa(z)=\kappa_p \exp\left[-\frac{1}{2}\left(\frac{z}{L_H}\right)^2\right] \quad (2.36)$$

Here  $L_H$  is the half width of the profile (at  $1/e$  intensity point) and  $\kappa_p$  is the peak value of  $\kappa$  given in equation (2.26) as

$$\kappa_p = \frac{\pi \delta n}{\lambda} m \quad (2.37)$$

and  $L$  is the grating length. The full width at half maximum (FWHM) of  $\kappa$  can be found from equation (2.36) as

$$FWHM_\kappa = 2L_H \sqrt{2 \ln 2} \quad (2.38)$$

Inserting this term in (2.36) gives a more understandable Gaussian variation of  $\kappa$

$$\kappa(z)=\kappa_p \exp\left(\frac{-4 \ln 2}{FWHM_\kappa^2} z^2\right) \quad (2.39)$$



In most cases, the  $FWHM_{\kappa}$  is related to the grating length by

$$L \cong 3 FWHM_{\kappa} \quad (2.40)$$

Two types Gaussian apodized grating are shown in Figure 2.4.

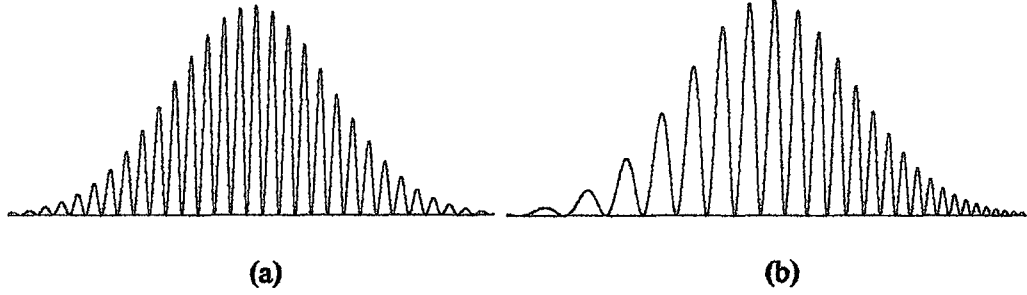


**Figure 2.4** Refractive index variation of Gaussian apodized FBG. a) Uniform pitch, b) linearly chirped (minimum level is  $n_{co} = 1.46$ ,  $m = 1$  for both)

### 2.3 Solution of Coupled-Mode Equations

The coupled-mode pairs given in equations (2.14), (2.15) and (2.31), (2.32) are quite similar and can be solved following the procedure given below:

After some algebraic operations on equations (2.14) and (2.15), the coupled-mode pair can be reduced to a set of second order differential equations with constant coefficients such that

$$F'' - \gamma^2 F = 0 \quad (2.41)$$

$$R'' - \gamma^2 R = 0 \quad (2.42)$$

where  $\gamma$  is defined by

$$\gamma^2 = \kappa^2 - \delta^2 \quad (2.43)$$

A nontrivial general solution for these equations can be written as

$$F = f_1 e^{\gamma z} + f_2 e^{-\gamma z} \quad (2.44)$$

$$R = r_1 e^{\gamma z} + r_2 e^{-\gamma z} \quad (2.45)$$

Substituting (2.44) and (2.45) and their derivatives into (2.14) and (2.15), we can obtain

$$F = f_1 e^{\gamma z} - r_2 \left( \frac{\gamma + j\delta}{j\kappa} \right) e^{-\gamma z} \quad (2.46)$$

$$R = -f_1 \left( \frac{\gamma + j\delta}{j\kappa} \right) e^{\gamma z} + r_2 e^{-\gamma z} \quad (2.47)$$

Assuming that the fields at  $z = 0$  are known and their values at any point  $z$  are required, applying boundary conditions at  $z = 0$ , these equations reduce to

$$F_0 = f_1 - r_2 \left( \frac{\gamma + j\delta}{j\kappa} \right) \quad (2.48)$$

$$R_0 = -f_1 \left( \frac{\gamma + j\delta}{j\kappa} \right) + r_2 \quad (2.49)$$

where  $F_0$  and  $R_0$  are the values of the fields  $F$  and  $R$  at  $z = 0$ , respectively. After some algebraic operations on these equations,  $f_1$  and  $r_2$  can be found as

$$f_1 = \frac{(\gamma - j\delta)F_0 - j\kappa R_0}{2\gamma} \quad (2.50)$$

$$r_2 = \frac{-j\kappa F_0 + (\gamma - j\delta)R_0}{2\gamma} \quad (2.51)$$

Putting  $f_1$  and  $r_2$  into equations (2.46) and (2.47) and using trigonometric identities

$$\sinh(\gamma z) = \frac{e^{\gamma z} - e^{-\gamma z}}{2} \quad \text{and} \quad \cosh(\gamma z) = \frac{e^{\gamma z} + e^{-\gamma z}}{2} \quad (2.52)$$

we can obtain

$$F = \left[ \cosh(\gamma z) - j \frac{\delta}{\gamma} \sinh(\gamma z) \right] F_0 - \left[ j \frac{\kappa}{\gamma} \sinh(\gamma z) \right] R_0 \quad (2.53)$$

$$R = \left[ j \frac{\kappa}{\gamma} \sinh(\gamma z) \right] F_0 + \left[ \cosh(\gamma z) + j \frac{\delta}{\gamma} \sinh(\gamma z) \right] R_0 \quad (2.54)$$

These two equations can also be written in the matrix form as

$$\begin{bmatrix} F \\ R \end{bmatrix} = \begin{bmatrix} \cosh(\gamma z) - j \frac{\delta}{\gamma} \sinh(\gamma z) & -j \frac{\kappa}{\gamma} \sinh(\gamma z) \\ j \frac{\kappa}{\gamma} \sinh(\gamma z) & \cosh(\gamma z) + j \frac{\delta}{\gamma} \sinh(\gamma z) \end{bmatrix} \begin{bmatrix} F_0 \\ R_0 \end{bmatrix} \quad (2.55)$$

or in a more compact form

$$\begin{bmatrix} F \\ R \end{bmatrix} = \mathbf{T} \begin{bmatrix} F_0 \\ R_0 \end{bmatrix} \quad (2.56)$$

where  $\mathbf{T}$  is called the transmission matrix. If the field is to be calculated at  $z = L$ , then all  $z$  in the  $\mathbf{T}$  matrix must be replaced by  $L$ .

If the grating is assumed to be made up of  $M$  sections each having a length of  $\Delta z$  (piecewise-uniform approach), the fields at  $i^{\text{th}}$  section can be calculated from the known fields of the  $(i-1)^{\text{th}}$  section such that

$$\begin{bmatrix} F_i \\ R_i \end{bmatrix} = \mathbf{T}_i \begin{bmatrix} F_{i-1} \\ R_{i-1} \end{bmatrix} \quad (2.57)$$

For the most general case, a fiber Bragg grating can be both linearly chirped and apodized. In this case, the modified transmission matrix for the  $i^{\text{th}}$  section can be written, replacing  $\delta$  with  $\hat{\sigma}$  in equation (2.30) for the modeling of chirped Bragg gratings and taking  $\kappa$  as in equation (2.39), as

$$\mathbf{T}_i = \begin{bmatrix} \cosh(\gamma \Delta z) - j \frac{\hat{\sigma}}{\gamma} \sinh(\gamma \Delta z) & -j \frac{\kappa}{\gamma} \sinh(\gamma \Delta z) \\ j \frac{\kappa}{\gamma} \sinh(\gamma \Delta z) & \cosh(\gamma \Delta z) + j \frac{\hat{\sigma}}{\gamma} \sinh(\gamma \Delta z) \end{bmatrix} \quad (2.58)$$

Although the subscripts are not shown, for the sake of simplicity, in this equation,  $\gamma$ ,  $\kappa$  and  $\hat{\sigma}$  are different for each section and must be calculated individually before putting into the transfer matrix.

Assuming a grating with a length  $L$  extends from  $z = -L/2$  to  $z = L/2$ , the calculations start with  $F_0 = F(L/2) = 1$  (normalized amplitude) and  $R_0 = R(L/2) = 0$ , develop through  $z = -L/2$  and end with the calculation of the fields  $F(-L/2) = F_M$  and  $R(-L/2) = R_M$ . Once all of the matrices for the individual sections are known, the amplitudes can be found from the multiplication of the transfer matrices such that

$$\begin{bmatrix} F_M \\ R_M \end{bmatrix} = \mathbf{T} \begin{bmatrix} F_0 \\ R_0 \end{bmatrix} \quad \text{where} \quad \mathbf{T} = \mathbf{T}_M \cdot \mathbf{T}_{M-1} \cdot \dots \cdot \mathbf{T}_1 \cdot \dots \cdot \mathbf{T}_1 \quad (2.59)$$

The number of sections needed for the calculations is determined by the required accuracy. For most cases,  $M \approx 100$  is sufficient [49].  $M$  may not be arbitrarily large, since the approximations that lead to the coupled-mode equations (2.31) and (2.32) are not valid when a grating section is only a few grating periods long. Thus, we require  $\Delta z \gg \Lambda$  which means that (since  $\Delta z = L/M$ ,  $\Lambda = \lambda_0/2n_{co}$ )

$$M \ll \frac{2n_{co}L}{\lambda_0} \quad (2.60)$$

The amplitude reflection coefficient of the Bragg grating can be calculated from the proportion of the reverse and forward propagating fields at  $z = -L/2$

$$\rho = \frac{R_M}{F_M} \quad (2.61)$$

and the power reflection coefficient is simply  $|\rho|^2$ .

## CHAPTER 3

### RESULTS OF THE FIBER BRAGG GRATING MODEL

#### 3.1 Introduction

In this chapter, the results of the grating model are presented. A computer model was developed according to the equations given in Chapter 2. This model is based on the piecewise uniform approach with the grating is divided into  $M$  equal-length sections. Both the chirping and the apodization effects are included in the model. By changing some parameters in the program, it is possible to obtain the response of different types of gratings such as uniform (no chirp, no apodization), linearly chirped (no apodization), Gaussian apodized (no chirp) and -the most general case- linearly chirped apodized (both chirped and apodized).

Table 3.1 shows the standard values of grating parameters.

Table 3.1 Standard parameters for the FBG model

Parameter	Symbol	Standard value	Unit
Grating length	L	4	cm
# Grating sections	M	142	
Desired peak reflectivity (field)	$\rho_p$	0.5	
Peak of Gaussian $\kappa$ variation	$\kappa_p$	1.0	$\text{cm}^{-1}$
Modulation index	m	0.8	
Wavelength chirp	C	-1.9	nm/cm
Refractive index of unmodified fiber core	$n_{co}$	1.46	

In the grating model, the design wavelength was taken as  $1.55 \mu\text{m}$  where the fiber loss is minimum. The parameters in showed Table 3.1 (desired peak reflectivity and the peak of Gaussian  $\kappa$  variation) are used interchangeably, i.e. when the desired

peak reflectivity is entered,  $\kappa_p$  is calculated by iteration to give that reflectivity. Similarly, when the  $\kappa_p$  is entered, the peak reflectivity is calculated according to that  $\kappa_p$ . There is also a control parameter for the apodization which shows that either Gaussian apodization is taken into account or not. If Gaussian apodization is not present, then the value of  $\kappa_p$  is considered to be constant through the entire grating length.

All the other parameters except the wavelength can be changed in the program according to the required specifications. One can design a grating with a certain reflectivity, the program gives the  $\kappa_p$  and hence the index variation  $\delta n$  that must be created during the writing process.

### **3.2 Design of FBG with Desired Peak Reflectivity**

In this section, the design of Bragg gratings with the known chirp and apodization, and desired peak reflectivity is presented. The program iterates the value of  $\kappa_p$  and hence the amount of refractive index deformation that will result in the desired reflectivity will be known. This allows one to design a grating and then write it.

#### **3.2.1 Uniform FBGs**

The reflection spectrum of a uniform grating with 0.5 peak reflectivity is shown in Figure 3.1. The spectrum is narrow, 0.2 Å (FWHM) and  $\kappa_p$  is 0.499 cm<sup>-1</sup>. There are many side-lobes at the long- and short-wavelength sides of the main lobe. These lobes are the result of the Fabry-Perot effect employed by the grating edges that behave as partially reflecting mirrors [49-50]. Inspecting the Figure 3.1, one may think that the reflectivity curve looks like a sinc function that is the Fourier transform of a unit step (rectangular) pulse.

This is because a rectangular pulse can approximate a uniform grating with a small but constant amplitude index variation over a dc offset ( $n_{GS}$ ) when observed from afar. This behavior is explained in detail in [36]. The group delay characteristics are also shown in this figure. The jump discontinuities in the group delay response are the result of the side-lobes at the reflection spectrum [51-52]. Since the phase of the

reflectivity vanishes ( $\pi$  phase change in the phase of reflection) at the minimums of the spectrum, their derivatives are discontinuous at these points as shown in Figure 3.2. Since the group delay is proportional to the phase of the reflectivity, there will also be discontinuities at these jumps as shown in Figure 3.1.

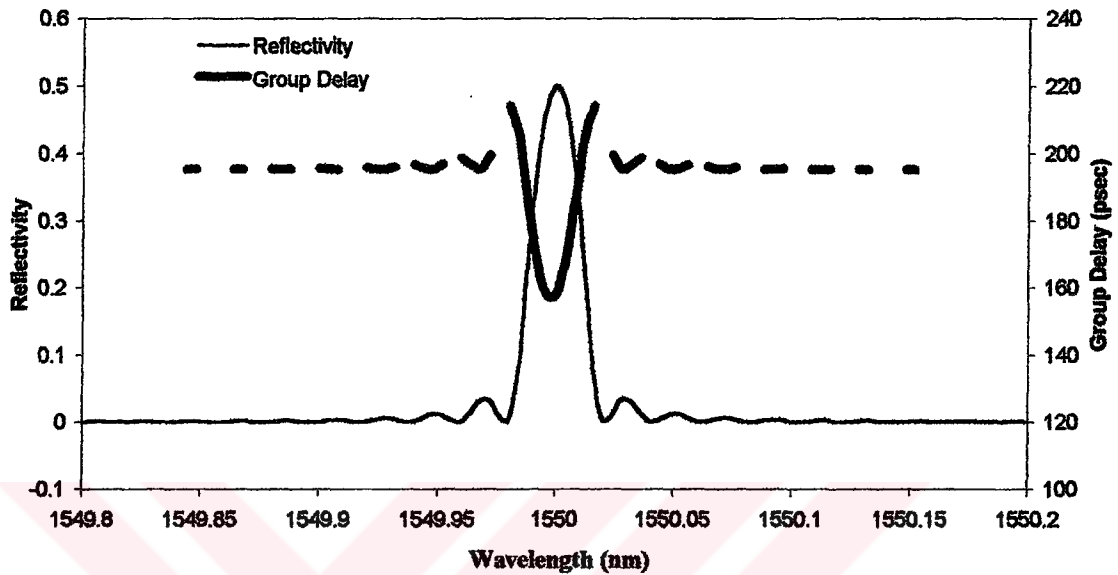


Figure 3.1 Reflectivity and group delay characteristics for uniform FBG with 0.5 peak reflectivity

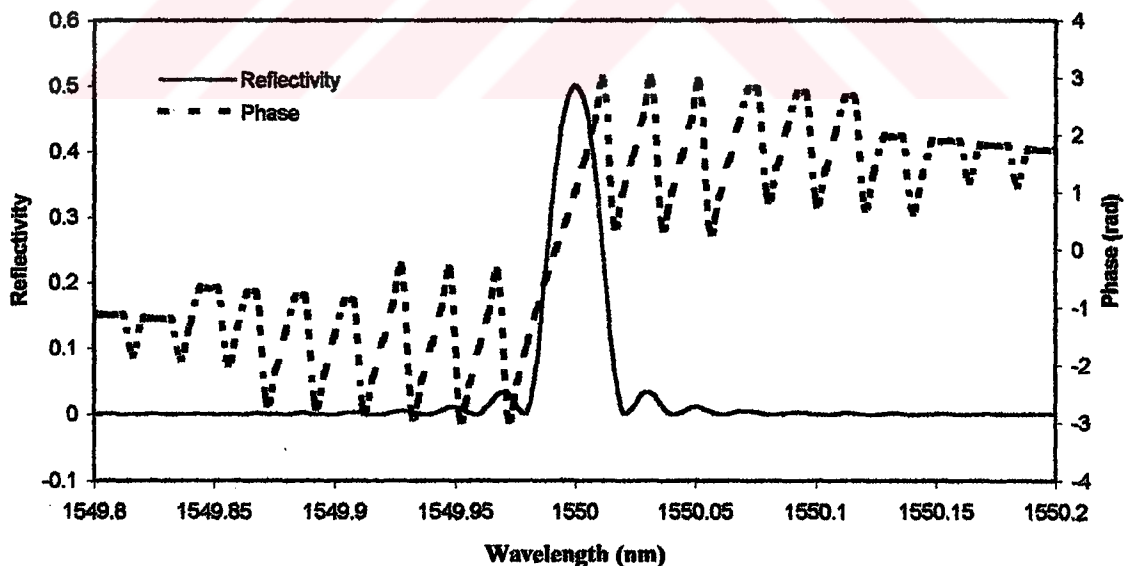
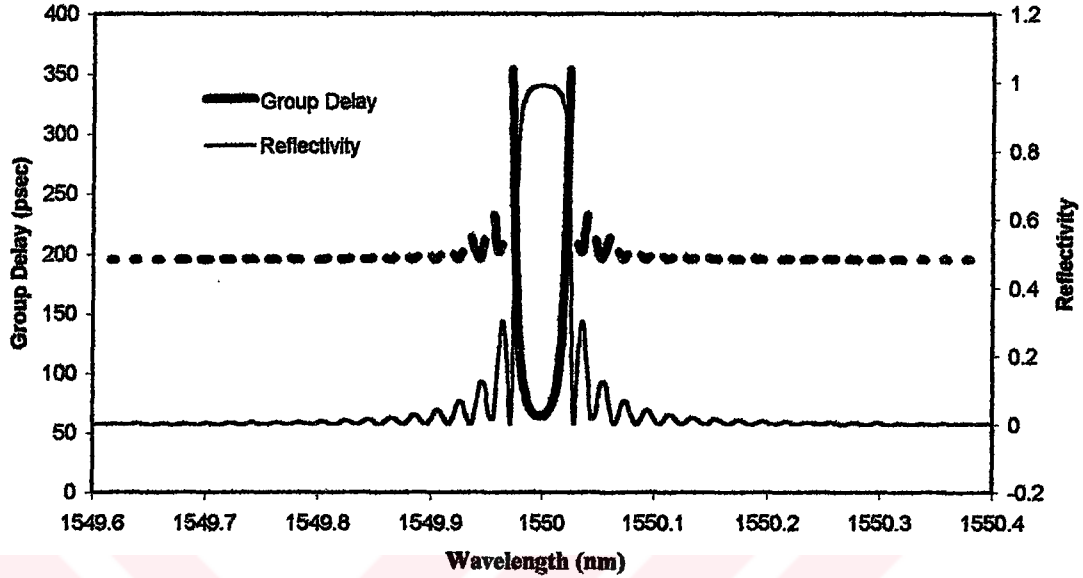


Figure 3.2 Reflectivity and phase characteristics for uniform FBG with 0.5 peak reflectivity

For comparison with the 0.5 peak reflectivity, the response of the uniform grating for 0.99 peak reflectivity is shown in Figure 3.3. The reflection spectrum takes the form of so-called *top-hat* shape in this case. The amplitude of the side-lobes increases as

expected. As expected, the value of  $\kappa_p$  is increased from  $0.499 \text{ cm}^{-1}$  (for 0.5 reflectivity) to  $1.721 \text{ cm}^{-1}$  for 99% reflectivity. In addition, the FWHM of the reflection spectrum is also increased ( $0.52 \text{ \AA}$ ) because of the top-hat shape.



**Figure 3.3** Reflectivity and group delay characteristics for uniform FBG with 0.99 peak reflectivity

### 3.2.2 Linearly Chirped Uniform FBGs

If the period of the sinusoidal variation of refractive index is reduced linearly ( $-1.9 \text{ \AA/cm}$ ) through the grating length, then the reflectivity and group delay response of the grating will be as in Figure 3.4. In this case, the reflection spectrum covers a wide range of wavelengths and reflectivity changes between 0.4 and 0.5. The FWHM of the spectrum is  $14.3 \text{ \AA}$  and the peak value of  $\kappa$  is  $3.48 \text{ cm}^{-1}$ . Compared to the uniform FBG, the chirped grating needs more index deformation to achieve the same amount of peak reflectivity. However, the way we apply the chirp is important. We consider it in such a way that the pitch corresponding to Bragg wavelength coincides with the center of the grating length, i.e. if the grating length is 4 cm; the pitch is  $\Lambda_0$  at the center (2 cm). The pitch is larger for  $L < 2 \text{ cm}$  and smaller for  $L > 2 \text{ cm}$ .

The reflectivity spectrum of this chirped grating has a ripple that is characteristic of unapodized gratings, as does the group delay. The strong ripple in the group delay plays an important role in pulse compression and shaping applications [53]. The ripple frequency becomes smaller towards the longer wavelengths.



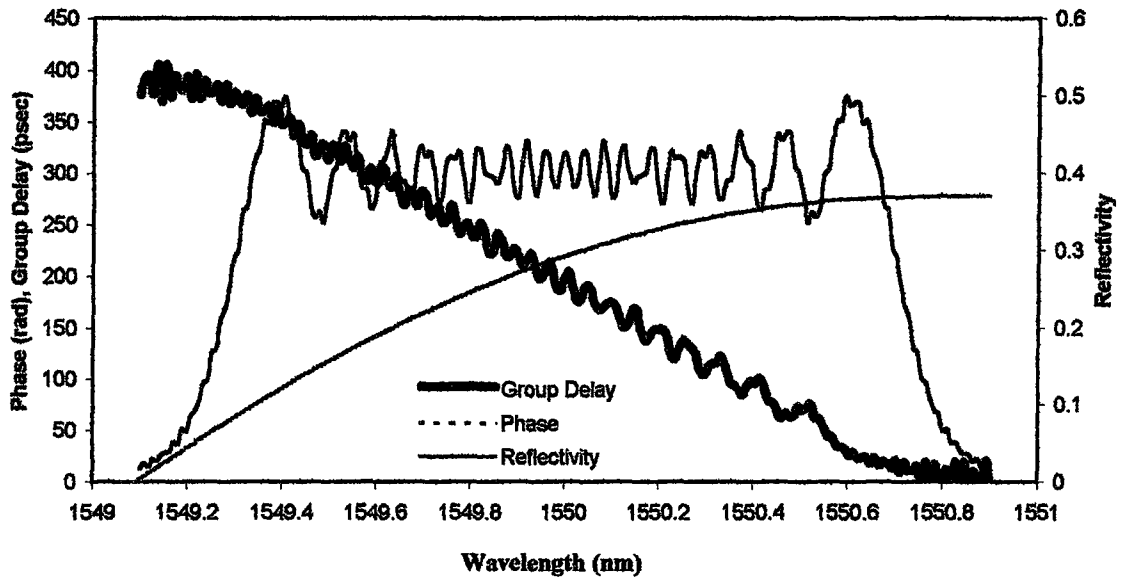


**Figure 3.4** Reflectivity, phase and group delay characteristics for linearly chirped uniform FBG with 0.5 peak reflectivity

This ripple is a consequence of the multiple reflections between the adjacent grating sections that has a constant amount of index deformation.

The response of a linearly chirped uniform grating with a 0.99 peak reflectivity is given in Figure 3.5. Similar to the uniform FBGs, the peak value of  $\kappa$  is increased to  $9.556 \text{ cm}^{-1}$  and the FWHM of the reflection spectrum becomes wider,  $16.1 \text{ \AA}$ . Peak wavelength of the reflection spectrum is shifted towards the shorter wavelengths (1549.45 nm) because of the DC averaged refractive index is more effective at lower wavelengths.

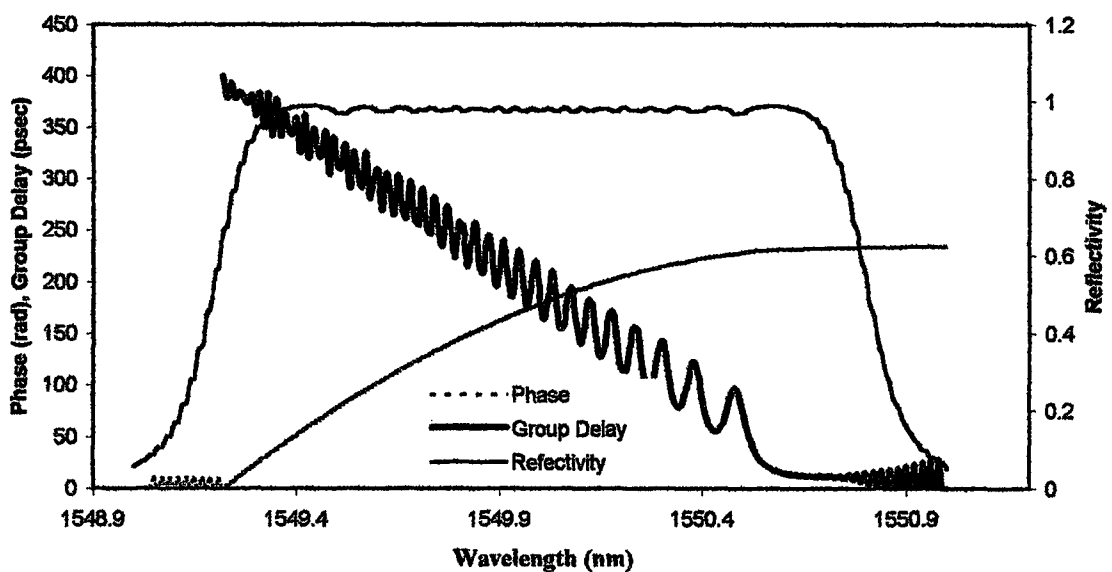


**Figure 3.5** Reflectivity, phase and group delay characteristics for linearly chirped uniform FBG with 0.99 peak reflectivity

### 3.2.3 Gaussian Apodized FBGs

The response of a Gaussian apodized FBG is shown in Figure 3.6. Although the spectrum is wider compared to that of uniform grating, there is no symmetric side-lobe structure around the main lobe. This is because the Fabry-Perot effect is eliminated by smoothly passing from the refractive index of the fiber core  $n_{co}$  to the deformation in the refractive index that produces grating. It can also be explained by the Fourier transform approach. As the profile of the index deformation is Gaussian, its Fourier transform must also be Gaussian as well. Our situation is the same, except there is a small side-lobe on the short wavelength side of the main lobe. This is because of the nonzero dc index change formed by the Gaussian shape deformation of the refractive index. This behavior is explained in detail in [50]. The peak of the reflection spectrum is also shifted to longer wavelengths (1550.036 nm) from the design wavelength because of the nonzero dc averaged refractive index change. More clearly, since  $\lambda_o = 2 n_{co} \Lambda$  and the pitch is constant, as the average refractive index  $n_{co}$  increases,  $\lambda_o$  increases as well. The discontinuity in the group delay curve is a result of the side-lobe where phase jumps up as shown in Figure 3.6. The peak  $\kappa_p$  value is  $1.46 \text{ cm}^{-1}$  that is almost 3 times larger than its value for the uniform grating, because of the Gaussian distribution instead of uniform deformation with  $0.499 \text{ cm}^{-1}$

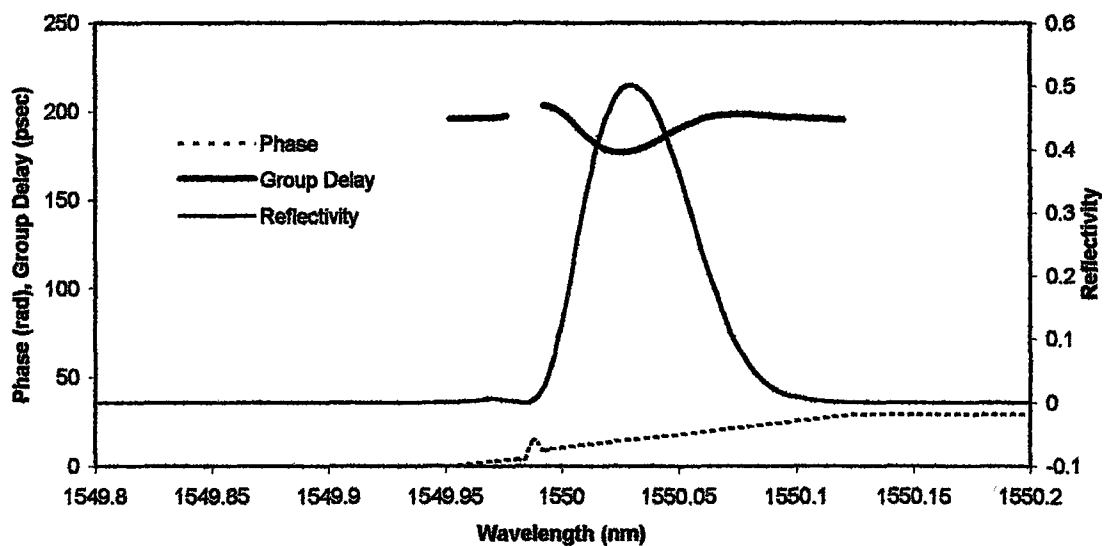


Figure 3.6 Reflectivity, phase and group delay characteristics for Gaussian apodized FBG with 0.5 peak reflectivity

The response of the 0.99 peak reflectivity Gaussian apodized grating is shown in Figure 3.7. Side-lobe suppression is reduced as the grating gets stronger and these side-lobes cause a nonlinear group delay.

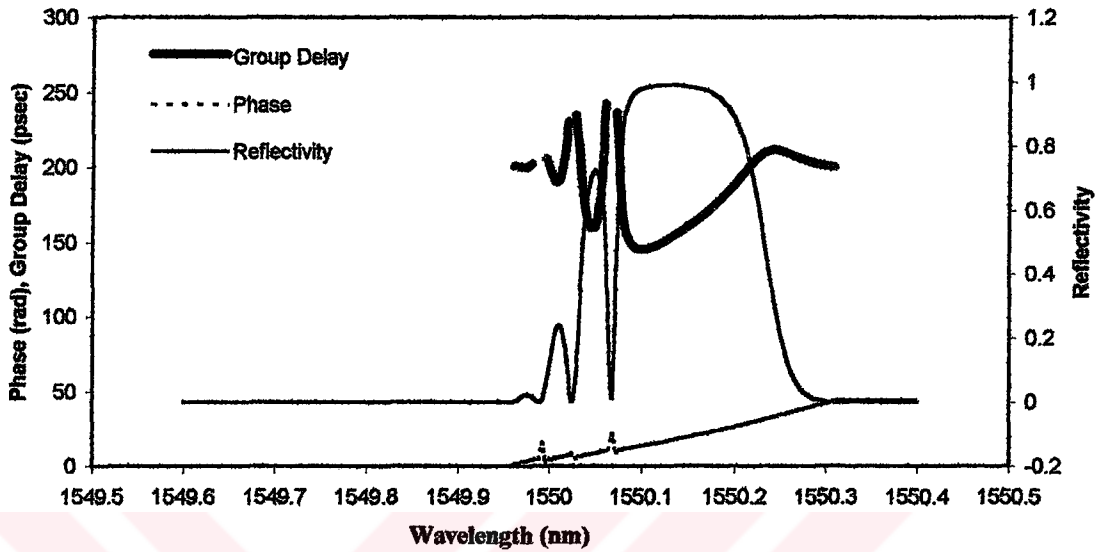
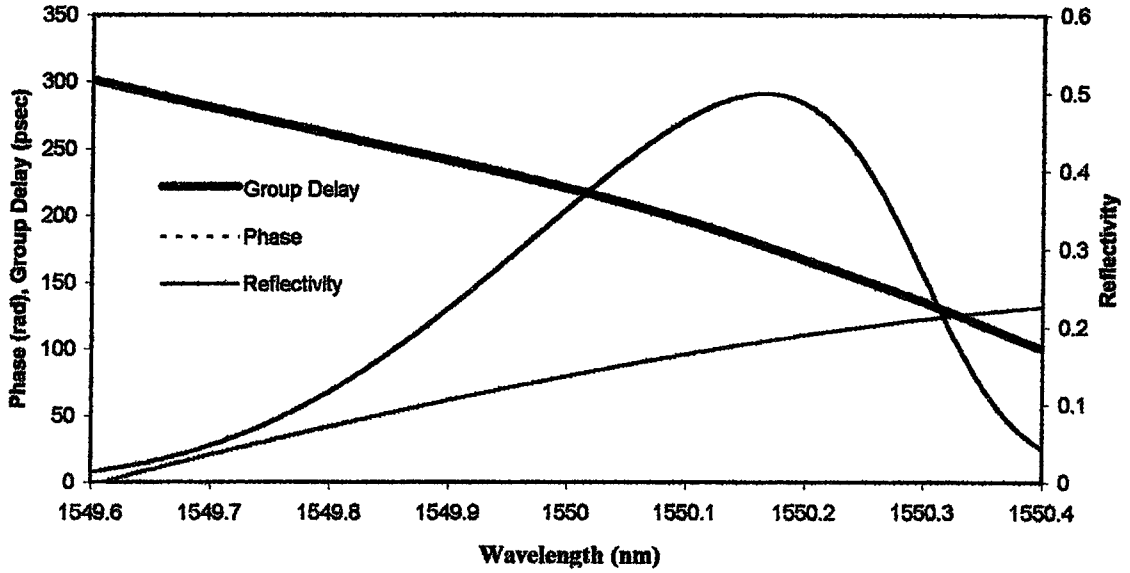


Figure 3.7 Reflectivity, phase and group delay characteristics for Gaussian apodized FBG with 0.99 peak reflectivity

### 3.2.4 Linearly Chirped Gaussian Apodized FBGs

If the grating is both linearly chirped and Gaussian apodized then the resulting reflection spectrum and group delay will be as shown in Figure 3.8. The reflection spectrum has only one lobe and the group delay curve is linear. Apodization suppresses the side-lobes in the reflection spectrum and ripples on the group delay curve [54] and chirping makes both the spectrum wider and the group delay linear. Neither apodization nor chirping could solve these problems alone. For example, a linearly chirped uniform grating has almost linear group delay characteristics with a small ripple. The most beneficial effect of the apodization in this case is the removal of the ripple in the group delay characteristics (see Figure 3.4 for comparison). The reflection spectrum is wider (FWHM 3.78 Å) compared to the uniform grating and its peak is shifted towards the longer wavelengths (1550.171 nm). The peak value of Gaussian  $\kappa$  is about  $3.958 \text{ cm}^{-1}$  indicating that the grating deformation must be higher than that of chirped gratings ( $3.48 \text{ cm}^{-1}$ ).



**Figure 3.8** Reflectivity, phase and group delay characteristics for linearly chirped Gaussian apodized FBG with 0.5 peak reflectivity

This spectrum is the one that is desired for the mode-locked Hybrid Soliton Pulse Source (HSPS) [18]. The group delay is almost linear. This results in wavelength dependent cavity length control in HSPS. By this property, it is possible to apply 2 to 3 GHz ranges of drive frequencies to the HSPS although it is designed to be mode-locked at 2.5 GHz. This mechanism is called *wavelength self-tuning* [18, 22]. It is a very useful tool for mode locking applications where no frequencies other than the cavity design frequency is allowed to operate.

The response of the linearly chirped Gaussian apodized FBG for 0.99 peak reflectivity is shown in Figure 3.9. The reflectivity in this response has a small side-lobe on the long wavelength side. This side-lobe is the result of the apodization and chirping that together forms a very strong grating ( $\kappa_p = 9.438 \text{ cm}^{-1}$ ). Short wavelengths travel further than the long wavelengths that immediately turn back, inside the grating.

Comparison of Figure 3.8 and Figure 3.9, and the other figures with the peak reflectivities of 0.5 and 0.99 shows that, as the reflectivity is increased, the grating gets stronger and possibility of side-lobe occurrence increases. This can be eliminated by the use of longer gratings. For HSPS applications, the peak reflectivity of the grating is around 0.3-0.7. Therefore, Figure 3.8 is the best choice (for the standard parameters, of course) for HSPS applications.

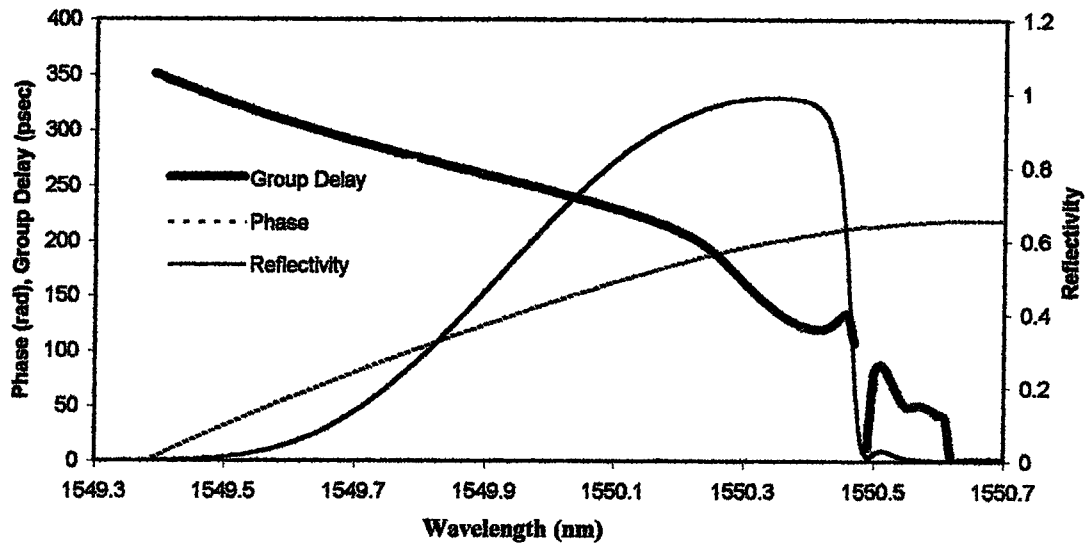


**Figure 3.9** Reflectivity, phase and group delay characteristics for linearly chirped Gaussian apodized FBG with 0.99 peak reflectivity

### 3.3 Conclusions

In this chapter, reflection spectrums and group delay curves of the fiber Bragg gratings has been explained and it has already been described in [23].

As seen from the results, it is possible to design a chirped, apodized grating such that the group delay response is almost perfectly linear. It was shown that using this grating the group delay is linearized and side-lobes is eliminated since the apodization suppresses the side-lobes in the reflection spectrum and ripples on the group delay curve and chirping makes both the spectrum wider and the group delay linear.

## CHAPTER 4

### MODELING OF HYBRID SOLITON PULSE SOURCE (HSPS)

#### 4.1 Introduction

A laser is basically an oscillator working at optical frequencies. In order to get an oscillator to work, both *amplification* and *feedback* are needed. In a semiconductor laser the amplification (gain) is provided by injecting current into the active region, and the feedback is usually provided simply by reflection from the facets. Two situations must be considered:

1. steady-state operation in which the gain must be equal to loss, and
2. dynamic behavior described by a set of rate equations

These are important concepts that form the basis for the understanding of the properties of semiconductor lasers.

An important property of semiconductor lasers is that they are pumped simply by passing a current through the laser structure. This is in contrast to other laser types which are usually pumped either optically or by an electrical discharge. The basic semiconductor laser structure consists of a narrow bandgap material, the active region (usually undoped) placed between two wide bandgap regions, and the confinement or passive regions, one n-doped, the other p-doped. This is known as a double heterostructure.

Despite their differences the basic principle of operation is the same for each type of laser. Laser action is the result of three key processes. These are photon absorption, spontaneous emission, and stimulated emission. These three processes are represented by the simple two-energy-level diagrams in Figure 4.1, where  $E_1$  is the ground-state energy and  $E_2$  is the excited-state energy. According to Planck's law, a transition between these two states involves the absorption or emission of a photon of energy  $h\nu_{12}=E_1-E_2$ . Normally the system is in the ground state. When a photon of

energy  $h\nu_{12}$  impinges on the system, an electron in state  $E_1$  can absorb the photon energy and be excited to state  $E_2$ , as shown in Figure 4.1a. Since this is an unstable state, the electron will shortly return to the ground state, thereby emitting a photon of energy  $h\nu_{12}$  as seen in Figure 4.1b. This occurs without any external stimulation and is called *spontaneous emission*. These emissions are isotropic and of random phase, and thus appear as a narrowband Gaussian output.

The electron can also be induced to make a downward transition from the excited level to the ground-state level by an external stimulation. As shown in Figure 4.1c, if a photon of energy  $h\nu_{12}$  impinges on the system while the electron is still in its excited state, the electron is immediately stimulated to drop to the ground state and give off a photon energy  $h\nu_{12}$ . This emitted photon is in phase with the incident photon, and the resultant emission is known as *stimulated emission*.

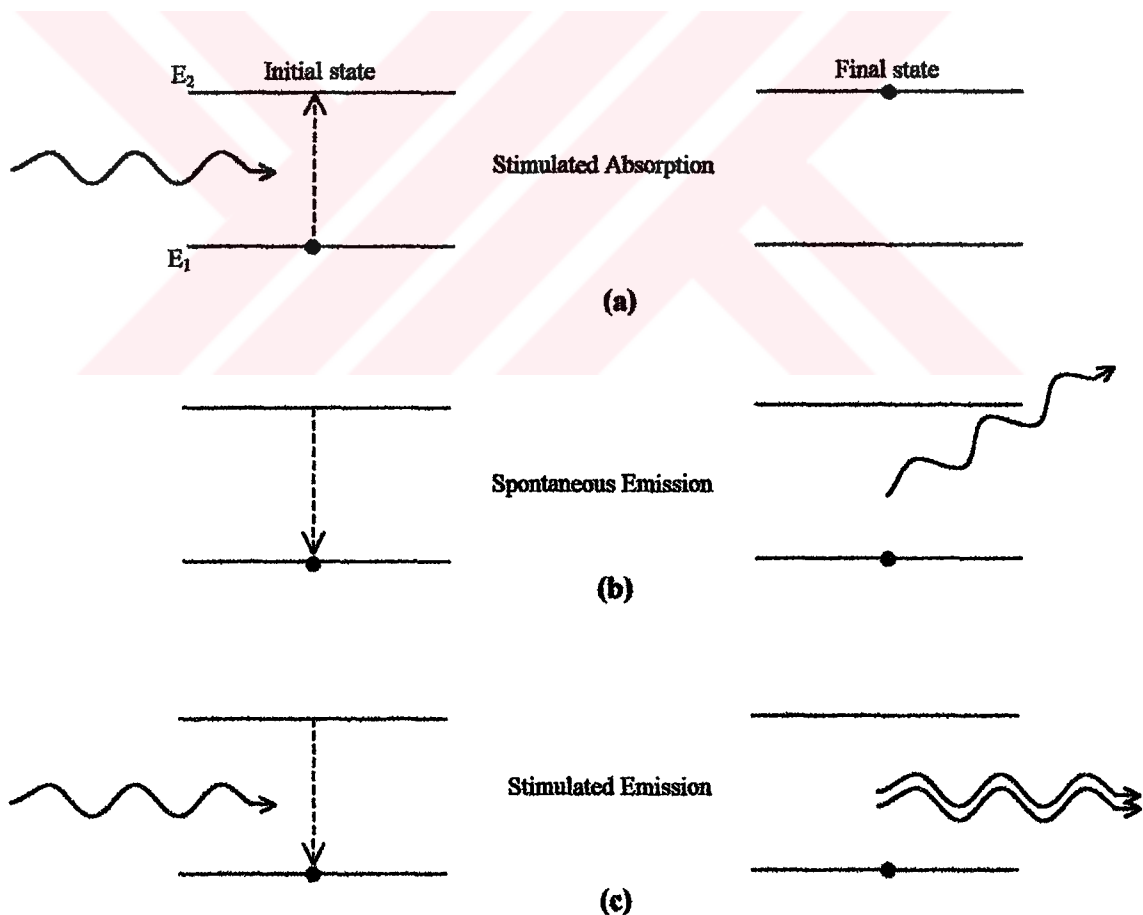


**Figure 4.1** Energy level diagram illustrating (a) absorption, (b) spontaneous emission and (c) stimulated emission. The black dot indicates the state of the atom before and after the transition

In thermal equilibrium the density of excited electrons is very small. Most photons incident on the system will therefore be absorbed, so that stimulated emission is essentially negligible. Stimulated emission will exceed absorption only if the population of the excited states is greater than that of the ground state. This condition is known as *population inversion*. Since this is not an equilibrium condition, population inversion is achieved by various "pumping" techniques. In a semiconductor laser, population inversion is accomplished by injecting electrons into the material at the device contacts to fill the lower energy states of the conduction band.

The relationship between light output and diode drive current is given Figure 4.2. At low diode currents only spontaneous radiation is emitted. A dramatic and sharply defined increase in the light output occurs at the lasing threshold current ( $I_{th}$ ). As this transition point is approached, the spectral range and the beam width both narrow with increasing drive current. Above threshold, stimulated emission becomes the dominant mechanism for photon production, and so a linear increase in forward current, giving as it does a linear increase in carrier concentration, should also give a linear dependence of light output on current above threshold. This indeed does happen to a reasonable degree, but because the stimulated process is so much more efficient than the spontaneous one the slope of the light output-current curve is much steeper. As shown in Figure 4.2 region (a) is the region where spontaneous emission dominates, and laser behaves as an LED. Region (b) is non-linear transition region, where the spontaneous and stimulated emission regimes are both significant and the brightness of the device increases rapidly. Such a device is called a superradiant LED. The stimulated emission region, characterized by a steep slope of light output/current is shown in region (c).

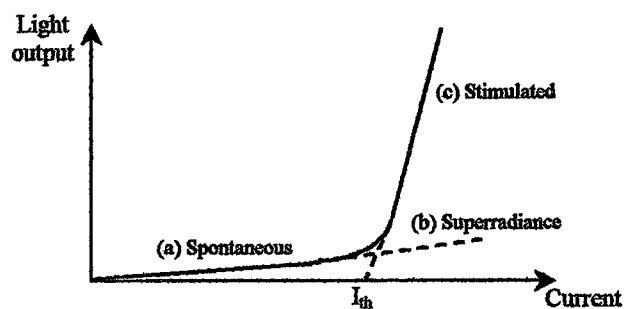


Figure 4.2 Light output-current characteristic of an ideal semiconductor laser



## 4.2 Mode-Locked Lasers

Output of a laser consists of a number of very closely spaced, discrete frequency components (that is very narrow spectral lines) covering a moderately broad spectral range. The discrete components are called *laser modes* and the spectral range they occupy is approximately the fluorescent linewidth of the atomic transition giving rise to the laser output. A mode of a laser resonator can be defined as a self-consistent optical field configuration which re-produces itself after one round-trip in the cavity. The waves within the laser resonator form standing wave patterns with the mirrors as modes in an exactly analogous way to a sound wave within an organ pipe or a microwave inside a cavity. Stationary waves of frequency

$$f = \frac{nc_o}{2L_1n_1} \quad (4.1)$$

(where  $c_o$  is the velocity of light in vacuum (cm/sec),  $L_1$  is the laser diode length (cm),  $n_1$  is the active region refractive index, and  $n$  is any integer) which are directed along the laser axis are called *longitudinal* (or *axial*) *modes* of the laser. Longitudinal modes have the same form of spatial energy distribution in a transverse plane (parallel to the mirrors), but have different axial distributions corresponding to different numbers of half-wavelengths of light along the axis of the resonator. These longitudinal modes are spaced in frequency by  $c_o/2L_1n_1$ . Usually, quite a few longitudinal modes will lie within the range where laser gain exceeds the threshold cavity loss. The output of the laser will then consists of several spectral lines. These lines have finite bandwidth, determined by the losses of the cavity.

Apart from longitudinal modes, there also, exists a set of solutions for the light energy inside a resonator which correspond to different energy distributions in a plane transverse to the axis. These solutions are called the *transverse modes* of the resonator. For each transverse mode there exists a set of longitudinal modes and vice versa. Electric field configurations which exist in laser cavities are of the transverse electromagnetic type, represented as  $TEM_{qmn}$  where  $q$  is the longitudinal mode order number (giving the number of half-wavelengths of light along the axis of the resonator), and  $m, n$  are the transverse mode order numbers.

One of the conditions of perfect longitudinal mode-locking, as will be explained later, is to have only one transverse mode oscillating. In order to obtain single transverse mode excitation, it is necessary to use some device which will give high losses to all transverse modes but the desired one. Since higher order transverse modes spread further from the resonator axis, the easiest way to accomplish single transverse mode operation is to insert into the laser cavity a circular aperture whose size is such that the fundamental  $TEM_{00}$ - mode experiences little diffraction loss while higher order modes suffer appreciable attenuation.

Mode-locked semiconductor laser diodes offer the possibility of producing small, and reliable sources of stable subpicosecond pulses over a wide wavelength ranges and with moderate peak powers. They can be used in telecommunication systems for time-division multiplexing or for high-bit-rate systems using an external modulator [55]. Semiconductor lasers are ideal candidates for use in practical commercial electrooptic sampling systems [56] due to their small size, low cost, low noise, and small timing jitter in comparison to the use of the more complex and less reliable sources such as pulse-compressed YAG lasers.

The theory of mode-locking can be explained that the initial electromagnetic radiation field in the laser cavity is a sum of individual fields of the oscillating longitudinal modes with random phases and therefore has a noise-like fluctuating waveform. When the phase difference between adjacent modes becomes fixed, the fluctuating pattern changes and acquires the characteristics of a well defined single pulse. The process of fixing the frequency separation and phase differences of the excited modes can be defined as "mode-locking". The single pulse which is produced as a result of mode-locking will naturally be very narrow. At the same time, its peak power will be enormous because all of the laser energy will have been concentrated in the single surviving pulse.

Mode-locking of any laser can be achieved by modulating either loss or the gain of the laser. There are mainly two methods for this purpose, "passive mode-locking" and "active mode-locking". A third type of mode-locking, called "self-locking", is also possible. In self-locking, ultrashort pulses can be obtained spontaneously without employing an external modulator or other mode-locking element. However, due to somewhat unstable and uncontrollable nature of self-locking, this method is

very rarely used. The active mode-locking method usually gives rise to continuous operation, whereas passive mode-locking produces Q-switched "giant" pulse output.

Short pulse generation from mode-locked semiconductor lasers is currently a very active research area. Ultrashort pulses by actively mode-locking semiconductor lasers cannot be generated with solitary diodes, which have typical lengths of a few hundred micrometers, since the modulation frequency of the external driver corresponding to this length is of the order of a few hundred GHz. Mode-locking therefore requires an external cavity, formed by placing one or more mirrors at a distance from the partially reflecting facets of the laser diode. The external cavity is usually a few tens of centimeters long whereas diode cavity is only several hundred microns long. A schematic diagram of the composite cavity, which is comprised of the external mirror and the laser diode, is shown in Figure 4.3.

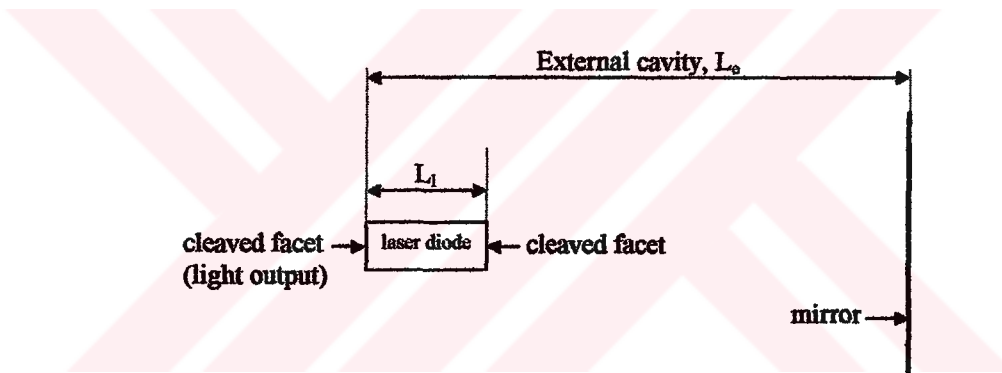


Figure 4.3 The composite semiconductor laser cavity

The round trip time of the laser cavity, in seconds, is simply, given as

$$T = \frac{2L_1 n_1}{c_0} \quad (4.2)$$

where  $L_1$  is the laser diode length (cm),  $n_1$  is the active region refractive index, and  $c_0$  is the velocity of light in vacuum (cm/sec). The corresponding drive frequency,  $f_m$  (in Hz), is simply equal to the inverse of the round trip time. From equation (4.2), a 400  $\mu\text{m}$  with  $n_1$  being 3.6, corresponds to a drive frequency of about  $\sim 100$  GHz. However, the relaxation time of the population inversion is of the order of a fraction of a nanosecond, therefore if the modulation period is made equal to the round-trip period of the diode, the population inversion will not be able to respond to the modulation. In other words, the modulation frequency should be low enough so that

the population will show an instantaneous response, and this is possible only if the modulation period is much larger than the relaxation time of the population inversion. Furthermore, we would not have a practical source of sinusoidally varying voltage at ~100 GHz. Both of these obstacles are overcome by incorporating an external mirror, which would increase the round-trip time considerably. The round-trip period for the composite cavity is

$$T = \frac{2(L_e - L_l) + 2L_l n_l}{c_o} \quad (4.3)$$

where  $L_e$  is the length of the external cavity. If  $L_e=15$  cm, then  $T=10^{-9}$  seconds and the modulation frequency is 1 GHz which is now within limits. On the other hand, it is also important that the external cavity should not be made too long, otherwise spontaneous emission will build up excessively between the mode-locked pulses and hence background noise will be increased needlessly.

There are basically four reasons why an external cavity is employed for mode-locking purposes [57]. An external cavity is used to that

1. The gain will be able to follow the modulating current, (otherwise, since the relaxation time of the population inversion is not very short, a modulation current of too high a frequency will not be felt effectively by the active medium.)
2. The frequency of modulation of the injected current will be within practically realizable limits,
3. The number of longitudinal modes oscillating will be increased,
4. The threshold of lasing will be reduced.

Active mode-locking of laser diodes is achieved by exciting the laser diode simultaneously with DC and RF current at a frequency equal to the inverse round-trip period. Mode-locking can also be performed by modulating the injection current of the laser diode at a frequency that is an integer multiple of the fundamental frequency corresponding to the external cavity length. This technique is known as harmonic mode-locking [58] and is used to generate short-duration mode-locked

pulses at very high repetition rates [59]. The DC bias is usually greater than the threshold current, although mode-locking has also been achieved by using a bias that is considerably less than the threshold current or exactly equal to it.

The composite cavity has two kinds of axial modes: those belonging to the diode cavity, and those belonging to the external cavity. The modulation imposed by the diode cavity modes presents a serious problem. Usually the diode cavity modes cannot be phase-locked, hence only those external cavity modes that are situated within the frequency spread of a single diode cavity mode can thus be successfully mode-locked. If more than one diode cavity mode is excited (as is usually the case) then the phases of the external cavity modes which are within the frequency spread of one diode cavity mode will not have a fixed relationship with the phases of the external cavity modes within the frequency spread of an adjacent diode cavity mode. This means that the oscillating external cavity modes will be locked in groups and complete mode-locking of all oscillating axial external cavity modes will not occur. This will give rise to a light pulse which is not transform-limited and therefore the width of this pulse will be relatively broad, that is, much broader than allowed by the oscillation bandwidth.

For successful mode-locking of laser diodes, the oscillation spectrum should be restricted to a single longitudinal mode. Therefore, the Fabry-Perot resonator resulting from the partially reflecting laser diode mirrors should be removed. The schemes that used in practice to modify the oscillation spectrum of the laser diodes can be summarized [57] as:

1. An intra-cavity Fabry-Perot etalon acting as an optical filter that should have a bandwidth just large enough to allow only one diode cavity mode passes through.
2. A reflecting diffraction grating can be used instead of a plane mirror and an etalon.
3. Tilting the stripe of the laser diode or polishing the facet of the laser diode at the Brewster angle can suppress the total internal reflections at the diode facet and hence removes all the diode cavity modes.

4. Anti-reflection (AR) coating of one of the laser diode facets will remove all the diode cavity modes.

Mode-locked HSPS is a kind of external cavity lasers where FBG is used as external cavity. Structure of this laser is explained next sections.

### 4.3 Structure of the HSPS

The HSPS shown in Figure 4.4 is demonstrated first by Morton et al. [18,60-61]. It is made up of a multi-quantum well (MQW) semiconductor laser, a fiber and a fiber Bragg grating. One facet of diode is the high reflectivity (HR) coated for improved cavity Q and the other is anti-reflection (AR) coated to allow coupling to the external cavity and suppress Fabry-Perot modes. The light from the AR coated facet is coupled to the fiber Bragg grating reflector. The field in this system travels between the HR coated laser end and effective cavity length of the grating. The output power is taken through the grating.

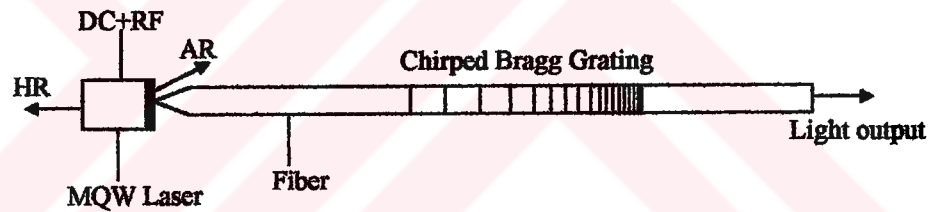


Figure 4.4 Schematic of HSPS

For the modeling of a multi-section system like HSPS, coupled-mode equations must be modified in such a way that they include gain, loss and noise in the laser. In addition, since a field is not inserted in the cavity but is a result of the lasing, one cannot write the initial conditions at a definite point (i.e. the fields entering and leaving that point), instead, the fields at any time is assumed to be known and their values along the sections are calculated progressively.

The solution of the coupled-mode equations are written in Chapter 2 as

$$F = \left[ \cosh(\gamma z) - j \frac{\delta}{\gamma} \sinh(\gamma z) \right] F_0 - \left[ j \frac{\kappa}{\gamma} \sinh(\gamma z) \right] R_0 \quad (4.4)$$

$$R = \left[ j \frac{\kappa}{\gamma} \sinh(\gamma z) \right] F_0 + \left[ \cosh(\gamma z) + j \frac{\delta}{\gamma} \sinh(\gamma z) \right] R_0 \quad (4.5)$$

In order to calculate the progressive fields, either  $F_0$  and  $R$  or  $R_0$  and  $F$  are assumed to be known. Let us assume  $F_0$  and  $R$  are known, and write  $R_0$  and  $F$  in terms of these known fields:

$$F = \frac{\gamma F_0 - j \kappa \sinh(\gamma z) R}{\gamma \cosh(\gamma z) + j \delta \sinh(\gamma z)} \quad (4.6)$$

$$R_0 = \frac{-j \kappa \sinh(\gamma z) F_0 + \gamma R}{\gamma \cosh(\gamma z) + j \delta \sinh(\gamma z)} \quad (4.7)$$

These equations can be written in matrix form as

$$\begin{bmatrix} F \\ R_0 \end{bmatrix} = \frac{1}{\gamma \cosh(\gamma z) + j \delta \sinh(\gamma z)} \begin{bmatrix} \gamma & -j \kappa \sinh(\gamma z) \\ -j \kappa \sinh(\gamma z) & \gamma \end{bmatrix} \begin{bmatrix} F_0 \\ R \end{bmatrix} \quad (4.8)$$

In order to model the complete HSPS, each section must be modeled separately since the parameters in Equation 4.13 are different for each section.

#### 4.4 Laser Diode Model

Internal loss of a laser diode is intrinsic and is given by

$$\alpha_{\text{int}} = \alpha = \Gamma \alpha_a + (1 - \Gamma) \alpha_c + \alpha_{\text{sc}} \quad (4.9)$$

where  $\Gamma$  is the confinement factor,  $\alpha_a$  is the absorption loss (mainly due to free carrier absorption),  $\alpha_c$  is the cladding absorption loss and  $\alpha_{\text{sc}}$  is the scattering loss at the junction interfaces. The total internal loss of a MQW laser can be typically taken as  $25 \text{ cm}^{-1}$  [22].

There are no mirror losses in the laser cavity because one side of the laser diode is HR coated and the other side is AR coated. The light propagates between the HR coated laser end and the FBG.

In order to include effects of the laser gain and loss,  $\beta$  and  $\gamma$  must be written as

$$\beta = \beta_o + (\delta + jg - j\alpha) = \beta_o + (\delta + jg_{net}) \quad (4.10)$$

$$\gamma^2 = \kappa^2 + (g_{net} - j\delta)^2 \quad (4.11)$$

Here  $g$  is the gain for the field (note that the intensity gain is  $2g$ ) and is defined as

$$g = \frac{\Gamma \alpha_o (N - N_o)}{2(1 + \varepsilon P)} \quad (4.12)$$

where  $\varepsilon$  is the gain compression factor (also referred to as gain saturation).  $\alpha$  is the internal field loss (note that the intensity loss is  $\alpha_{int}$  given by  $2\alpha$ ) and  $g_{net}$  is the net field gain in the laser diode when the loss is subtracted from the gain. In addition, the spontaneous emission to the fields must be taken into account and it must be put into the coupled forward and reverse-propagating fields. This can be in the form of a Gaussian noise added into the coupled-mode equations [46]

$$\begin{bmatrix} F \\ R_o \end{bmatrix} = \frac{1}{\gamma \cosh(\gamma z) - (g_{net} - j\delta) \sinh(\gamma z)} \begin{bmatrix} \gamma & -j\kappa \sinh(\gamma z) \\ -j\kappa \sinh(\gamma z) & \gamma \end{bmatrix} \begin{bmatrix} F_o \\ R \end{bmatrix} + \begin{bmatrix} s_f \\ s_r \end{bmatrix} \quad (4.13)$$

Here  $s_f$  and  $s_r$  are the spontaneous noise coupled to the forward and reverse waves, respectively and will be explained later.

#### 4.4.1 Nonradiative Recombination

The carriers can recombine in the active region by several mechanism: nonradiative recombination, bimolecular recombination, and Auger processes. The latter involves carrier scattering between different energy bands. In addition to these processes stimulated recombination takes place under lasing.

The nonradiative recombination process can be divided into two main groups: Auger recombination, and defect and surface recombination.



Auger recombination is the major recombination in the narrow-band semiconductor lasers such as InGaAsP. There are mainly three types of Auger process: Band-to-band, phonon-assisted and trap-assisted. Phonon-assisted process is only important at high temperatures and the trap-assisted process is very important in heavily doped semiconductors with a high concentration of traps above and below the Fermi level. Therefore, these processes are generally ignored and the relatively dominant band-to-band Auger process can be included in the rate equation model as

$$R_A = C_A N^3 \quad (4.14)$$

where  $C_A$  is the Auger recombination coefficient in  $\text{cm}^6\text{s}^{-1}$ . Measured values of  $C_A$  lie in the range  $1-7.5 \times 10^{-29} \text{ cm}^6\text{s}^{-1}$  for conventional InGaAsP lasers and higher for quantum well structures. For this reason we use  $C_A = 10 \times 10^{-29} \text{ cm}^6\text{s}^{-1}$  in this work.

The other nonradiative recombination type is the defect and surface recombination. This process occurs, as the name implies, at the cleaved facets of the laser diode and the imperfections that occurs during the manufacturing process. The Auger recombination is effective at high injection levels since it is proportional to the cubic power of the carrier density, whereas the recombination at defects and surfaces is dominant at low injection levels since it is proportional to the carrier density as given below:

$$R_{nr} = \frac{N}{\tau_n} \quad (4.15)$$

where  $\tau_n$  is the carrier lifetime and  $N$  is the carrier density. The numerical value of carrier lifetime is on the order of a few tens nanoseconds. This recombination type can also be expressed in terms of a nonradiative recombination constant  $A$ , such that

$$R_{nr} = AN \quad (4.16)$$

where  $A$  is in  $\text{s}^{-1}$ .

#### 4.4.2 Radiative Recombination and Spontaneous Emission

Spontaneous emission plays an important role in laser dynamics especially before the threshold is reached. Its inclusion in the carrier rate equation is in the form of total spontaneous emission rate given by

$$R_{sp} = B N^2 \quad (4.17)$$

where  $B$  is the radiative recombination coefficient (which lies in the range  $0.7 - 1.5 \times 10^{-10} \text{ cm}^3 \text{ s}^{-1}$ ) and  $N$  is the carrier density. However, the peak value of the spontaneous emission spectrum have been found to change with the carrier injection level as

$$R_{sp} = (B_0 - B_1 N) N^2 \quad (4.18)$$

where  $B_0$  and  $B_1$  are the radiative (or bimolecular) recombination coefficients. The value of  $B_0$  is in the range of  $0.5 - 0.7 \times 10^{-10} \text{ cm}^3 \text{ s}^{-1}$  and the ratio of  $B_0$  to  $B_1$  typically lies in the range  $1.7 - 2.2 \times 10^{19}$ . The effect of  $B_1$  is similar to the effect of Auger recombination hence, we took  $B = 1 \times 10^{-10} \text{ cm}^3 \text{ s}^{-1}$  in this work. The relations given above are only valid for the carrier rate equation since they are in terms of the densities rather than fields.

#### 4.4.3 Carrier Rate Equations

In order to relate the field with the photon density generated in the laser diode, a carrier rate equation must be written. The rate equation of the carrier density is taken as

$$\frac{dN(z,t)}{dt} = \frac{I(t)}{qV} - R(N) - \frac{a_0(N(z,t) - N_0)}{1 + \varepsilon P(z,t)} v_g P(z,t) + F_N \quad (4.19)$$

where  $t$  is time,  $N$  is the carrier density,  $I(t)$  is the current injected to the active region (both DC and RF parts),  $q$  is the electron charge,  $V$  is the volume of the active region,  $P(z,t)$  is the photon density and it is proportional to  $|F|^2 + |R|^2$ ,  $N_0$  is the carrier density at transparency,  $\varepsilon$  is the gain compression coefficient,  $a_0$  is the differential gain

coefficient (intensity) and  $F_N$  is the carrier density. The fields  $F$  and  $R$  are normalized so that  $|F|^2$  and  $|R|^2$  has the unit of photon density.

The total recombination rate of carrier concentration  $R(N)$  given by

$$R(N) = \left( \frac{N}{\tau_n} + B N^2 + C_A N^3 \right) \quad (4.20)$$

where  $\tau_n$  is the carrier lifetime and  $C_A$  is the Auger recombination coefficient. It can also be written in a different form such that

$$R(N) = (A N + B N^2 + C_A N^3) \quad (4.21)$$

The current  $I(t)$ , comprised of a dc part  $I_{dc}$  and an ac part having a magnitude of  $I_{rf}$ , is given as

$$I(t) = I_{dc} + I_{rf} \sin(2\pi f_m t) \quad (4.22)$$

where  $f_m$  is the drive (or modulation) frequency.

#### 4.4.4 Carrier Induced Refractive Index Change

Since there is no grating in the laser diode section, there will be no coupling between the forward- and reverse-propagating fields, i.e.  $\kappa_L = 0$ . However, the effective refractive index of the laser diode  $n_{eff}$  differs from the nominal value  $n_{eff0}$  by

$$n_{eff} = n_{eff0} + \Delta n \quad (4.23)$$

where  $\Delta n$  is the change in the refractive index due to the change in the carrier density  $\Delta N$ . The change in refractive index due to a change in the carrier density is given as

$$\Delta n = - \frac{\lambda_o}{4\pi} \Gamma \alpha_h \alpha_o \Delta N(z, t) \quad (4.24)$$

where  $\alpha_h$  is the linewidth enhancement factor. In this case, the real part of the propagation constant differs from the Bragg condition by

$$\delta_L = \frac{2\pi}{\lambda_o} \Delta n \quad (4.25)$$

and  $\gamma$  for the laser diode becomes

$$\gamma_L = \sqrt{(g_{net} - j\delta_L)^2} \quad (4.26)$$

The net field gain of the laser diode  $g_{net}$  is defined in terms of the field gain and the internal loss of the laser diode  $\alpha_{int}$  (intensity) as

$$g_{net} = g - \alpha_{int} / 2 \quad (4.27)$$

Assuming that the laser diode is divided into  $M_L$  equal sections with  $dz = v_g dt$ , the solution of coupled-mode equations can be written as

$$\begin{bmatrix} F_{i+1} \\ R_i \end{bmatrix} = \frac{1}{\gamma_L \cosh(\gamma_L \Delta z) - (g_{net} - j\delta_L) \sinh(\gamma_L \Delta z)} \begin{bmatrix} \gamma_L & 0 \\ 0 & \gamma_L \end{bmatrix} \begin{bmatrix} F_i \\ R_{i+1} \end{bmatrix} + \begin{bmatrix} s_f \\ s_r \end{bmatrix} \quad (4.28)$$

The matrices must be multiplied by each other for  $i = 0$  to  $i = M_L - 1$  to find the fields at the end of the laser diode.

#### 4.5 Fiber Model

There is no gain, no loss, no coupling and no spontaneous emission incorporated in the fiber. Although the fiber itself is a lossy medium, the loss can be neglected since it is a few centimeters long ( $\alpha_F < 0.2$  dB/km for conventional fibers). Similarly, the effect of fiber dispersion is also neglected since the fiber is typically 2-3 cm long. The only thing to do with this section is to provide a progress to the fields, i.e.

$$\begin{bmatrix} F_{i+1} \\ R_i \end{bmatrix} = \begin{bmatrix} 1 \\ 1 \end{bmatrix} \begin{bmatrix} F_i \\ R_{i+1} \end{bmatrix} \quad (4.29)$$

Similar to the laser sections, the fiber is divided into  $M_F$  sections and calculations are carried out from  $i = 0$  to  $i = M_F - 1$ .

#### 4.6 Grating Model

The grating is made up of a single mode fiber of a few centimeters long. In this case, the medium can be assumed to be lossless as in the fiber model, and there is no gain in this medium. The parameters that must be known are  $\kappa$  and  $\delta$  for the grating. The coupling coefficient of a Gaussian apodized grating is written as

$$\kappa_G = \kappa_p \exp\left(\frac{-4 \ln 2}{FWHM_\kappa^2} z^2\right) \quad (4.30)$$

where the peak value of the  $\kappa$  is given by

$$\kappa_p = \frac{\pi \delta n}{\lambda} m \quad (4.31)$$

If the grating is not apodized, simply  $\kappa_G = \kappa_p$ .

The deviation of  $\beta_0$  from the real part of  $\beta$  is given as  $\delta$  for the uniform gratings. For the most general grating type we must take into account the effect of chirping, hence, conventional  $\delta$  is replaced by the dc self-coupling coefficient

$$\hat{\sigma}_G = \delta_G + \sigma + \frac{4\pi n_\infty}{\lambda_o^2} C z \quad (4.32)$$

Similar to the situation of  $\kappa_G$  for uniform and apodized gratings, if the grating is uniform, then  $\hat{\sigma}_G = \delta_G$  which is given as

$$\delta_G = \beta - \beta_0 = 2\pi n_\infty \left( \frac{1}{\lambda} - \frac{1}{\lambda_o} \right) \quad (4.33)$$

For the most general case,  $\gamma$  can be written as

$$\gamma_G = \sqrt{\kappa_G^2 - \hat{\sigma}_G^2} \quad (4.34)$$

For these grating parameters, the solution of coupled-mode equations can be written as (noting that  $dz = L/M$ )

$$\begin{bmatrix} F_{i+1} \\ R_i \end{bmatrix} = \frac{1}{\gamma_G \cosh(\gamma_G \Delta z) + j\delta_G \sinh(\gamma_G \Delta z)} \quad (4.35)$$

$$\begin{bmatrix} \gamma_G & -j\kappa_G \sinh(\gamma_G \Delta z) \\ j\kappa_G \sinh(\gamma_G \Delta z) & \gamma_G \end{bmatrix} \begin{bmatrix} F_i \\ R_{i+1} \end{bmatrix}$$

#### 4.7 Laser-Fiber Interface

The physical and section models for the laser-fiber interface is given in Figure 4.5 and Figure 4.6. Although the right hand side of the laser diode is AR coated to provide maximum field transfer to the fiber, it is not perfectly transmittive and practically the field reflection coefficient of the AR coating is taken as 0.01. In addition, due to the laser-fiber interface (i.e. splicing loss), some of the fields cannot be coupled totally passing from laser-to-fiber and fiber-to-laser. This phenomenon is expressed in our model by the coupling factor  $\eta$  whose magnitude is assumed to be 0.8 for both laser-to-fiber and fiber-to-laser field transfer.

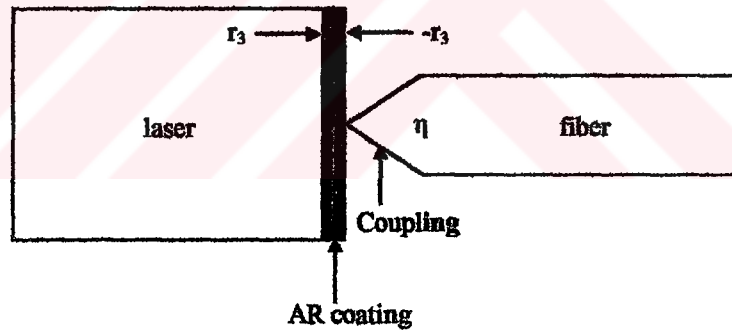


Figure 4.5 Physical model of the laser-fiber interface

When only an AR coating with a laser-to-fiber reflectivity  $r_3$  exists in the laser-fiber interface, the reflections and transmissions of the forward- and backward-traveling waves are shown in Figure 4.5. They can be related to the known fields  $F_i$  and  $R_{i+1}$  (assuming no multiple reflections) as

$$F_{i+1} = (1 - r_3)F_i - r_3 R_{i+1} \quad (4.36)$$

$$R_i = r_3 F_i + (1 + r_3)R_{i+1}$$

Since the coupling takes place after the AR coating, the forward traveling wave passes through the laser-fiber interface first and then it is multiplied by  $\eta$ . The reflected part of the forward field is only multiplied by  $r_3$  since it is reflected from AR coating, before coupling. The reverse traveling wave, however, experiences coupling first and then passes through the AR coating, so multiplied by  $\eta(1+r_3)$ . The reflected part of the reverse traveling wave first passes coupling, then reflected back from AR coating and finally couples to the fiber, as a result, multiplied by  $-\eta^2 r_3$ . The final diagram of transmitted and reflected fields, in case where both AR coating and coupling efficiency present, is given in Figure 4.6. The final field values can be written as

$$F_{i+1} = \eta(1 - r_3)F_i - \eta^2 r_3 R_{i+1} \quad (4.37)$$

$$R_i = r_3 F_i + \eta(1 + r_3)R_{i+1}$$

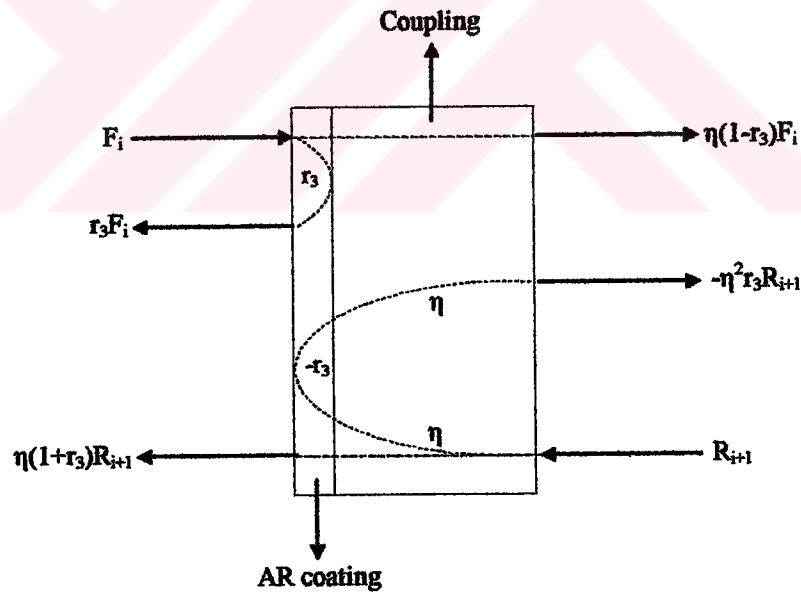


Figure 4.6 Section model of the laser-fiber interface and field reflections

These equations should be included in the model in order to observe the effects of AR coating and laser-fiber bi-directional light coupling efficiency.

#### 4.8 Boundary Conditions

In order to include the effects of reflecting mirror (reflectivity  $r_1$ ) of the laser diode at the left end, and the field reflected back from the Bragg grating, the following boundary conditions are taken into account:

$$F_1 = r_1 R_1 \tag{4.38}$$

$$R_M = r_2 F_M$$

In these equations, subscript 1 (for the fields) denotes the first section of the laser diode (left side) and  $M$  denotes the last section. The reflectivity at the end of the grating,  $r_2$ , is taken as zero, since there is no reflective element after the grating.





## **CHAPTER 5**

### **SPONTANEOUS AND CARRIER NOISE IN MODE- LOCKED HSPS**

#### **5.1 Introduction**

In this chapter, noise in the laser will be described. Then, the output of HSPS will be investigated for all types of fiber Bragg gratings when spontaneous emission and carrier noise are taken into account. At the mode-locking frequency of 2.5 GHz, the full width at half maximum (FWHM) of output pulses, and their TBP will be investigated in order to see HSPS is properly mode-locked or not. The range of frequencies through which the HSPS mode-locked properly will also be identified. All of these are made to show how the noise affects the operation of mode-locked HSPS.

The fiber grating peak reflectivity is taken 0.5. The standard parameters for the mode- locked HSPS program are given in Table 5.1.

Table 5.1 Standard parameters for the HSPS mode-locking program

Parameter	Symbol	Standard value	Unit
Differential gain	$a_0$	$10.0 \times 10^{-16}$	$\text{cm}^2$
Gain saturation parameter	$\varepsilon$	$2.0 \times 10^{-17}$	$\text{cm}^3$
Spontaneous emission parameter	$\beta_{sp}$	$5.0 \times 10^{-5}$	
Field coupling factor	$\eta$	0.8	-
Field reflectivity of AR coating	$r_3$	0.01	-
Field reflectivity of left facet	$r_1$	0.9	-
Field reflectivity of right facet	$r_2$	0.0	-
Refractive index of unmodified fiber core	$n_{co}$	1.46	-
Refractive index of the gain medium	$n_1$	3.3	-
Total internal loss	$\alpha_{int}$	25	$\text{cm}^{-1}$
Linewidth enhancement factor	$\alpha_h$	2	
Confinement factor	$\Gamma$	0.1	-
Nonradiative recombination coefficient	A	$4.0 \times 10^8$	$\text{s}^{-1}$
Bimolecular recombination coefficient	B	$1.0 \times 10^{-10}$	$\text{cm}^3 \text{s}^{-1}$
Auger recombination coefficient	$C_A$	$10.0 \times 10^{-29}$	$\text{cm}^6 \text{s}^{-1}$
Carrier lifetime	$\tau_n$	$0.8 \times 10^{-9}$	s
Transparency carrier density	$N_o$	$1.2 \times 10^{18}$	$\text{cm}^{-3}$
Reference carrier density for refractive index	$N_{rf}$	$2.0 \times 10^{18}$	$\text{cm}^{-3}$
Mode-locking frequency	$f_m$	2.5	GHz
DC bias current	$I_{dc}$	6	mA
RF current amplitude	$I_{rf}$	20	mA
Length of the laser diode	$L_1$	$2.5 \times 10^{-2}$	cm
Width of the laser diode	w	$1.0 \times 10^{-4}$	cm
Thickness of the laser diode	d	$5.0 \times 10^{-6}$	cm
Operating wavelength	$\lambda$	$1.55 \times 10^{-4}$	cm
Speed of light in vacuum	$c_o$	$3.0 \times 10^{10}$	cm/sec
Length of grating*	L	4.0	cm
Length of fiber*	$L_f$	2.06	cm
Effective cavity length	$L_{eff}$	4.06	cm

\*: for 2.5 GHz.

TEC YÜKSEK LİSANS ENSTİTÜSÜ  
MÜHÜRÜ

## 5.2 Noise in the Laser

Laser diodes are intrinsically noisy devices because of the quantum nature of the light. Even when the laser is biased at a constant current, with negligible fluctuations, the output of a semiconductor laser exhibits fluctuations in its phase and in its intensity. These laser noise fluctuations are known as the Langevin noise forces that describe the fluctuations of a system.

Langevin noise term is to determine the quantum nature of the photon absorption and emission process. They play crucial roles in determine the linewidth and amplitude fluctuations of semiconductor laser. The various sources of noise are added as random Langevin forces, which are added to the wave equations of the electric field and to the rate equation of the carrier density. These equations are solved to determine how the system variables fluctuate. From these equations and the correlation relations between the Langevin noise functions, one can determine the noise spectra of the output field such as the intensity noise and phase noise.

*Spontaneous emission* and electron-hole recombination, which one known as *shot noise* are two fundamental noise mechanisms. The fluctuations in carrier number result from the processes of generation and recombination. Spontaneous emission results from a sum of contributions from throughout the laser.

All of these noises can be assumed to have Gaussian distribution with zero average and for the noise analysis; correlations relations between them must be determined. In the steady- state operation, the correlation of two variables does not depend on time ( $t$ ). This is known as *stationary*. The noise processes are considered to be stationary and ergodic.

### 5.2.1 Spontaneous Emission Noise

Spontaneous emission is the main source of noise. It occurs in all directions and over a broad range of optical frequencies. Spontaneous emission events instantaneously add increments to the laser field, each increment having a magnitude of unity and a random phase angle. It perturbs both amplitude and phase in a random manner. The intensity fluctuations are characterized by the relative intensity noise (RIN) and they lead to a limited signal-to-noise ratio (SNR). The phase fluctuations lead to a finite

spectral linewidth when semiconductor lasers are operated continuously at a constant current. These fluctuations can affect the performance of lightwave systems and it is important to estimate their magnitude. As seen in Figure 5.1, it has two parts, imaginary part causes the phase fluctuations and real part causes the amplitude fluctuations.

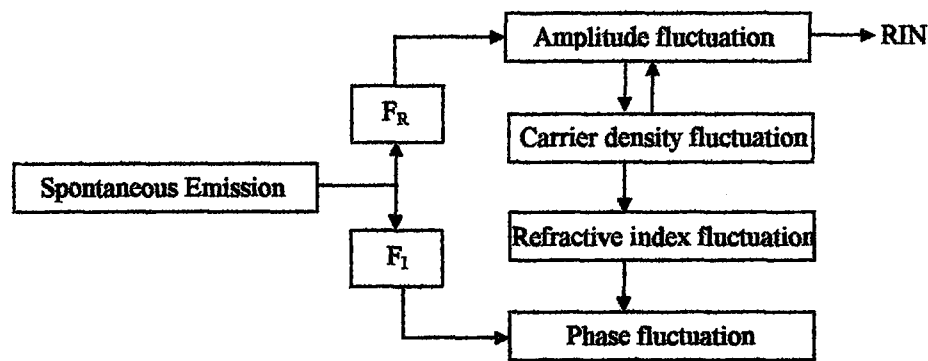


Figure 5.1 Noise diagram in laser

Phase noise in the optical field of a laser is due to spontaneous photons coupled into the lasing mode. Two mechanisms contribute to phase fluctuations:

- (a) First term is due to spontaneous emission. Each spontaneously emitted photon changes the optical phase by a random amount. When spontaneous photon is injected into the lasing mode, both the amplitude and phase of the optical field in the mode undergo changes. These changes can be described in terms of the field associated with the injected photon combined by phasor addition with the field of the lasing mode. The fluctuations in phase of the total field due to a large number of random spontaneous emission events give rise directly to phase noise as seen in figure.
- (b) The second term shows that fluctuations in the carrier populations also lead to a phase change as seen in Figure 5.1. Each spontaneously emitted photon changes the laser power, which changes the gain (or equivalently the carrier populations); this in turn affects the refractive index (or the optical path length) and consequently the optical phase. The resulting delayed phase fluctuations are affected by relaxations oscillations and leads to peaks at the relaxation oscillation frequency as well as a broadening of the central peak by a  $1 + \alpha_h^2$ .

The spontaneous noise  $s_f$  and  $s_r$  coupled to the forward and reverse waves in equations 4.12 and 4.20, are assumed to have equal amplitudes, e.g. [46],

$$s(z,t) = s_f(z,t) = s_r(z,t) \quad (5.1)$$

Spontaneous emission is assumed to have a Gaussian distribution and to satisfy the correlation:

$$\begin{aligned} \langle s(z,t) s^*(z',t') \rangle &= \beta_{sp} \frac{R_{sp}}{v_g} \delta(t-t') \delta(z-z') \\ \text{and} & \\ \langle s(z,t) s(z',t') \rangle &= 0 \end{aligned} \quad (5.2)$$

Here  $\beta_{sp}$  is the spontaneous coupling factor for each mode,  $R_{sp} = B N^2/L_l$  is the bimolecular recombination per unit length contributed to the spontaneous emission,  $B$  is the radiative (or bimolecular) recombination coefficient and  $v_g$  is the group velocity of light in the cavity.

### 5.2.2 Carrier Noise

The carrier noise  $F_N$  in equation 4.13 results from two kinds of processes and can be written in the following way [62]

$$F_N(z,t) = F_{nr}(z,t) - F_s(z,t) \quad (5.3)$$

The first term  $F_{nr}$  on the right-hand side of (5.3) describes the noise of injection current and the noise caused by nonradiative recombination of carriers. This noise term is not correlated with the process of spontaneous emission and, is a Gaussian white noise with correlation [62]:

$$\langle F_{nr}(z,t) F_{nr}(z',t') \rangle = (I/qV + N/\tau_n) \delta(t-t') \delta(z-z') \quad (5.4)$$

Here, first term determines noise of injection currents and it is neglected for this analysis. Second term  $F_s$  on the right-hand side of (5.3) results from radiative recombination and is therefore correlated to the spontaneous emission. In fact, since every emitted photon implies the recombination of one electron hole pair, the carrier

noise resulting from photon emission is proportional to the fluctuation of the optical intensity.

The autocorrelation for  $F_N(z,t)$  and the cross correlation between  $F_N$  and  $s(z,t)$  becomes

$$\langle F_N(z,t)F_N(z',t') \rangle = \left( I/qV + N/\tau_n + \frac{a_o(N-N_o)}{1+\epsilon P} v_g P \right) \delta(t-t')\delta(z-z') \quad (5.5)$$

and

$$\langle F_N(z,t)s(z',t') \rangle = -\beta_{sp} R_{sp} \frac{a_o(N-N_o)}{1+\epsilon P} P \delta(t-t')\delta(z-z') \quad (5.6)$$

### 5.3 Relative Intensity Noise

RIN describes the laser's maximum available amplitude range for signal modulation and serves as a quality indicator of laser devices. RIN can be thought of as a type of inverse carrier-to-noise-ratio. Since the emitted optical power  $P$  of a laser exhibits noise, which causes it to fluctuate around its steady- state value, it can be written as

$$P(t) = \langle P \rangle + \delta P(t) \quad (5.7)$$

where  $\langle P \rangle$  is the mean power. The RIN relates the noise of the optical power  $\delta P(t)$  to  $\langle P \rangle$  and it is defined as the ratio of the mean square intensity fluctuations to the mean intensity squared of the laser output as shown the equation

$$RIN = \frac{\langle \delta P^2(t) \rangle}{\langle P \rangle^2} = \frac{\langle P(t)^2 \rangle}{\langle P \rangle^2} - 1 \quad (5.8)$$

where  $\langle P(t)^2 \rangle$  is the mean square optical power. The noise processes are considered to be stationary and ergodic, so that the symbol  $\langle \rangle$  denotes either the ensemble or the time average.

In order to find RIN the power spectral density of the noise must be determined firstly. At this point we need the Wiener-Khintchine theorem, which states that the power spectral density of a function is the Fourier transform of its autocorrelation function.

In this study, we calculate the spectral density of noise and then the value of RIN. To redefine the RIN as:

$$\frac{RIN}{\Delta f} = \frac{2S_{sp}(w)}{\langle P \rangle^2} \text{ dB/Hz} \quad (5.9)$$

$S_{sp}(f)$  is the spectral density of noise (*in a  $\Delta f$  bandwidth*) at a specified frequency. Note that the effective bandwidth is  $2\Delta f$  since we must include both positive and negative frequencies.

#### 5.4 Mode- Locked HSPS Results for Different FBG Types

In this section, the output of the mode-locked HSPS is given with and without noise for all grating types (uniform, linearly chirped uniform, Gaussian apodized and linearly chirped Gaussian apodized). DC and RF currents applied to the laser diode are 6 and 20 mA, respectively. The pulsewidth and the width of the corresponding spectrum are determined in order to calculate the TBP of the pulses.

##### 5.4.1 Output of HSPS for Linearly Chirped Gaussian Apodized FBG

Reflection spectrum, group delay and phase curves for linearly chirped Gaussian apodized grating were given in Figure 3.8. Transform-limited pulses from mode-locked HSPS with linearly chirped Gaussian apodized FBG are obtained over a tuning range of 1 GHz (2-3 GHz) around fundamental mode-locking frequency without noise and with spontaneous noise. This range was found 850 MHz in [22]. As shown in Figure 5.2, HSPS produces an output pulse without noise that has pulsewidth of 45.38 ps, spectral width of 8.68 GHz, and TBP of 0.394 at the fundamental mode-locking frequency of 2.5 GHz.

An output pulse with spontaneous noise that has a pulsewidth of 40.55 ps, spectral width of 8.6 GHz and a TBP of 0.349 at the fundamental mode-locking frequency is shown in Figure 5.3.

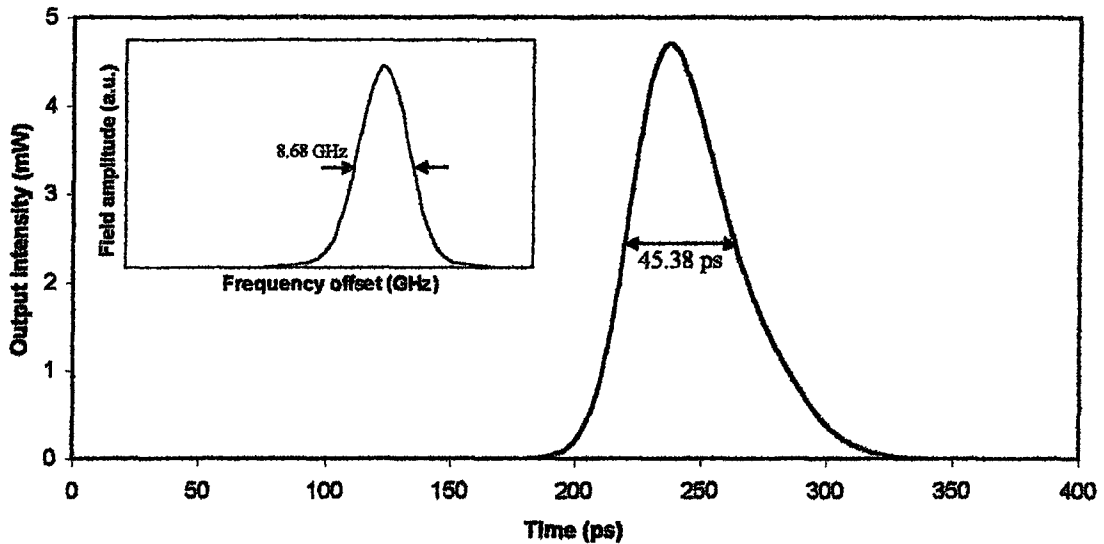


**Figure 5.2** Output intensity and field spectrum of mode-locked HSPS for linearly chirped Gaussian apodized FBG without noise at the mode-locking frequency of 2.5 GHz

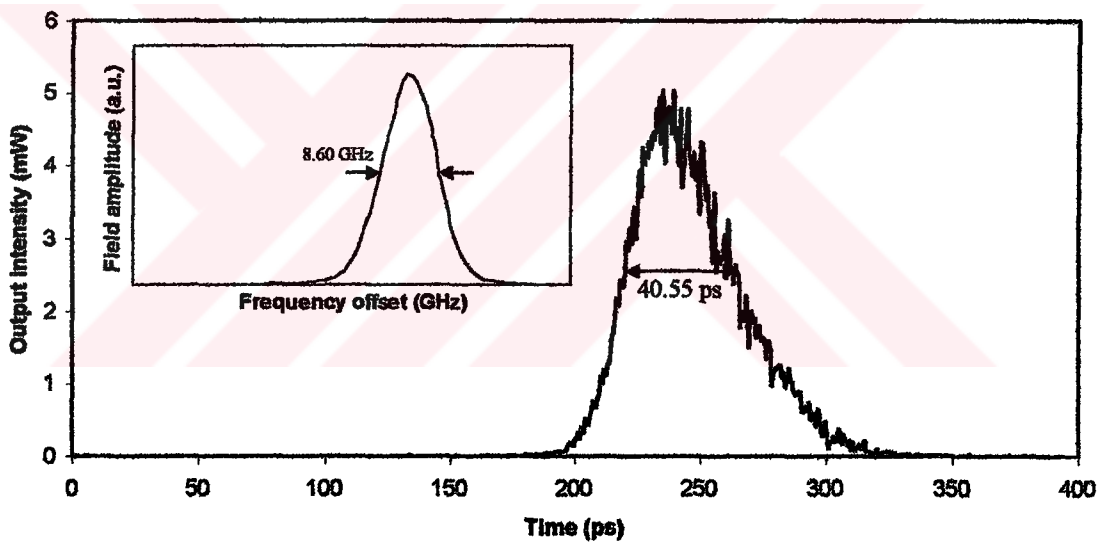


**Figure 5.3** Output intensity and field spectrum of mode-locked HSPS for linearly chirped Gaussian apodized FBG with spontaneous noise at the mode-locking frequency of 2.5 GHz

If carrier noise is considered, in this case, transform-limited pulses are not generated only at the mode-locking frequencies of 2.1 GHz and 2.3 GHz. A typical transform-limited output pulse that has a pulsewidth of 47.19 ps, spectral width of 8.65 GHz and TBP of 0.408 at the fundamental frequency is shown in Figure 5.4.

Transform-limited pulses are not only generated at the fundamental mode-locking frequency of 2.5 GHz if HSPS includes both spontaneous and carrier noise and Figure 5.5 shows output intensity of HSPS for this case. As seen in figure pulsewidth



is 1.278 ps, spectral width is 8.80 GHz and TBP is 0.011. These results are not suitable for soliton transmission system.

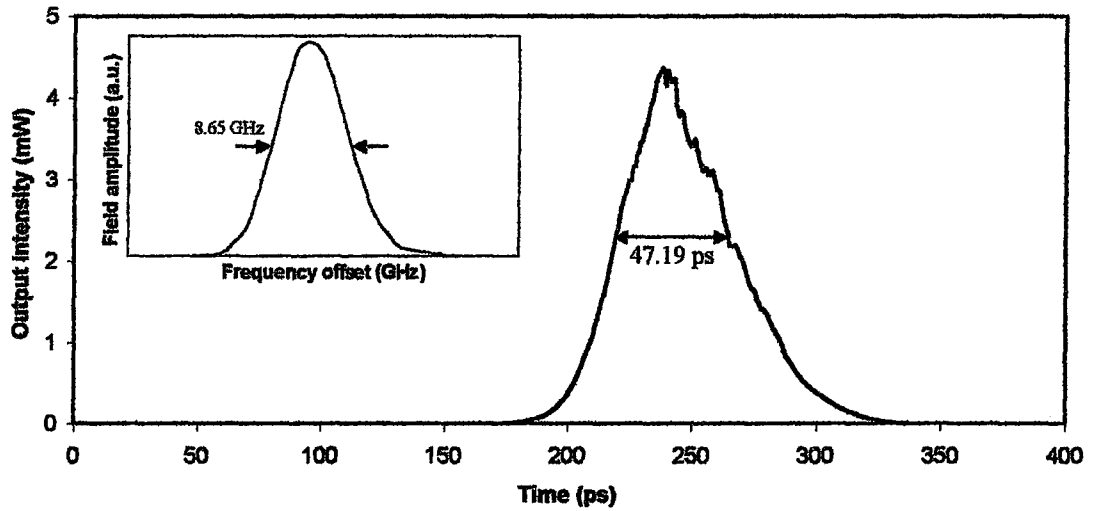


**Figure 5.4** Output intensity and field spectrum of mode-locked HSPS for linearly chirped Gaussian apodized FBG with carrier noise at the mode-locking frequency of 2.5 GHz

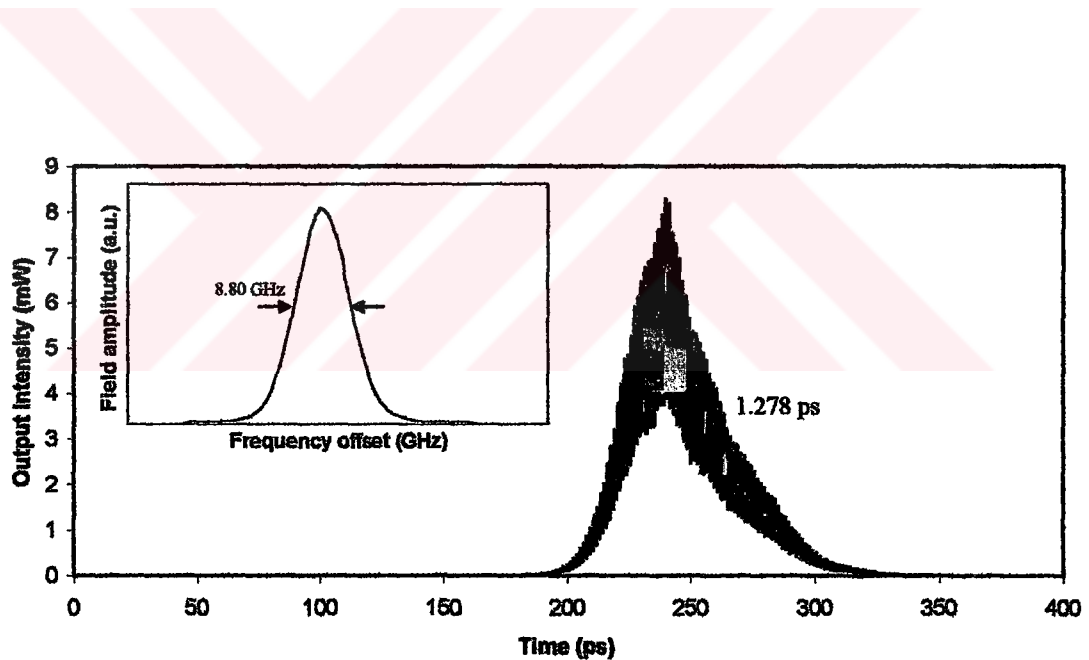


**Figure 5.5** Output intensity and field spectrum of mode-locked HSPS for linearly chirped Gaussian apodized FBG with spontaneous and carrier noise at the mode-locking frequency of 2.5 GHz

#### 5.4.2 Output of HSPS for Linearly Chirped Uniform FBG

The reflection spectrum of the linearly chirped uniform grating is given in Figure 3.4. Mode-locked HSPS utilizing linearly chirped uniform FBG produces output pulses that are transform-limited over a tuning range of 1.1 GHz (2-3.1 GHz) around the fundamental mode-locking frequency without any noise. It was experimentally showed that HSPS with linearly chirped uniform FBG could properly be mode-locked over an unusual frequency range of 2.1-2.8 GHz [18]. For this case, pulsewidth of output pulse is 45.69 ps, spectral width is 8.73 GHz, and TBP is 0.374 at the fundamental mode-locking frequency of 2.5 GHz as shown in Figure 5.6.

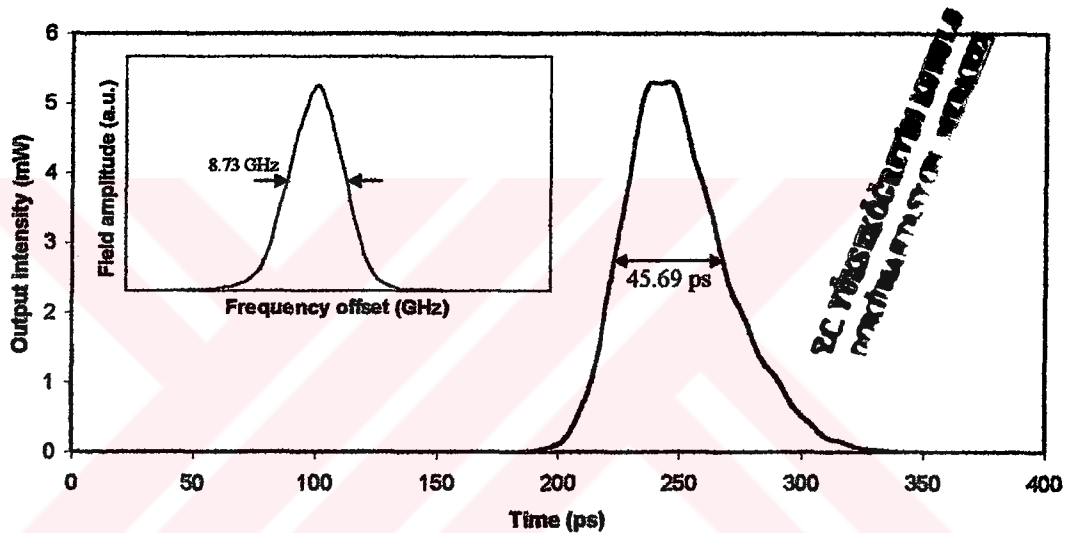


Figure 5.6 Output intensity and field spectrum of mode-locked HSPS for linearly chirped uniform FBG without noise at the mode-locking frequency of 2.5 GHz

Mode-locking range of 1.1 GHz where transform-limited pulses are generated is also found if spontaneous and both spontaneous and carrier noise is added in HSPS. Figure 5.7 shows output pulse of HSPS with spontaneous noise at the fundamental mode-locking frequency. As seen in figure output pulse has a pulsewidth of 34.23 ps, spectral width of 9.07 GHz and TBP of 0.399.

Carrier noise affects the output pulse of HSPS only at the fundamental mode-locking frequency of 2.5 GHz and 2 GHz. At the fundamental mode-locking frequency output pulse that has pulsewidth of 0.792 ps, spectral width of 8.34 GHz and TBP of 0.007 is shown in Figure 5.8. These results are not proper for practical applications.

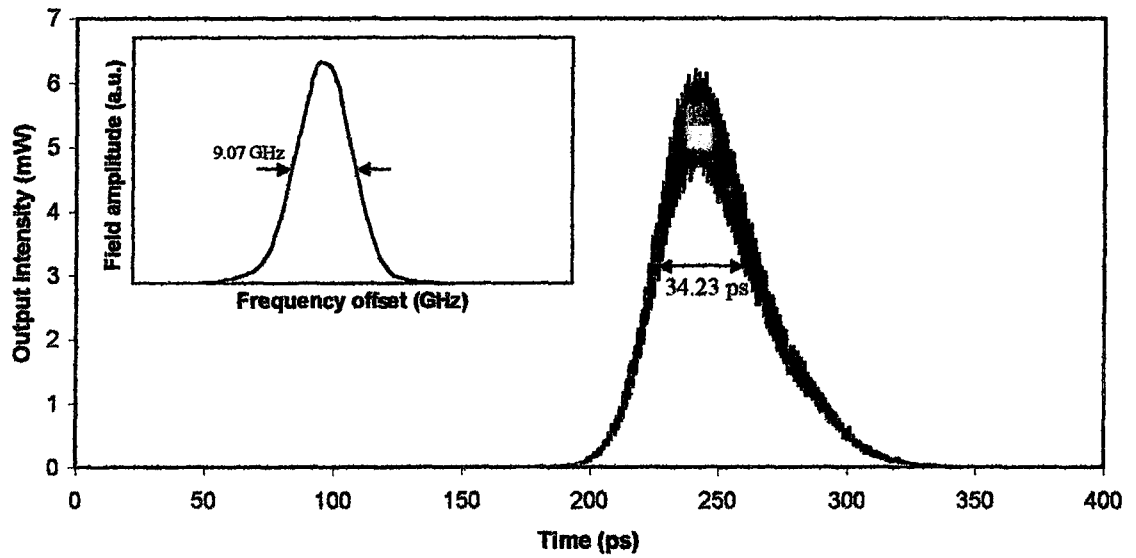


Figure 5.7 Output intensity and field spectrum of mode-locked HSPS for linearly chirped uniform FBG with spontaneous noise at the mode-locking frequency of 2.5 GHz

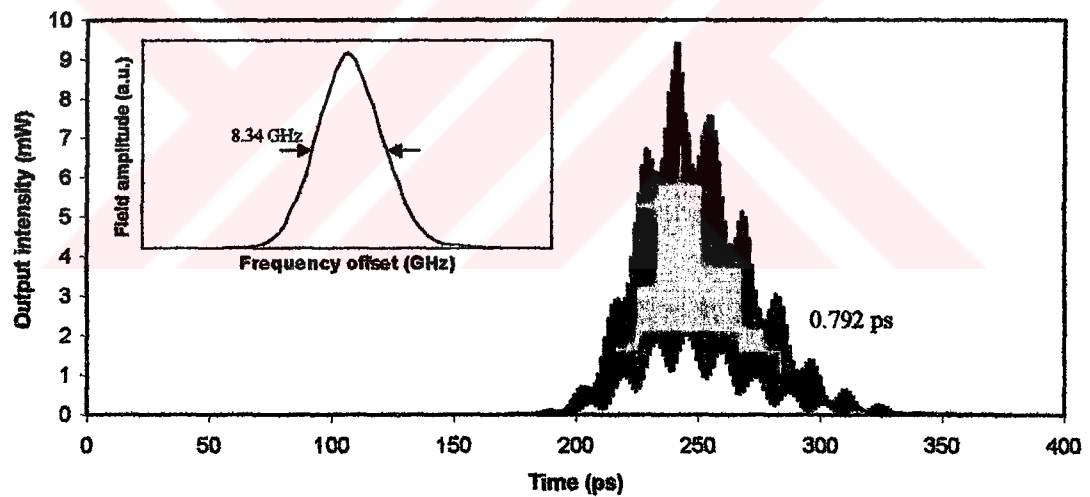
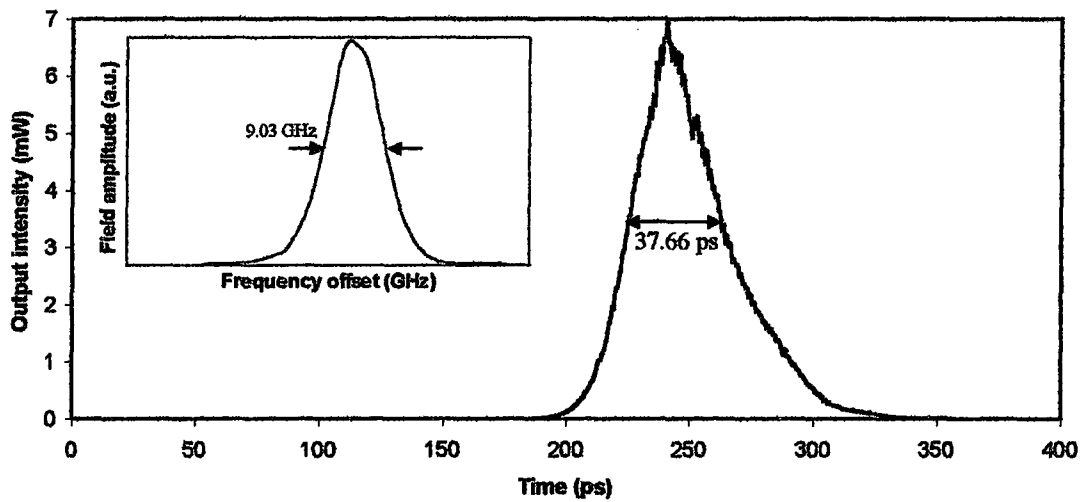


Figure 5.8 Output intensity and field spectrum of mode-locked HSPS for linearly chirped uniform FBG with carrier noise at the mode-locking frequency of 2.5 GHz

Output pulse of HSPS is given in Figure 5.9 at the mode-locking frequency of 2.5 GHz if both noises are considered. In this case, pulsewidth is 37.66 ps, spectral width is 9.03 GHz and TBP is 0.340 at this frequency.



**Figure 5.9** Output intensity and field spectrum of mode-locked HSPS for linearly chirped uniform FBG with spontaneous and carrier noise at the mode-locking frequency of 2.5 GHz

### 5.4.3 Output of HSPS for Gaussian Apodized FBG

The results show that mode-locked HSPS with Gaussian apodized FBG produces output pulses that are not transform-limited over a tuning range of 900 MHz (2-2.9 GHz) around the fundamental mode-locking frequency without noise and with spontaneous noise. Both of case transform-limited pulses that have TBP of 0.5 or less are only generated at mode-locking frequencies of 2.1, 2.2 and 2.3 GHz. An output pulse without noise having a pulse width of 63.11 ps, spectral width of 6.39 GHz and TBP of 0.403 at mode-locking frequency of 2.1 GHz is shown in Figure 5.10.

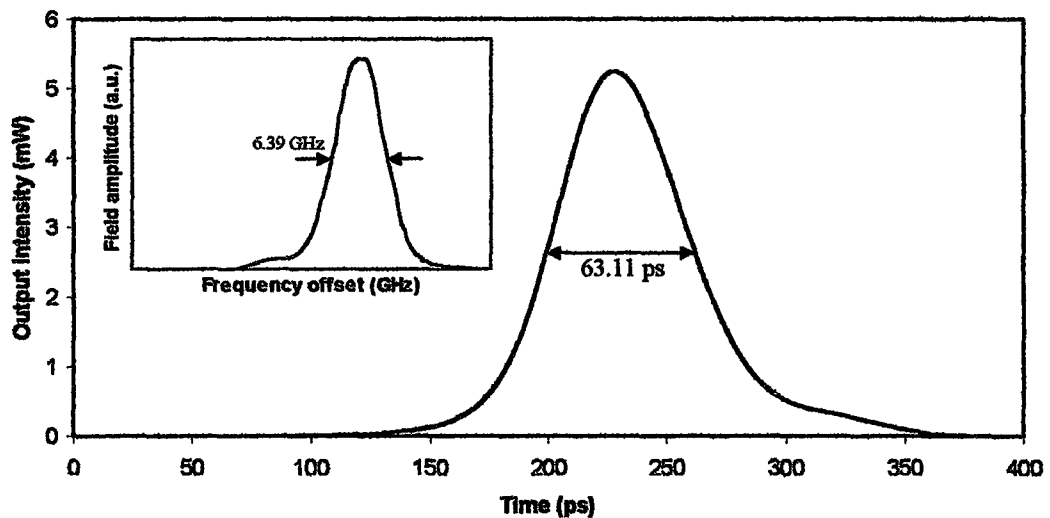


**Figure 5.10** Output intensity and field spectrum of mode-locked HSPS for Gaussian apodized FBG without noise at the mode-locking frequency of 2.1 GHz

A typical transform-limited output pulse with spontaneous noise that has a pulse width of 77 ps, spectral width of 5.74 GHz and a TBP of 0.442 at mode-locking frequency of 2.1 GHz is shown in Figure 5.11.

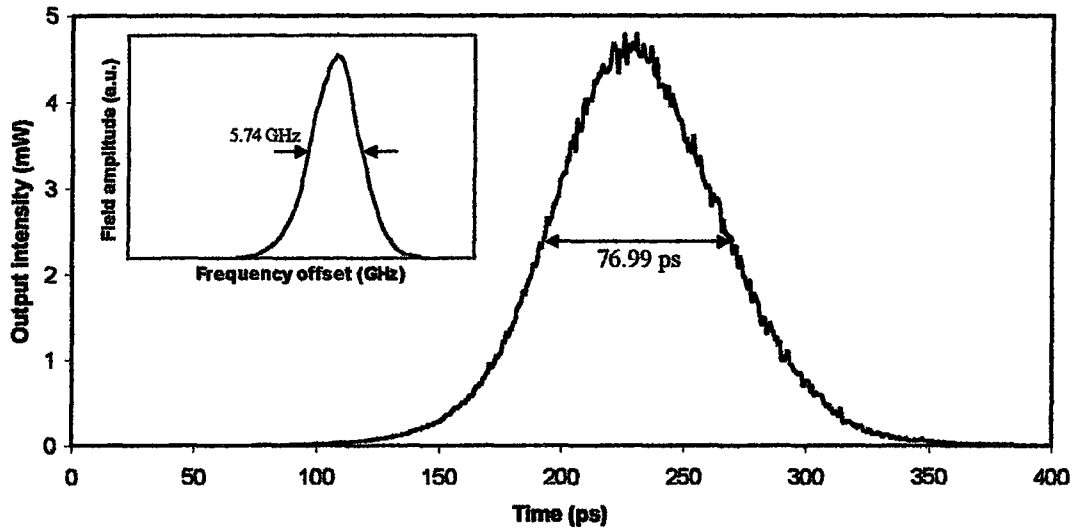


**Figure 5.11** Output intensity and field spectrum of mode-locked HSPS for Gaussian apodized FBG with spontaneous noise at the mode-locking frequency of 2.1 GHz

If only carrier noise is taken into account, transform-limited pulses are generated at the mode-locking frequencies of 2, 2.1, 2.2, 2.3 and 2.7 GHz. A typical output pulse that has pulse width of 62.12 ps, spectral width of 7.23 GHz and TBP of 0.449 at mode-locking frequency of 2.1 GHz is shown in Figure 5.12.

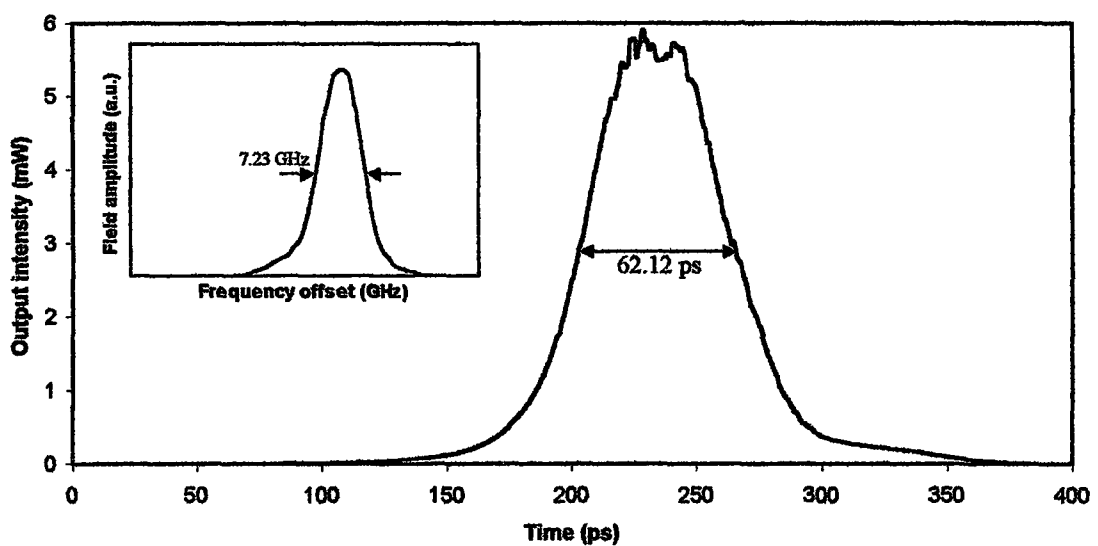


**Figure 5.12** Output intensity and field spectrum of mode-locked HSPS for Gaussian apodized FBG with carrier noise at the mode-locking frequency of 2.1 GHz

Transform-limited pulses are generated again at the mode-locking frequencies of 2.1, 2.2 and 2.3 GHz when spontaneous and carrier noises are added. Effect of these noises on HSPS at the mode-locking frequency of 2.1 GHz is given in Figure 5.13. As seen in figure pulsewidth is 73.76 ps, spectral width is 5.89 GHz and TBP is 0.435.

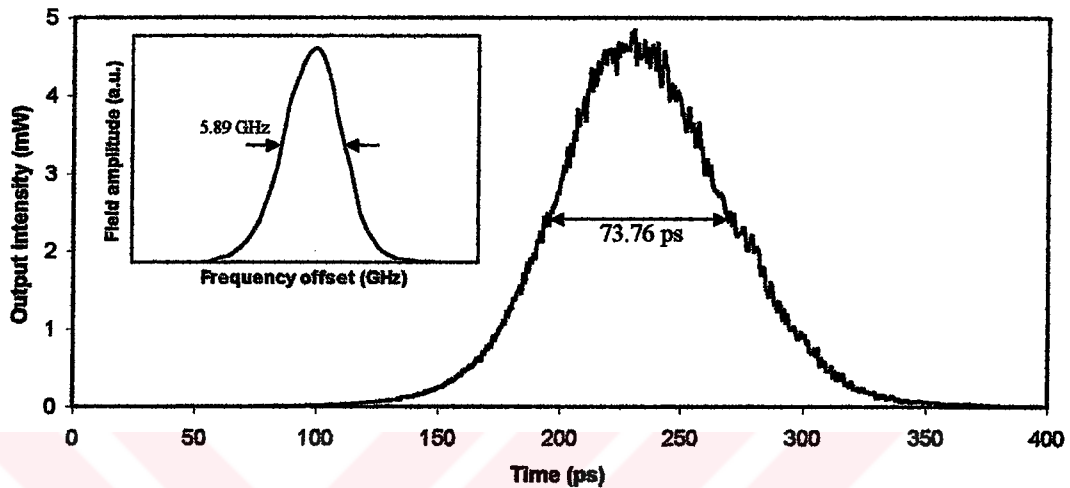


**Figure 5.13** Output intensity and field spectrum of mode-locked HSPS for Gaussian apodized FBG with spontaneous and carrier noise at the mode-locking frequency of 2.1 GHz

#### 5.4.4 Output of HSPS for Uniform FBG

The reflection spectrum of the uniform grating considered in this section is given in Figure 3.1. For this grating, mode-locked pulses that are not transform-limited are generated over a tuning range of 1 GHz (2-3 GHz) around the fundamental mode-locking frequency of 2.5 GHz without any noise. In this case, although TBP provides transform-limited pulse specifications giving a TBP of 0.494 and 0.524 at the mode-locking frequencies of 2.6 GHz and 2.7 GHz, pulsewidth is greater than 80 at the corresponding frequencies. An output pulse having a pulsewidth of 81.36 ps, spectral width of 6.074 GHz and TBP of 0.494 at the mode-locking frequency of 2.6 GHz is shown in Figure 5.14.

If spontaneous emission noise is considered, results show that transform-limited pulses are generated only at the mode-locking frequencies of 2.6 GHz and 2.7 GHz. A typical transform-limited output pulse that has a pulsewidth of 78.29 ps, spectral width of 4.73 GHz and TBP of 0.371 at the mode-locking frequency of 2.6 GHz is shown in Figure 5.15.

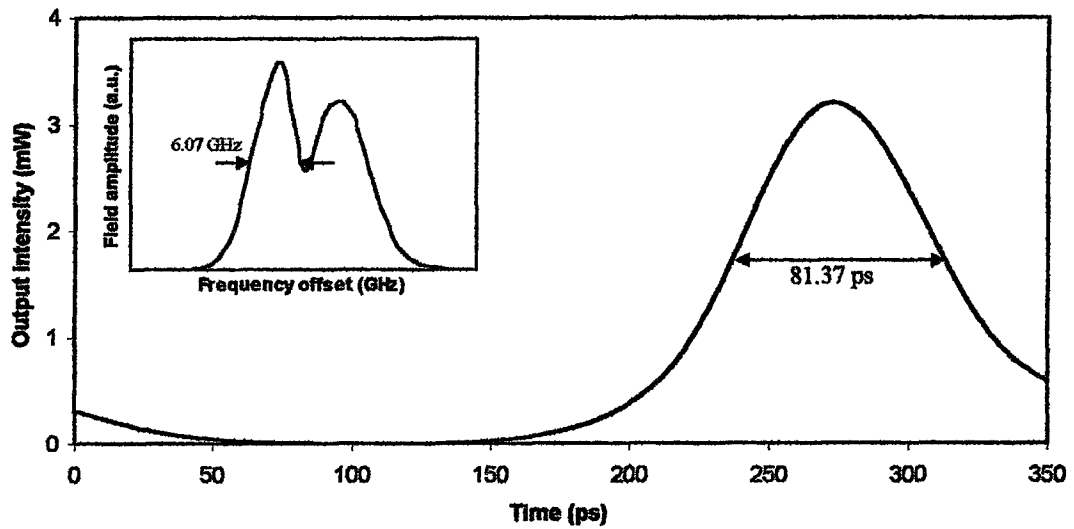


**Figure 5.14** Output intensity and field spectrum of mode-locked HSPS for uniform FBG without noise at the mode-locking frequency of 2.6 GHz

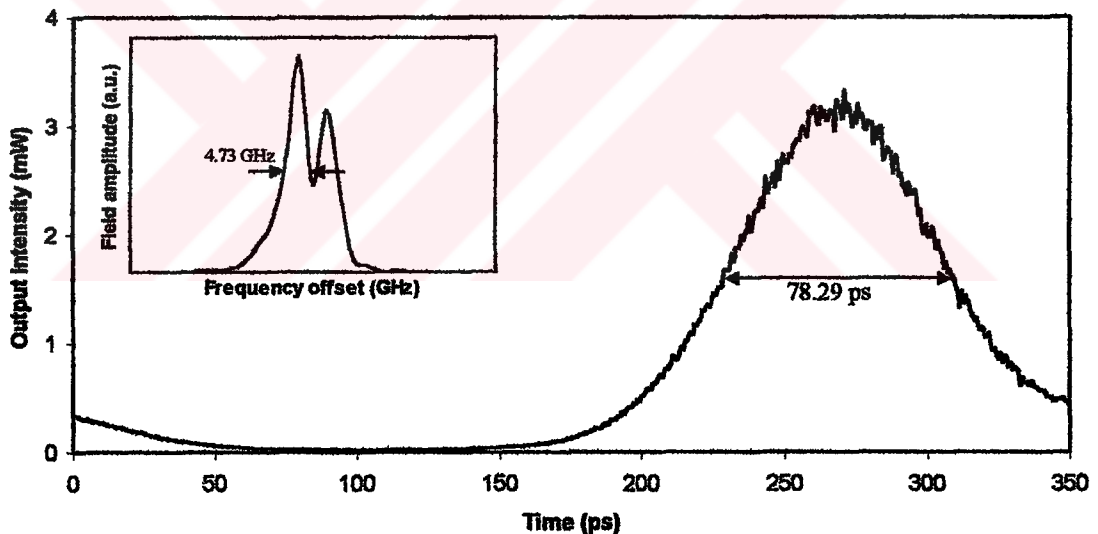


**Figure 5.15** Output intensity and field spectrum of mode-locked HSPS for uniform FBG with spontaneous noise at the mode-locking frequency of 2.6 GHz

Transform-limited pulses are obtained only at the mode-locking frequency of 2.7 GHz if carrier noise is considered. Output pulse having a pulse width of 60.39 ps, spectral width of 4.41 GHz and TBP of 0.266 at the mode-locking frequency of 2.7 GHz is given in Figure 5.16.

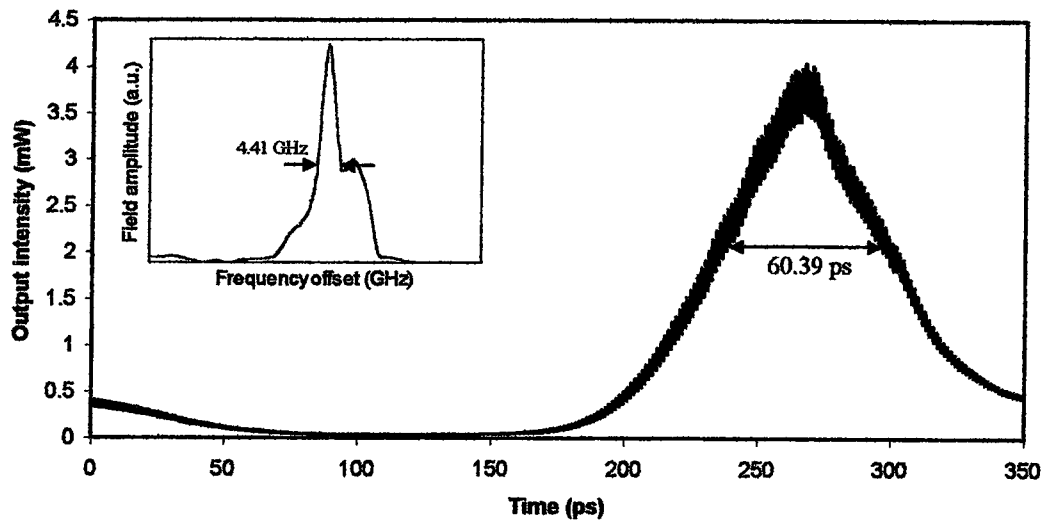


**Figure 5.16** Output intensity and field spectrum of mode-locked HSPS for uniform FBG with carrier noise at the mode-locking frequency of 2.7 GHz

HSPS including spontaneous and carrier noise produces output pulses that are transform-limited at the mode-locking frequencies of 2.6 and 2.7 GHz. For this case, output pulse that has a pulsewidth of 75.69 ps, spectral width of 4.99 GHz and TBP of 0.378 is given in Figure 5.17.

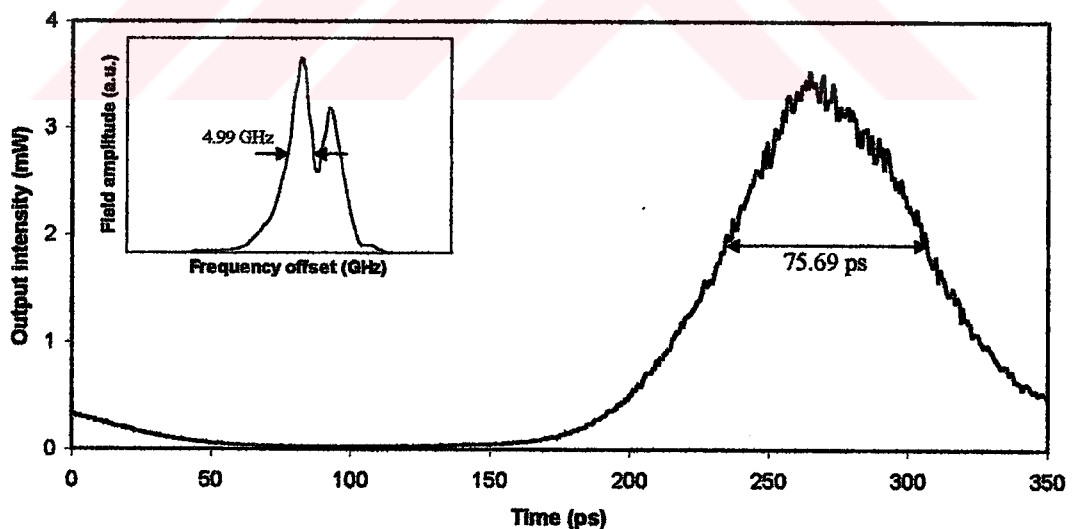


**Figure 5.17** Output intensity and field spectrum of mode-locked HSPS for uniform FBG with spontaneous and carrier noise at the mode-locking frequency of 2.6 GHz



## 5.5 Conclusions

In this section, effect of spontaneous and carrier noise on output of HSPS is explained. Output intensity and field spectrum that has been studied detail without noise in [23] is given at the mode-locking frequencies where transform-limited pulses are generated with and without noise.

From the obtained results, transform limited pulses over a wide tuning range around the fundamental mode-locking frequency are generated from the mode-locked HSPS with linearly chirped uniform and linearly chirped Gaussian apodized FBGs. The reason why transform limited pulses over a wide tuning range around the fundamental mode-locking frequency are not obtained from HSPS with unchirped gratings is that in a chirped Bragg reflector the distance within the reflector to an effective reflection plane depends on wavelength, giving a linear change in this distance as the wavelength is varied. Within the mode-locked cavity this translates into a change in overall cavity length, and therefore the mode-locking frequency, with a change in wavelength. In practice, for a particular modulation frequency the HSPS self-tunes its operating wavelength to keep the device on resonance, and therefore produce good mode-locking. By using a long chirped reflector large changes in modulation frequency can be accommodated. Linear chirp introduced into FBGs plays an important role for the generation of mode-locked transform-limited pulses over a wide tuning range around the fundamental mode-locking frequency from HSPS with these gratings.

As seen from the results, system operation is not affected by spontaneous noise. Carrier noise affects the output pulse of HSPS especially at the lower frequencies and at these frequencies transform-limited pulses are not generated. Both spontaneous and carrier noise may be effective at the fundamental mode-locking frequency of 2.5 GHz as seen in Figure 5.5. All of these results are obtained when standard laser diode parameters are used. However, if values of some laser diode parameters are changed, noise increases. Increasing noise affects the operation of device and therefore transform-limited pulses are not generated over a wide tuning range for linearly chirped uniform and linearly chirped Gaussian apodized FBGs. To better understand the effect of high noise on HSPS we should investigate the RIN spectrum for different values of these parameters that will be given in the next chapter.

## **CHAPTER 6**

### **RELATIVE INTENSITY NOISE (RIN) OF HSPS**

#### **6.1 Introduction**

In this chapter, RIN of HSPS for all types of FBGs will be described and the most effective noise terms will be determined through the results. In our simulation the cross correlation between the carrier and spontaneous noise is neglected because of the effect of this noise on RIN is very little.

#### **6.2 Relative Intensity Noise (RIN) of HSPS**

In this section, effect of spontaneous and carrier noise on RIN will be described for all type of FBGs for a wide frequency range of 1GHz around the fundamental frequency of 2.5 GHz.

##### **6.2.1 RIN of HSPS for Linearly Chirped Gaussian Apodized FBG**

Calculation of the RIN versus frequency is shown in Figure 6.1. As seen in the figure RIN has a peak at the fundamental mode-locking frequency of 2.5 GHz with spontaneous and both spontaneous and carrier noise and corresponding RIN values are  $-114.209$  dB and  $-102.903$  dB. Although transform-limited pulses are generated for  $-114.209$  dB of RIN value, it is not obtained for  $-102.903$  dB of RIN value as explained section 5.3.1. At the other mode-locking frequencies transform-limited pulses are generated.

Carrier noise is more effective at the mode-locking frequency of 2.3 GHz and it gives a RIN value of  $-96.96$  dB as shown in Figure 6.1. At this frequency output pulse that has a pulsewidth of 0.852 ps, a spectral width of 8.068 GHz and a TBP of 0.007. Hence pulse is not transform limited. At the fundamental mode-locking frequency RIN is low as seen in figure and pulse is transform limited. With carrier noise,

transform limited pulses is not generated only at the mode-locking frequencies of 2.3 and 2.1 GHz.

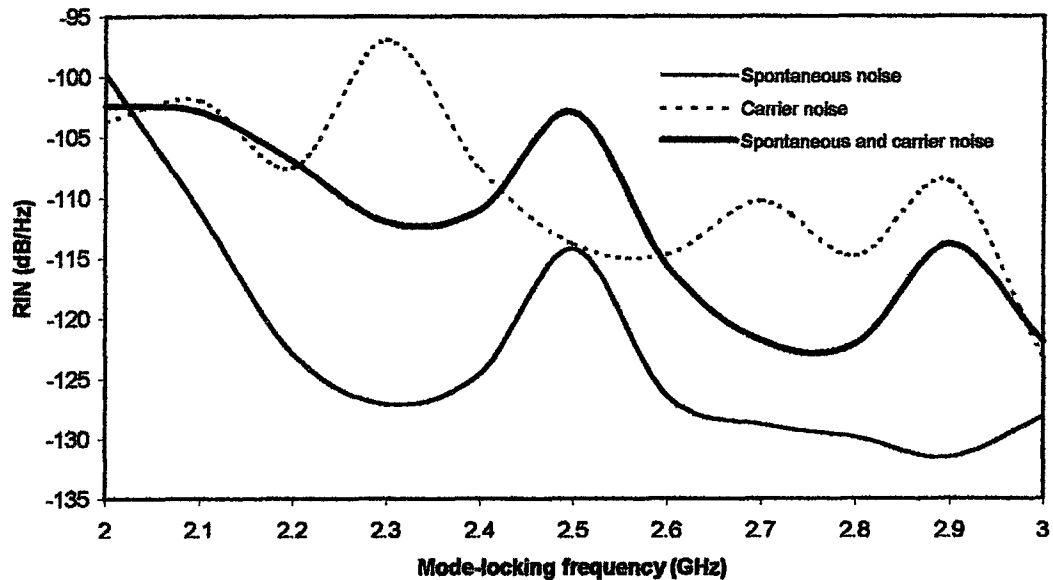
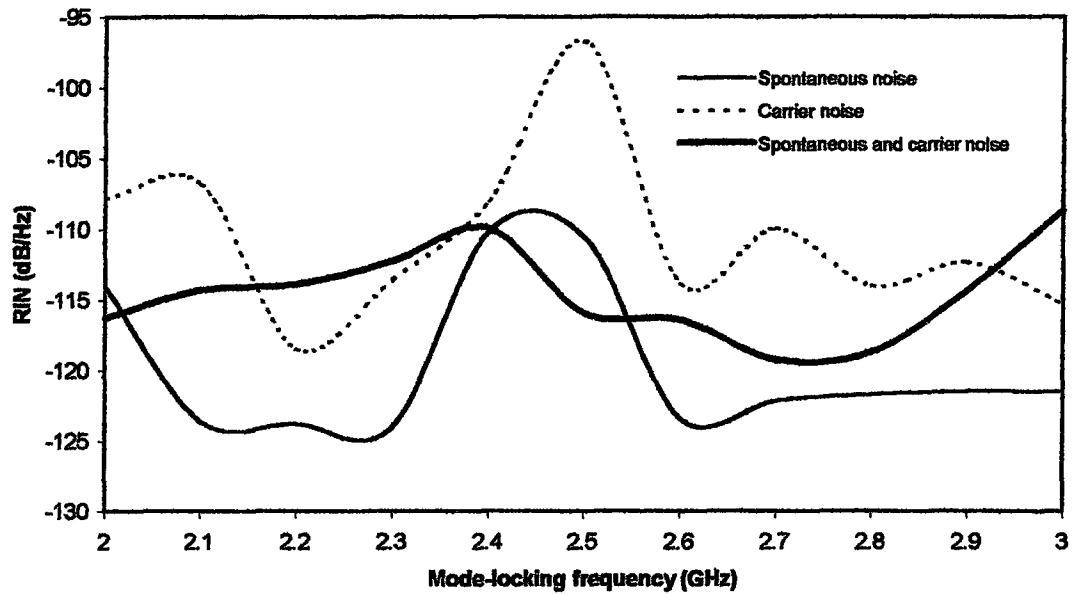


Figure 6.1 RIN spectrums of HSPS for linearly chirped Gaussian apodized FBG

### 6.2.2 RIN of HSPS for Linearly Chirped Uniform FBG

Effect of noise on RIN spectrum is given Figure 6.2. As seen in figure, with spontaneous noise RIN values is high and remains approximately the same at the mode-locking frequencies of 2.4 and 2.5 GHz, fact that the top of the spectrum is a little broad. This is the result of the long spatial extent of the Bragg reflector, which provides feedback at a range of effective cavity lengths. It is this phenomenon that allows an extremely large mode-locking frequency range for this kind of device as explained before. RIN values at the corresponding mode-locking frequencies are -110.184 dB and -110.521 dB. Explained section 5.3.2 for these gratings transform limited pulses are generated over a wide tuning range.

Carrier noise affects the RIN spectrum especially at the fundamental mode-locking frequency as seen in Figure 6.2 and it gives a RIN value of -96.738 dB. At this frequency pulse is not transform limited. At the mode-locking frequency of 2.4 GHz RIN is low and pulse is transform limited. Pulse is also not transform-limited at the mode-locking frequency of 2 GHz giving a TBP 0.577.



**Figure 6.2** RIN spectrums of HSPS for linearly chirped uniform FBG

If both of noises are included, RIN has a peak at the mode-locking frequency of 2.4 GHz and its value is  $-109.938$  dB as seen in figure. In this case, pulsewidth is 38.389 ps; spectral width is 8.132 GHz giving a TBP of 0.312 at this mode-locking frequency. These results are proper for practical applications. Near transform limited pulses are again generated over a wide frequency range of 2-3.1 GHz.

### 6.2.3 RIN of HSPS for Gaussian Apodized FBG

RIN spectrum of HSPS for Gaussian apodized FBG is given in Figure 6.3. As shown in figure there is no noise peak at the fundamental frequency where transform-limited pulses are not generated. It is found that for this gratings produced transform-limited pulses are not related to magnitude of RIN. Because transform-limited pulses are obtained at the mode-locking frequencies of 2.1, 2.2 and 2.3 GHz with spontaneous noise and corresponding RIN values are  $-107.45$  dB,  $-113.02$  dB, and  $-119.28$  dB as seen in figure. However, RIN values are lower than these RIN values at the mode-locking frequency ranges of 2.4-2.9 GHz that transform-limited pulses are not produced.

With carrier noise transform-limited pulses are obtained at the mode-locking frequencies of 2, 2.1, 2.2, 2.3 and 2.7 GHz and it gives RIN values of  $-102.363$  dB, -

112.135 dB, -104.447 dB, -118.011 dB, and -115.931 dB at these frequencies. It is noticeable that RIN is low at the mode-locking frequency of 2.4 to 3 GHz.

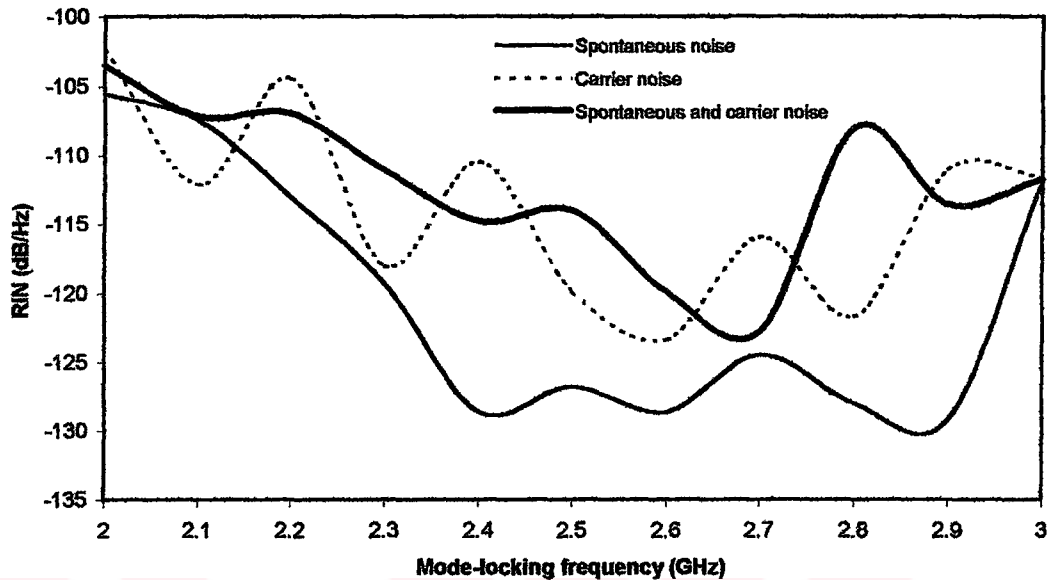
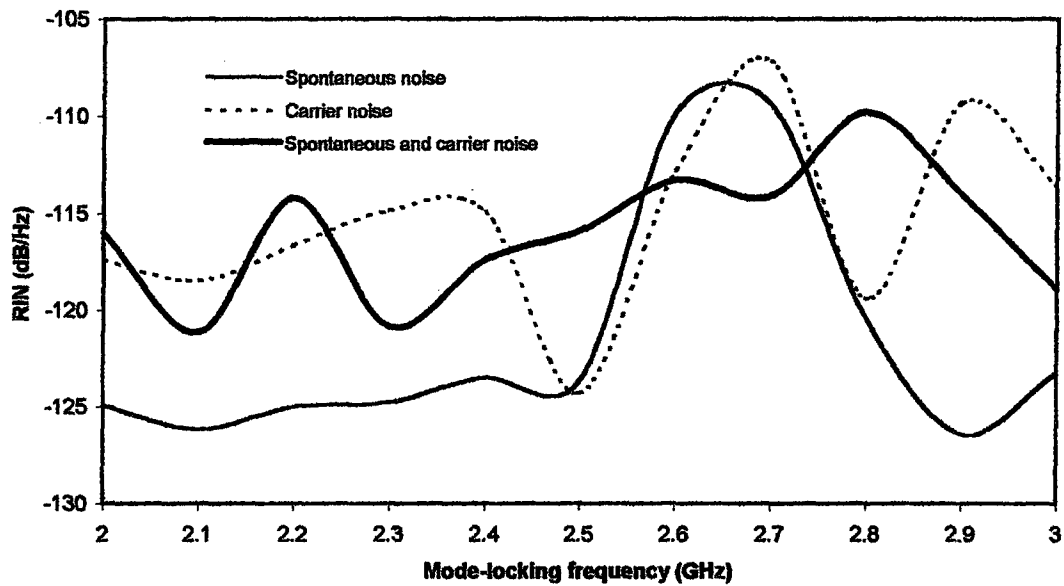


Figure 6.3 RIN spectrums of HSPS for Gaussian apodized FBG

If both noises are considered, transform-limited pulses are only produced at the mode-locking frequencies of 2.1, 2.2 and 2.3 GHz although RIN is low at the mode-locking frequency range of 2.4 to 2.7 GHz as seen in figure.

#### 6.2.4 RIN of HSPS for Uniform FBG

Figure 6.4 shows the RIN spectrum of HSPS utilizing uniform FBG. For this case, again produced transform-limited pulses are not related to magnitude of RIN. Although RIN spectrum has a peak at the mode-locking frequency of 2.7 GHz with carrier noise giving a RIN value of  $-109.4$  dB, transform-limited pulses are obtained only at this frequency. Also, when spontaneous noise is included, transform-limited pulses are produced only at the mode-locking frequencies of 2.6 and 2.7 GHz giving approximately a RIN value of  $-109$  dB and as seen in figure this value is high compared to other mode-locking frequencies. If both of noise is considered, in this case, transform-limited pulses are generated only at the mode-locking frequencies of 2.6 and 2.7 GHz.



**Figure 6.4 RIN spectrums of HSPS for uniform FBG**

The conclusion got to from the results is that if HSPS is properly mode-locked over a wide frequency range that transform-limited pulses are produced around the fundamental frequency of 2.5 GHz, noise peak occurs at the fundamental mode-locking frequency as seen in the results of linearly chirped uniform and linearly chirped Gaussian apodized FBGs. For Gaussian apodized and uniform FBGs transform-limited pulses are not generated at the fundamental mode-locking frequency and these pulses are obtained only at the limited frequency range and so there is no noise peak at the fundamental mode-locking frequency.

Active mode-locking is a resonance-like phenomenon in which the laser is modulated at a frequency corresponding to the inverse roundtrip propagation time of the laser cavity. That is the reason why the RIN spectrum has a noise peak at the resonance frequency that shows optical resonance due to cavity roundtrip time. Except at this frequency, pulsewidth is not affected by the noise in the locking range. It is also found that, in this study, noise affects output pulse at the mode-locking frequencies of 2.4 and 2.5 GHz for linearly chirped uniform FBGs as seen in Figure 6.2.

### 6.3 Effects of RF and DC Currents on RIN of HSPS

In this section, effects of RF and DC currents on RIN characteristics of HSPS with all types of FBGs including spontaneous and carrier noise will be presented. For this purpose, the ranges are taken as 2-3 GHz for the frequency, 10-30 mA with 5 mA steps and 4-8 mA with 1 mA steps for the RF and DC currents, respectively.

#### 6.3.1 Effects of RF and DC Currents on RIN of HSPS Utilizing Linearly Chirped Gaussian Apodized FBG

In order to investigate the effects of the level of the RF current, the laser diode is biased at a constant DC bias of 6 mA. The magnitude of the RF current is changed between 10 and 30 mA with 5 mA steps.

If RF current increases, noise peak shifts from 2.5 GHz to 2.4 GHz as shown in Figure 6.5 with spontaneous noise. As seen in the figure RIN has a peak at the mode-locking frequency of 2.5 GHz for RF current of 10 mA and at the mode-locking frequency of 2.4 GHz for 30 mA and at these frequencies transform limited pulses are not obtained. These pulses are also not generated at 2 and 2.1 GHz for 10 mA and at 2 GHz for 15 mA. Mode-locked of HSPS are not more affected by noise for the other current values and therefore transform-limited pulses are obtained over a wide frequency range.

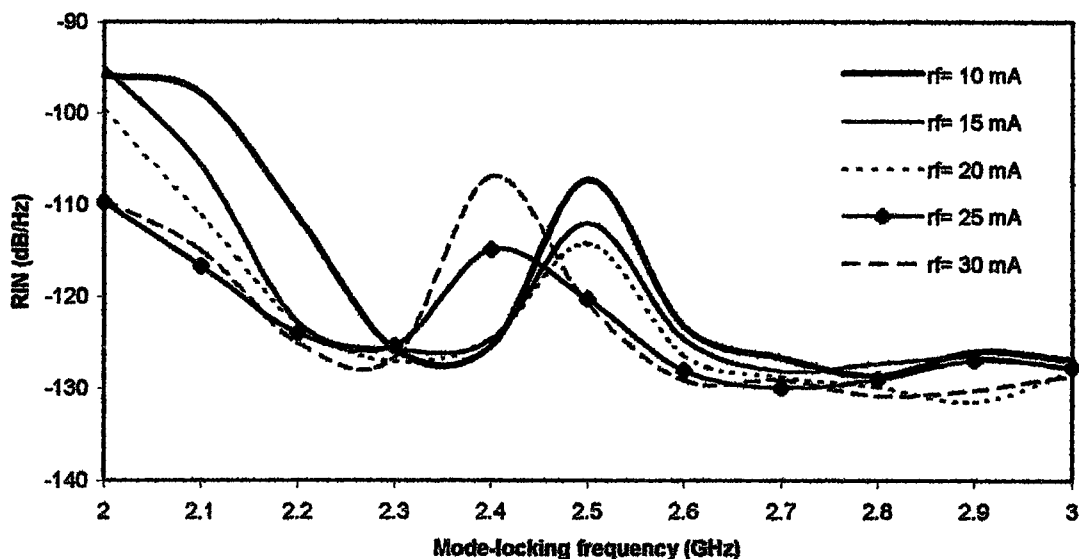


Figure 6.5 RIN spectrums of HSPS for linearly chirped Gaussian apodized FBG including spontaneous noise with different RF current for a DC current of 6 mA

Figure 6.6 shows effect of RF current on RIN if both of noise is taken into account. In this case, transform limited pulses are not generated at the mode-locking frequencies of at 2 and 2.1 GHz for 10 mA, at 2 and 2.5 GHz for 15 mA, and at 2.4 and 2.5 GHz for 30 mA.

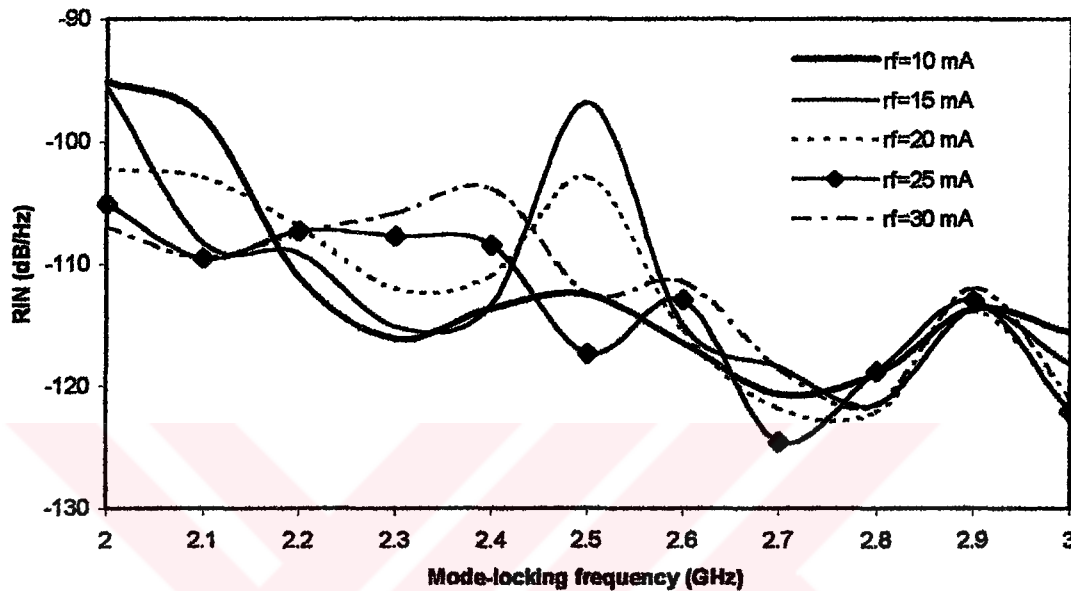


Figure 6.6 RIN spectrums of HSPS for linearly chirped Gaussian apodized FBG including spontaneous and carrier noise with different RF current for a DC current of 6 mA

Dr. YÜKSEL ÖZGÜR  
YÜKSEL ÖZGÜR

Figure 6.7 shows the effects of the DC current on the RIN when the laser diode is driven with 20 mA of RF current at the fundamental mode-locking frequency of 2.5 GHz. As seen in the figure for 5 mA of DC current top of the RIN spectrum is little broad because RIN is high and remains approximately the same at the mode-locking frequencies of 2.4 and 2.5 GHz. At these frequencies transform limited pulses are not obtained. These pulses are also not obtained at 2.5 GHz for a current of 4 and 7 mA and 2 GHz for 8 mA although obtained all mode-locking frequencies for 6 mA.

If both of noise is considered, 5 mA and 6 mA of DC current is the best value for mode-locked HSPS because of giving a 900 MHz mode-locking range where transform limited pulses are generated as seen in Figure 6.8.



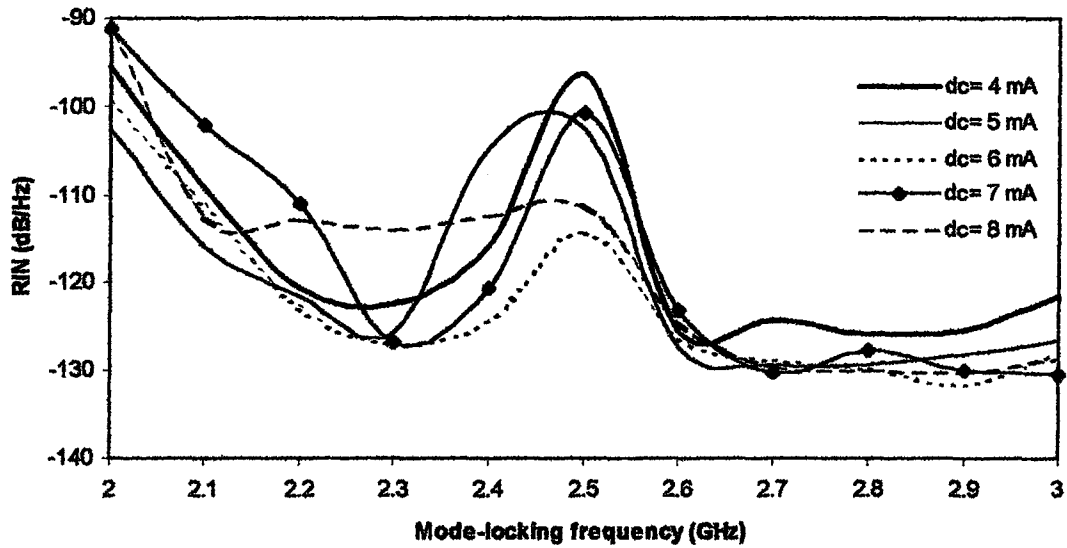


**Figure 6.7** RIN spectrums of HSPS for linearly chirped Gaussian apodized FBG including spontaneous noise with different DC current for a RF current of 20

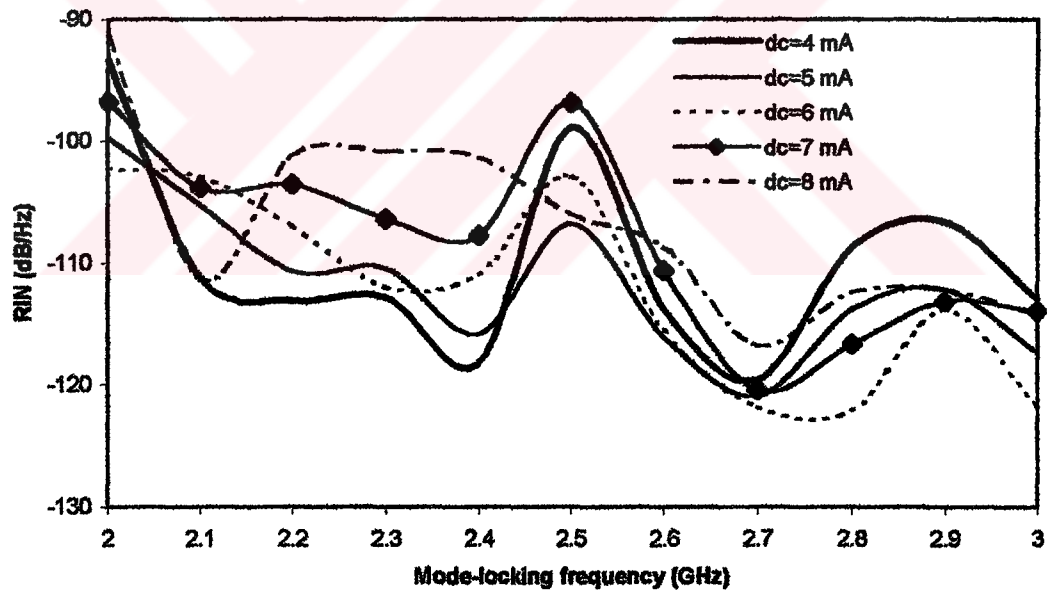


**Figure 6.8** RIN spectrums of HSPS for linearly chirped Gaussian apodized FBG including spontaneous and carrier noise with different DC current for a RF current of 20 mA

These results show that optimal value of RF current changes between 20 and 25 mA with spontaneous noise and both spontaneous and carrier noise. Optimal DC current is 6 mA with spontaneous noise and 5 and 6 mA for both spontaneous and carrier noise for mode-locked HSPS utilizing linearly chirped Gaussian apodized FBG.

DC YÖKSEKAKADEMİK KURULU  
 DOKÜMANIYASI VE ARŞİVİ

### 6.3.2 Effects of RF and DC Currents on RIN of HSPS Utilizing Linearly Chirped Uniform FBG

Figure 6.9 gives the effects of the RF current on the RIN for linearly chirped uniform FBG with spontaneous noise. In this case, transform limited pulses are generated over a wide frequency range (2-3.1 GHz) for all of currents except the 10 mA. For 10 mA transform limited pulses are not obtained at the mode-locking frequency of 2.4 GHz.

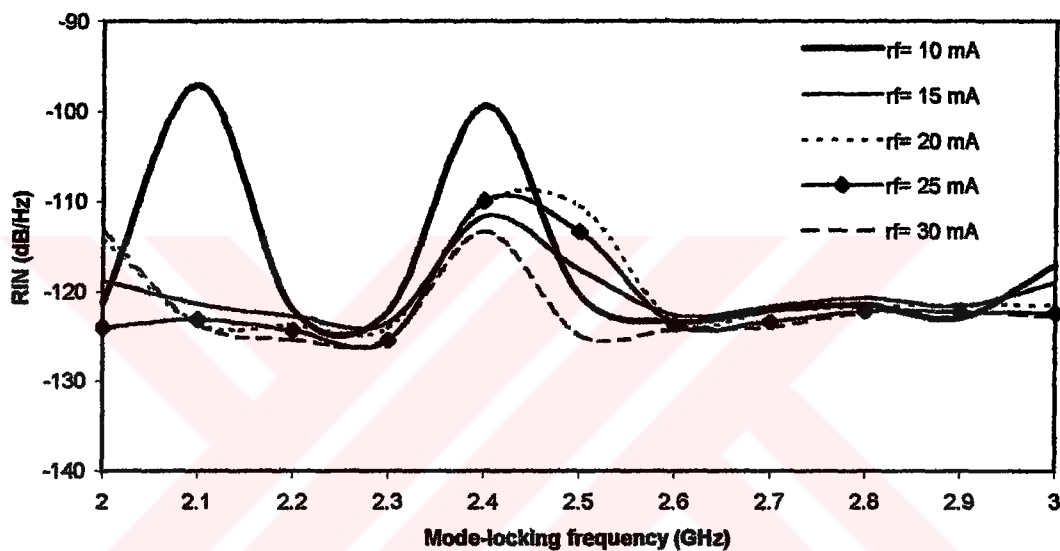
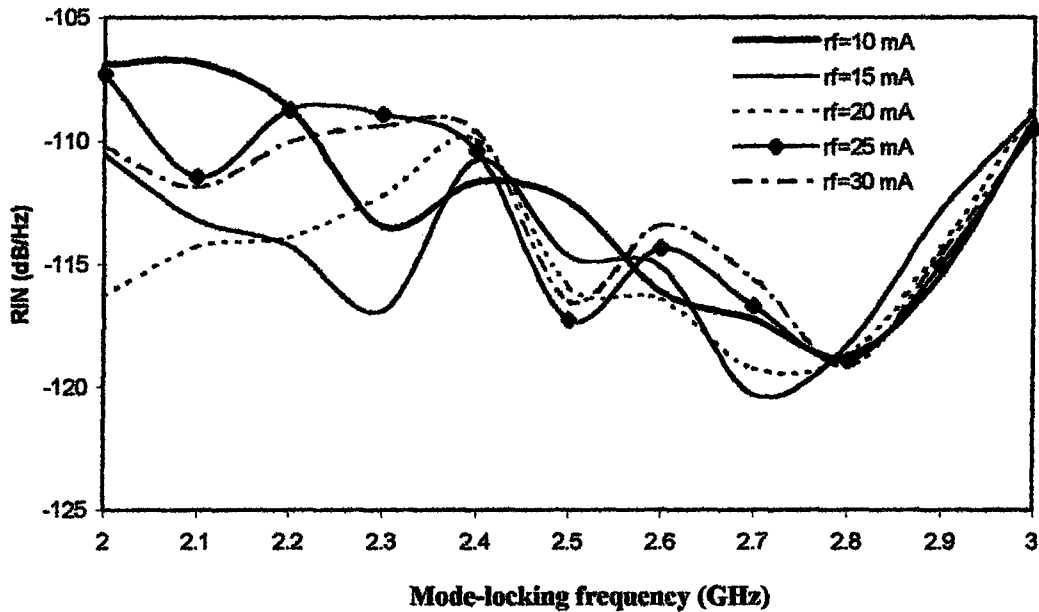


Figure 6.9 RIN spectrums of HSPS for linearly chirped uniform FBG including spontaneous noise with different RF current for a DC current of 6 mA

Transform-limited pulses are generated over a wider frequency range for all of current values if both of noise is considered as seen in Figure 6.10.

The effect of the DC current on the RIN is shown in Figure 6.11. As seen in figure RIN has a high value at the mode-locking frequency of 2.5 GHz for 4 mA of DC current and transform limited pulses are not obtained at this frequency. These pulses are also not generated at the mode-locking frequency of 2 GHz for 7 and 8 mA. Except at these frequencies and for the other currents transform limited pulses are generated.



**Figure 6.10** RIN spectrums of HSPS for linearly chirped uniform FBG including spontaneous and carrier noise with different RF current for a DC current of 6 mA

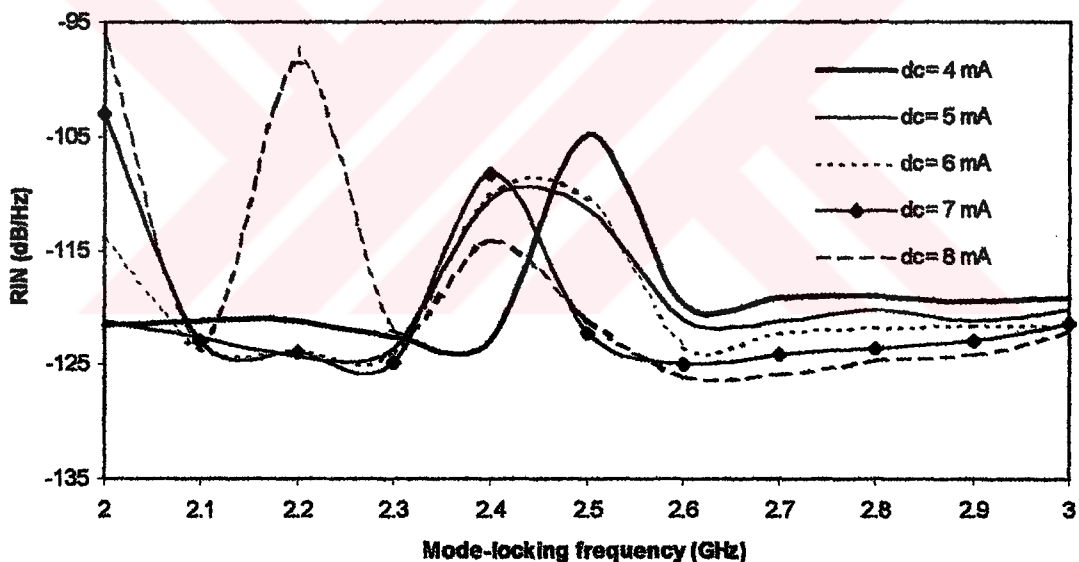


**Figure 6.11** RIN spectrums of HSPS for linearly chirped uniform FBG including spontaneous noise with different DC current for a RF current of 20 mA

The effect of DC current on the RIN spectrum is given in Figure 6.12 if both of noise is considered. For this case, transform-limited pulses are generated over a wider frequency range for all of DC current values except the mode-locking frequency of 2.4 GHz for 8 mA.

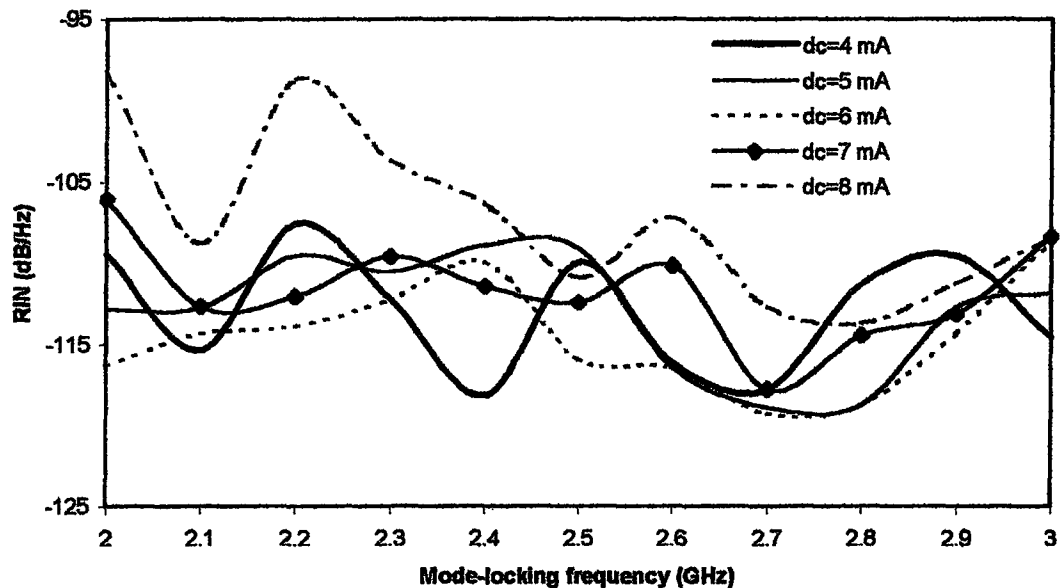


**Figure 6.12** RIN spectrums of HSPS for linearly chirped uniform FBG including spontaneous and carrier noise with different DC current for a RF current of 20 mA

From the obtained results, optimal values of RF currents are all currents except the 10 mA with spontaneous noise and all currents with both spontaneous and carrier noise. Optimal DC currents are 5-6 mA with spontaneous noise and all currents except the 8 mA with both of noise.

### **6.3.3 Effects of RF and DC Currents on RIN of HSPS Utilizing Gaussian Apodized FBG**

The effects of the RF current on the RIN for Gaussian apodized FBG including spontaneous noise is given in Figure 6.13. As seen in figure RIN is very low between the mode-locking frequencies of 2.4 and 3 GHz. Transform limited pulses are obtained only at 2.4 GHz for 10 mA of RF current, at 2.2 and 2.3 GHz for 15 mA, at 2.1, 2.2 and 2.3 GHz for 20 mA, at 2, 2.1, 2.2, 2.3 and 2.6 GHz for 25 mA, and at 2.1, 2.2, 2.3, 2.6 and 2.7 GHz for 30 mA. As seen the results transform limited range increases if RF current increases.

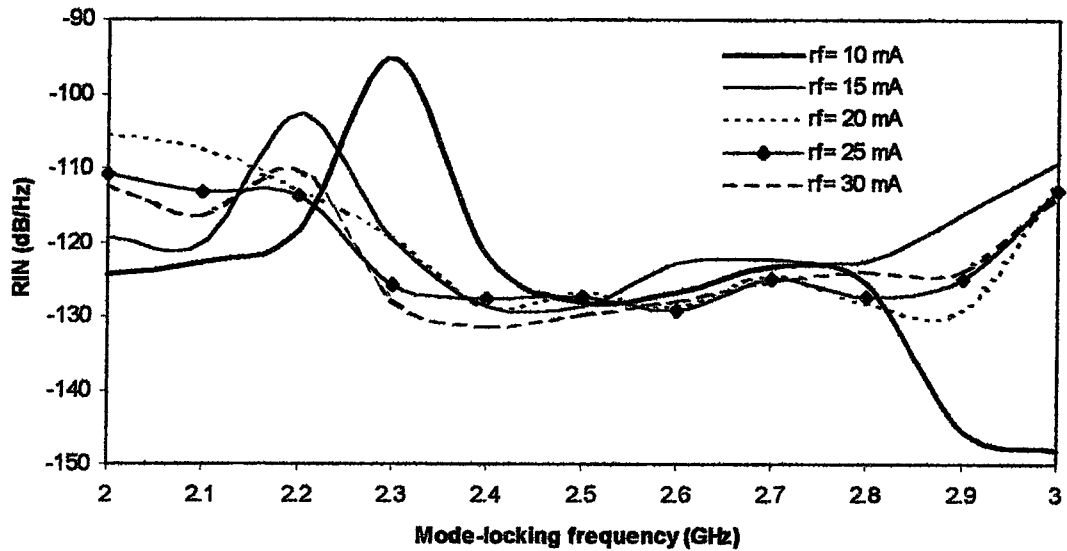


Figure 6.13 RIN spectrums of HSPS for Gaussian apodized FBG including spontaneous noise with different RF current for a DC current of 6 mA

Figure 6.14 shows effect of RF current on RIN if both of noise is considered. In this case, obtained results are similar to previous results and transform limited pulses are generated frequency range of 500 MHz for 25 and 30 mA. However, the other current values this range changes between 100 and 300 MHz.

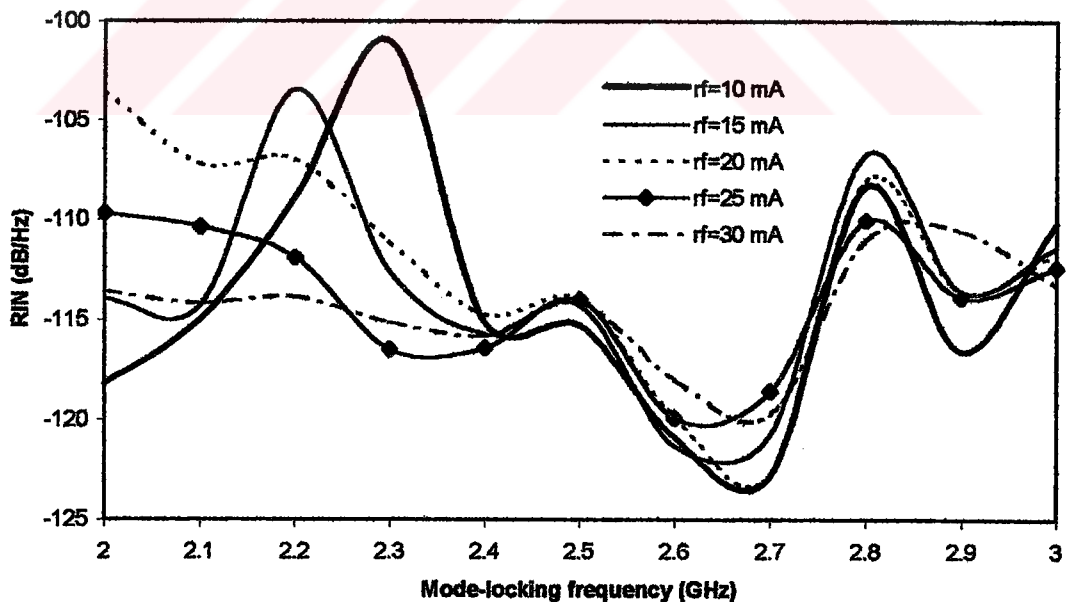


Figure 6.14 RIN spectrums of HSPS for Gaussian apodized FBG including spontaneous and carrier noise with different RF current for a DC current of 6 mA with

Although RIN is low wide frequency range for different DC current as shown in Figure 6.15, for only some mode-locking frequencies transform limited pulses are

generated as in RF current effects with spontaneous noise. These frequencies are 2.2 and 2.3 GHz for 4 mA, 2.1, 2.2 and 2.3 GHz for 5 mA and 6 mA, 2.1, 2.2, 2.3 and 2.6 GHz for 7 mA, 2.2, 2.3, and 2.6 GHz for 8 mA.

If both of noise is taken into account, transform limited pulses are generated from 200 MHz to 400 MHz for all of DC currents although RIN has a low value for many mode-locking frequencies as seen in Figure 6.16.

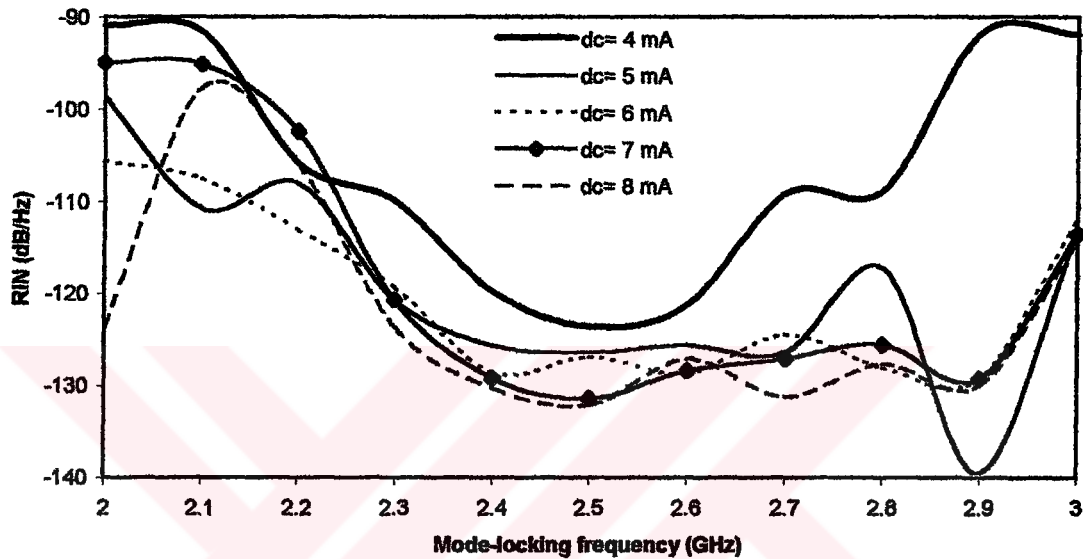


Figure 6.15 RIN spectrums of HSPS for Gaussian apodized FBG including spontaneous noise with different DC current for a RF current of 20 mA

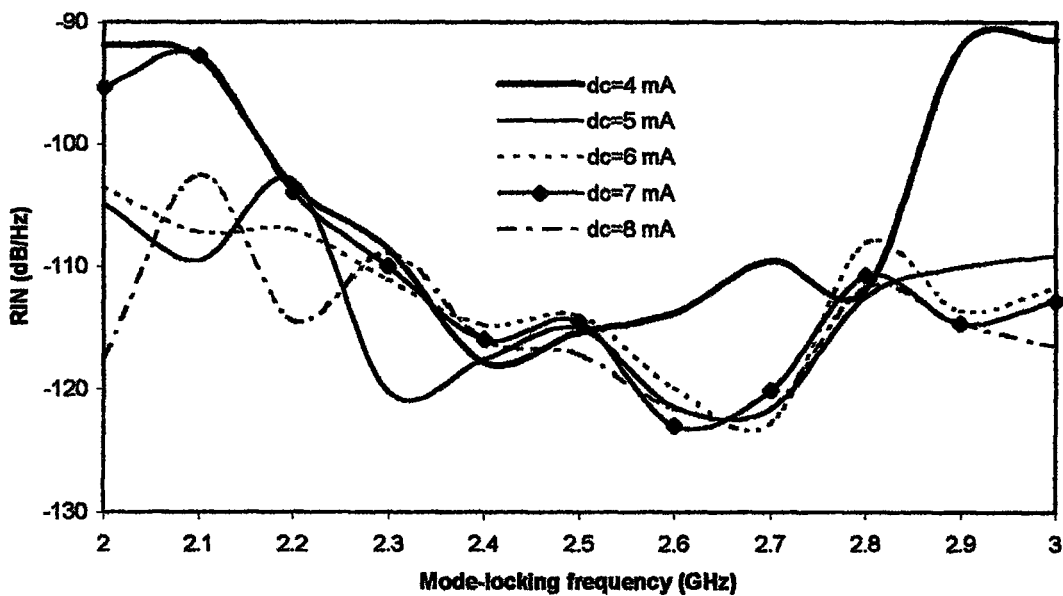


Figure 6.16 RIN spectrums of HSPS for Gaussian apodized FBG including spontaneous and carrier noise with different DC current for a RF current of 20 mA

For all of these results show that the generated transform limited pulses for Gaussian apodized FBG is not directly related to RIN value as explained before section 6.2.3. Although as seen in Figures 6.13-16 RIN is low many mode-locking frequencies, transform limited pulses are generated only limited frequency range. This result is not valid for linearly chirped Gaussian apodized and linearly chirped uniform FBGs.

From the obtained results, optimal values of RF currents are taken 25-30 mA with spontaneous noise and with both spontaneous and carrier noise. Optimal value of DC current is 7 mA with spontaneous noise and 8 mA with both of noises.

#### 6.3.4 Effects of RF and DC Currents on RIN of HSPS Utilizing Uniform FBG

As shown in Figure 6.17 the effect of the RF current on the RIN for uniform FBG including spontaneous noise is very small for 10 mA and for this current TBP value is in the range of transform-limited pulse specifications at the mode-locking frequencies of 2, 2.1, 2.2, 2.7, 2.8, 2.9 and 3 GHz. However, more of these frequencies pulsewidth takes a value greater than 80 ps. Transform-limited pulses are obtained at 2.9 and 3 GHz for 15 mA, at 2.6 and 2.7 GHz for 20 mA, at 2.6, 2.7 and 2.8 GHz for 25 mA, and at 2.7, 2.8 and 3 GHz for 30 mA.

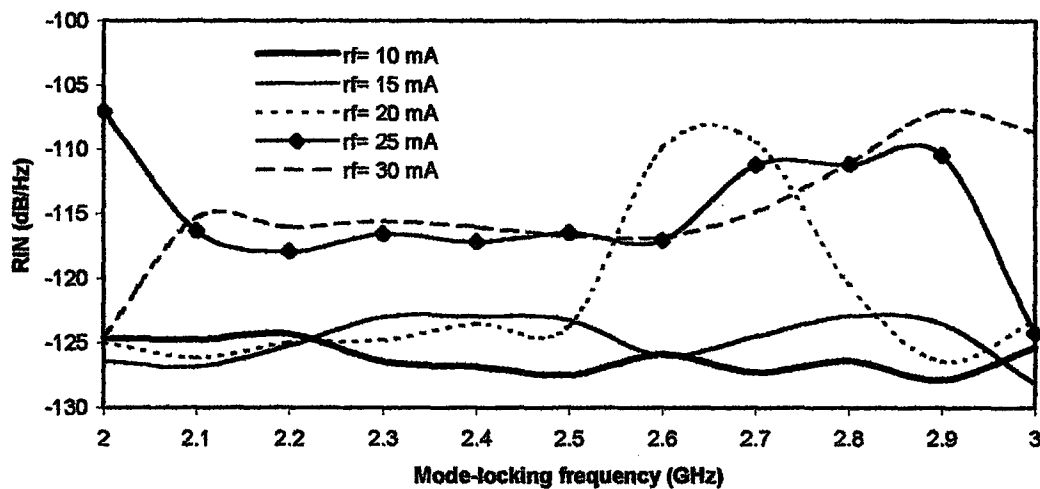


Figure 6.17 RIN spectrums of HSPS for uniform FBG including spontaneous noise with different RF current for a DC current of 6 mA

Figure 6.18 shows effect of RF current on the RIN when HSPS includes spontaneous and carrier noise. In this case, again transform-limited pulses are obtained again only limited frequency range.

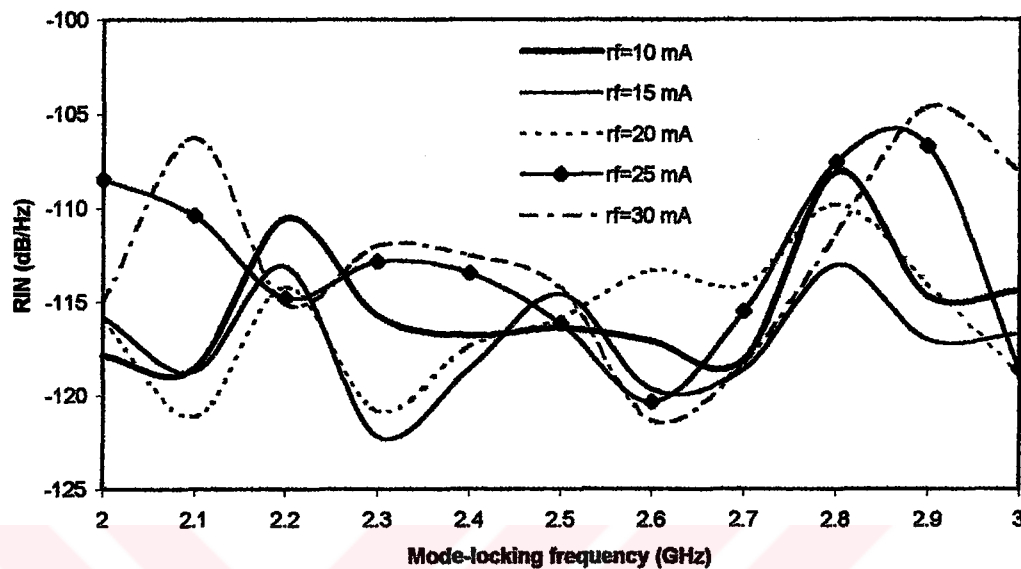


Figure 6.18 RIN spectrums of HSPS for uniform FBG including spontaneous and carrier noise with different RF current for a DC current of 6 mA

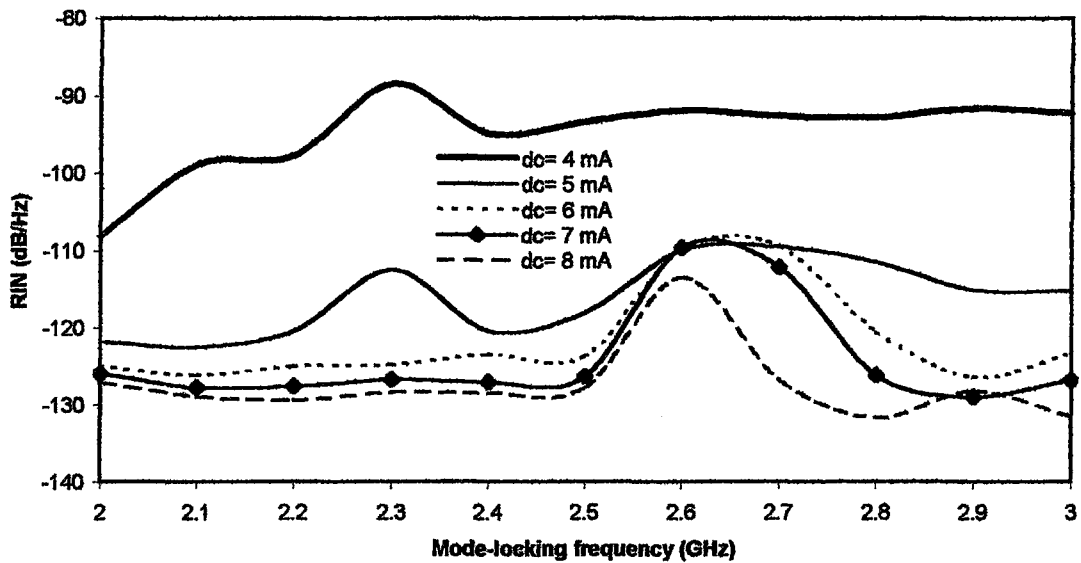
For 4 mA of the DC current RIN is very high as shown in Figure 6.19. Over all frequency range transform limited pulses are not generated for 4 and 8 mA. As seen in figure the other current values RIN is low and transform limited pulses are obtained at 2.6, 2.7 and 2.8 for 5 mA, at 2.6 GHz for 6 mA, at 2.7 GHz for 7 mA.

Figure 6.20 shows effect of DC current on the RIN if both of noise is considered. As seen in Figures 6.19 and 6.20 RIN spectrums are very similar to each other and transform-limited pulses are generated again maximum frequency range of 300 MHz.

These results also show that transform limited pulses for uniform FBG is not directly related to RIN value as in Gaussian apodized FBG as explained before section 6.2.4.

From the obtained results, optimal values of RF and DC currents are taken 10 mA and 5 mA with spontaneous noise and both spontaneous and carrier noise.





**Figure 6.19** RIN spectrums of HSPS for uniform FBG including spontaneous noise with different DC current for a RF current of 20 mA

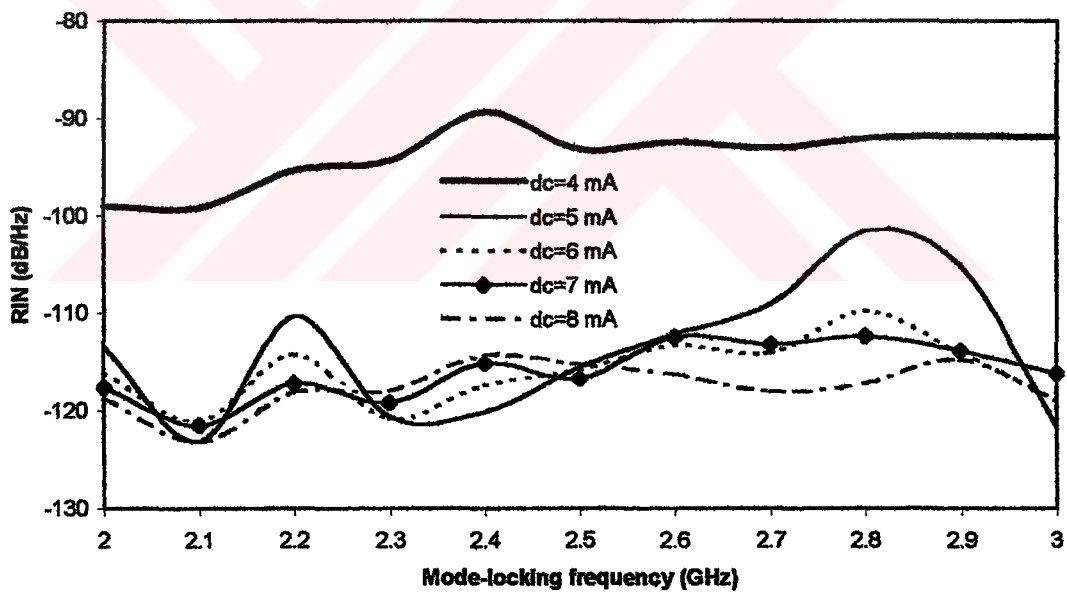


**Figure 6.20** RIN spectrums of HSPS for uniform FBG including spontaneous and carrier noise with different DC current for a RF current of 20 mA

All of these results show that output pulse and RIN of HSPS are very sensitive to the bias currents and so suitable value of these currents should be used to obtain transform-limited pulses for a large frequency range and low RIN value.

## 6.4 The Important Noise Parameters

In this section we will try to determine the most effective noise parameters through the results. Simulations are made for all type of FBGs when HSPS includes spontaneous and both spontaneous and carrier noise.

### 6.4.1 Linewidth Enhancement Factor

Linewidth enhancement factor ( $\alpha_h$ ) determines spectral linewidth and frequency chirp. MQW lasers have  $\alpha_h$  parameters that are about half those of similar lasers with bulk active layers and it is generally taken 2 for these lasers. For a semiconductor laser the refractive index depends on the carrier density and  $\alpha_h$  determines this dependence. Although zero dependence is impossible to obtain in practice, in our simulation  $\alpha_h$  is varied 0 to 5. The following results show the importance of this parameter.

Table 6.1 and 6.2 shows the variation in pulsewidth, spectral width and TBP for linearly chirped Gaussian apodized and linearly chirped uniform gratings due to  $\alpha_h$  at the mode-locking frequency of 2.5 GHz.

**Table 6.1** Effects of varying  $\alpha_h$  for linearly chirped Gaussian apodized FBG

$\alpha_h$	Pulsewidth (ps)	Spectral width (GHz)	TBP
0	60.19/60.17*/59.18**	9.42/9.38*/9.41**	0.567/0.564*/0.557**
2	45.38/40.55*/1.278**	8.68/8.60*/8.80**	0.394/0.349*/0.011**
5	31.87/41.77*/30.58**	10.98/8.16*/11.26**	0.350/0.341*/0.344**

**Table 6.2** Effects of varying  $\alpha_h$  for linearly chirped uniform FBG

$\alpha_h$	Pulsewidth (ps)	Spectral width (GHz)	TBP
0	58.00/58.61*/58.00**	9.28/9.26*/9.30**	0.539/0.543*/0.540**
2	45.69/34.23*/37.66**	8.73/9.07*/9.03**	0.399/0.310*/0.340**
5	27.73/31.47*/12.04**	11.12/9.30*/10.19**	0.308/0.293*/0.123**

\* with spontaneous noise, \*\* with both spontaneous and carrier noise

The reduction in pulsewidths when  $\alpha_h$  is changed between 0 and 5 is very noticeable, with and without noise for linearly chirped Gaussian apodized and linearly chirped uniform FBGs. However, spectral width increases a little with  $\alpha_h$ , possibly due to wavelength chirping. TBP decreases with increasing  $\alpha_h$  with and without noise.

The effect of this parameter on the RIN is given Figure 6.21 and 6.22 for linearly chirped Gaussian apodized FBG. As seen in figure when  $\alpha_h$  increases, noise increases and for a large amount mode-locking frequencies transform-limited pulses are not generated. Hence, proper mode-locking range reduces. RIN is low for its zero value except the mode-locking frequency of 2 GHz but in this case TBP is greater than 0.5 that is not in the range of transform-limited pulse specifications at the mode-locking frequency of 2.1 and 2.5 GHz without noise, at the mode-locking frequency of 2.5 GHz with spontaneous noise and at the mode-locking frequencies of 2.4 and 2.5 GHz with both spontaneous and carrier noise.

As seen in Figure 6.22 RIN is high at the mode-locking frequency of 2 GHz for zero value of  $\alpha_h$  and pulse is not transform-limited giving a TBP of 0.009. For 2 value of  $\alpha_h$  RIN becomes effective at the fundamental mode-locking frequency of 2.5 GHz making transform-limited pulse unobtainable with both spontaneous and carrier noise.

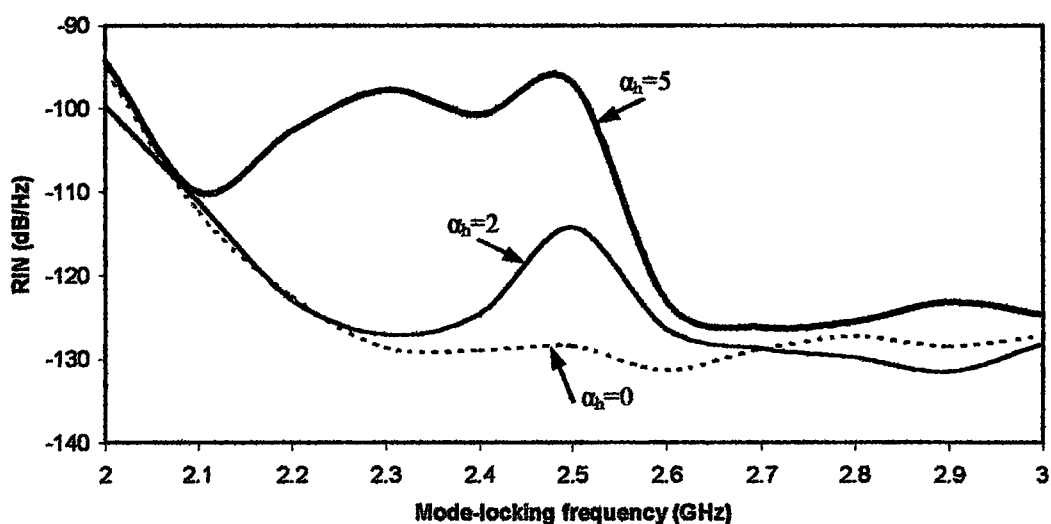
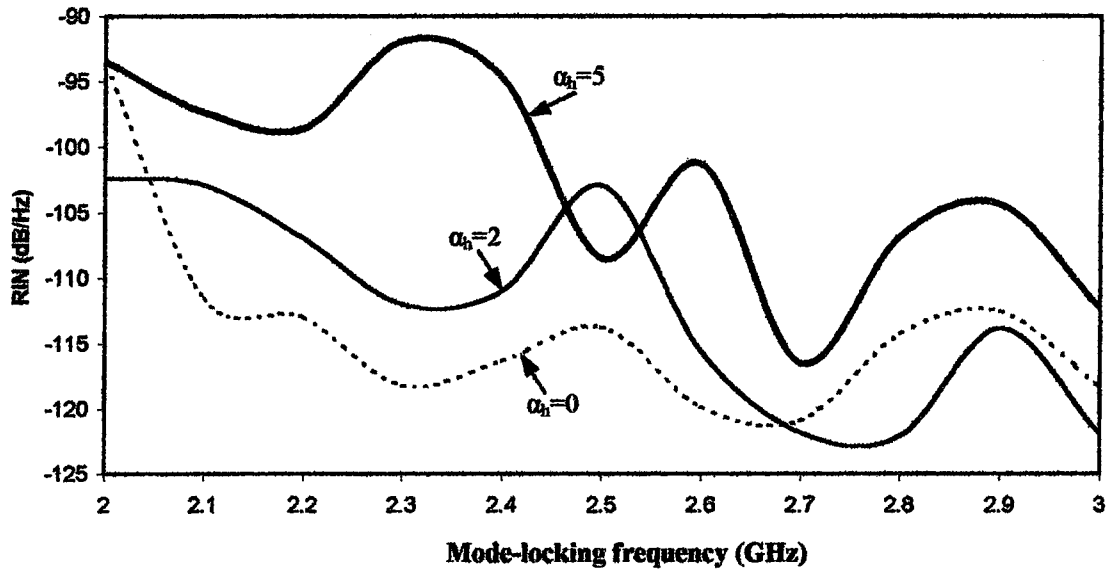
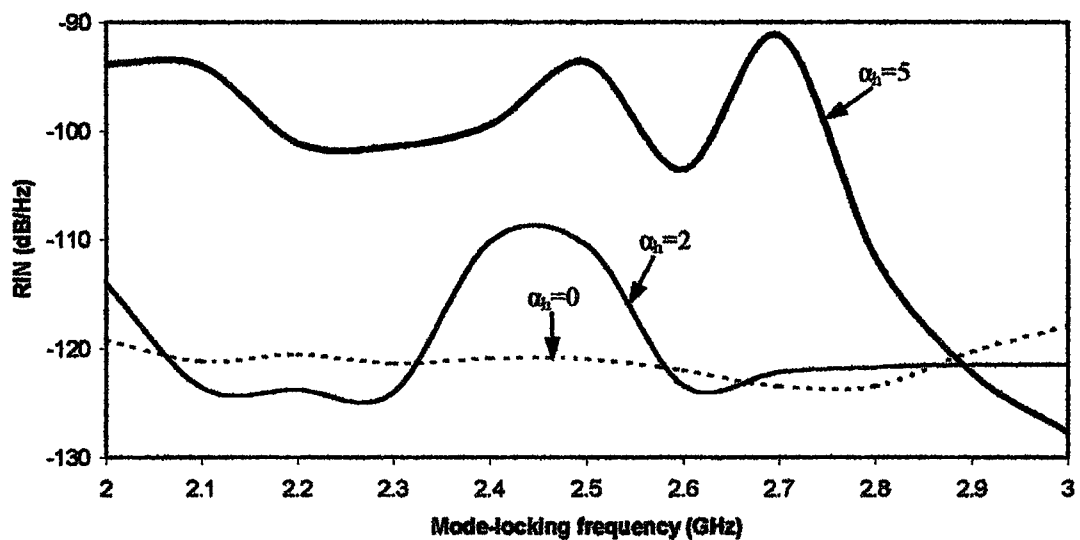


Figure 6.21 RIN spectrum of HSPS with linearly chirped Gaussian apodized FBG for different  $\alpha_h$  with spontaneous noise



**Figure 6.22** RIN spectrum of HSPS with linearly chirped Gaussian apodized FBG for different  $\alpha_h$  with both spontaneous and carrier noise

Figure 6.23 and 6.24 shows the RIN of HSPS with linearly chirped uniform FBG for different  $\alpha_h$ . Obtained results for this FBG are similar to linearly chirped Gaussian apodized FBG. If  $\alpha_h$  is zero, TBP has a value of greater than 0.5 at the mode-locking frequencies of 2, 2.6, 2.7 and 3 GHz without noise, at the mode-locking frequencies of 2, 2.2, 2.6, 2.7 and 2.8 GHz with spontaneous noise and at the mode-locking frequencies of 2.1, 2.2, 2.4, 2.7 and 2.8 with both spontaneous and carrier noise. For large value of  $\alpha_h$  RIN is high and TBP is less than 0.3. All of these results are not suitable for long distance soliton transmission and pulse is not transform-limited.



**Figure 6.23** RIN spectrum of HSPS with linearly chirped uniform FBG for different  $\alpha_h$  with spontaneous noise

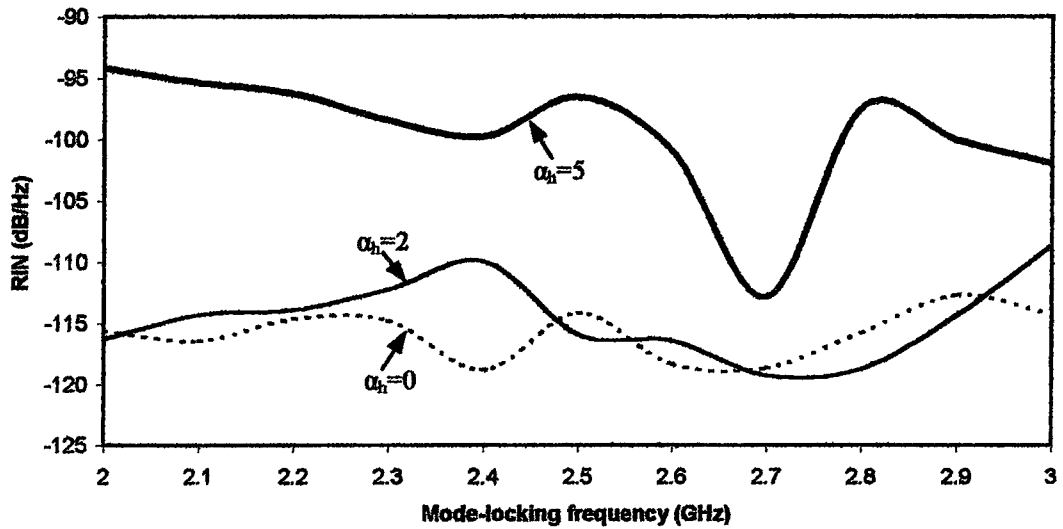


**Figure 6.24** RIN spectrum of HSPS with linearly chirped uniform FBG for different  $\alpha_h$  with both spontaneous and carrier noise

RIN spectrum of HSPS with Gaussian apodized FBG is given in Figure 6.25 and 6.26. For this grating transform limited pulses are only generated at the mode-locking frequency of 2.2 GHz giving a RIN value of -103.71 dB as seen in Figure 6.25 when  $\alpha_h$  is 5 with spontaneous noise. However, these pulses are obtained 800 MHz range with its zero value.

All of frequency range transform-limited pulses is not generated for 5 value of  $\alpha_h$  if both spontaneous and carrier noise is considered. Transform limited pulses are generated frequency range of 700 MHz for zero value of  $\alpha_h$  and frequency range of 300 MHz for its 2 value although RIN value is approximately same with two values of this parameter between the mode-locking frequency range of 2.3-3 GHz as shown in Figure 6.26.

It is also found that on the contrary of linearly chirped uniform and linearly chirped Gaussian apodized FBGs if  $\alpha_h$  increases, TBP increases and difference in pulsewidths when  $\alpha$  is changed between 0 and 5 is very little.

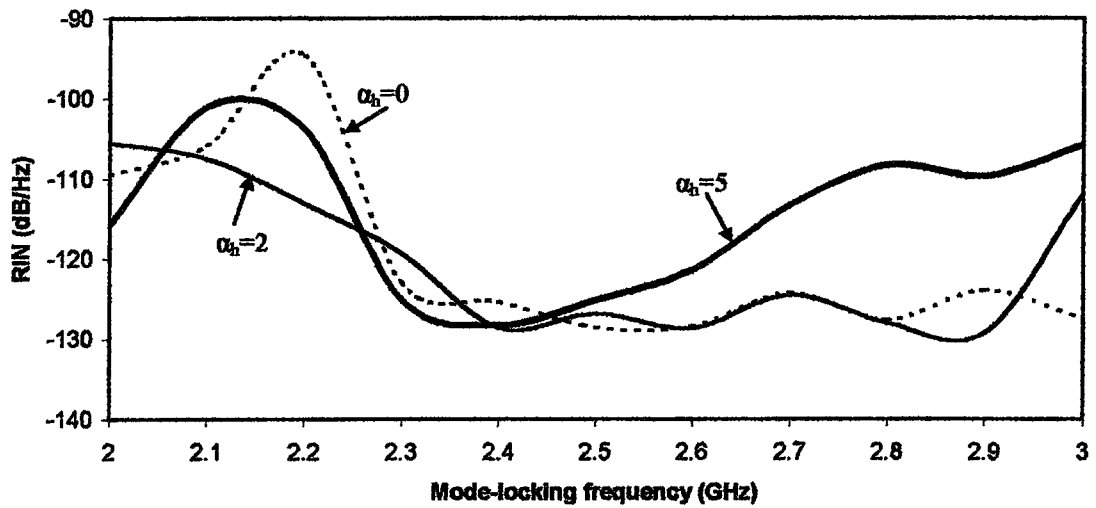


**Figure 6.25** RIN spectrum of HSPS with Gaussian apodized FBG for different  $\alpha_h$  with spontaneous noise

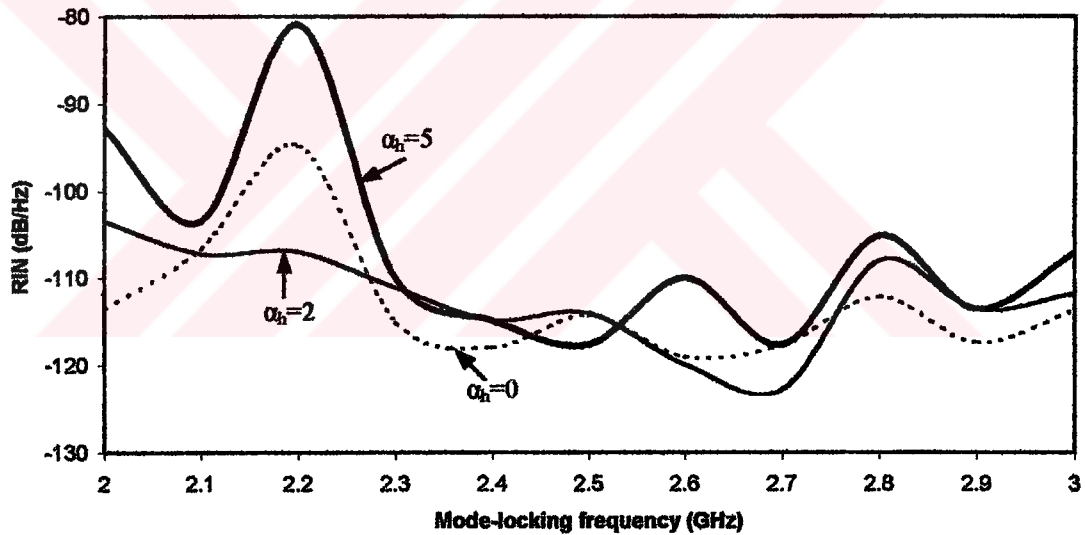


**Figure 6.26** RIN spectrum of HSPS with Gaussian apodized FBG for different  $\alpha_h$  with both spontaneous and carrier noise

Similar results are also obtained for uniform FBG as in Gaussian apodized FBG. In this case, transform limited pulses are generated at the mode-locking frequencies of 2-3 GHz except the frequencies of 2.1 and 2.2 GHz for zero value of  $\alpha_h$  if spontaneous and both spontaneous and carrier noise is taken into account. RIN values are  $-115.26$  dB and  $-97.22$  dB with spontaneous noise as shown in Figure 6.27 and  $-114.90$  dB and  $-101.19$  dB with both spontaneous and carrier noise as shown in Figure 6.28 at the corresponding frequencies. If  $\alpha_h$  is taken 5, transform

limited pulses are only obtained at the mode-locking frequency of 3 GHz where as RIN is also low for the other mode-locking frequencies as seen in Figure 6.27 and 6.28.

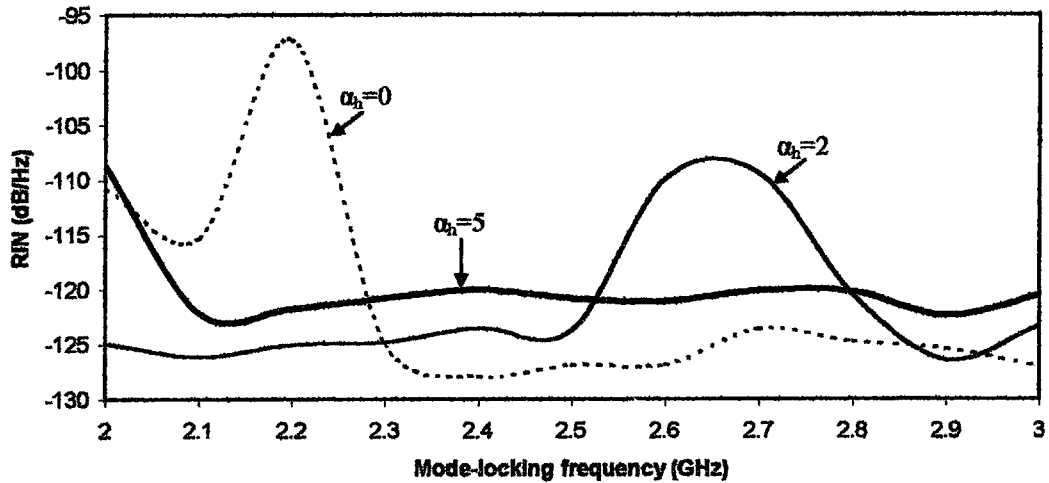


Figure 6.27 RIN spectrum of HSPS with uniform FBG for different  $\alpha_h$  with spontaneous noise

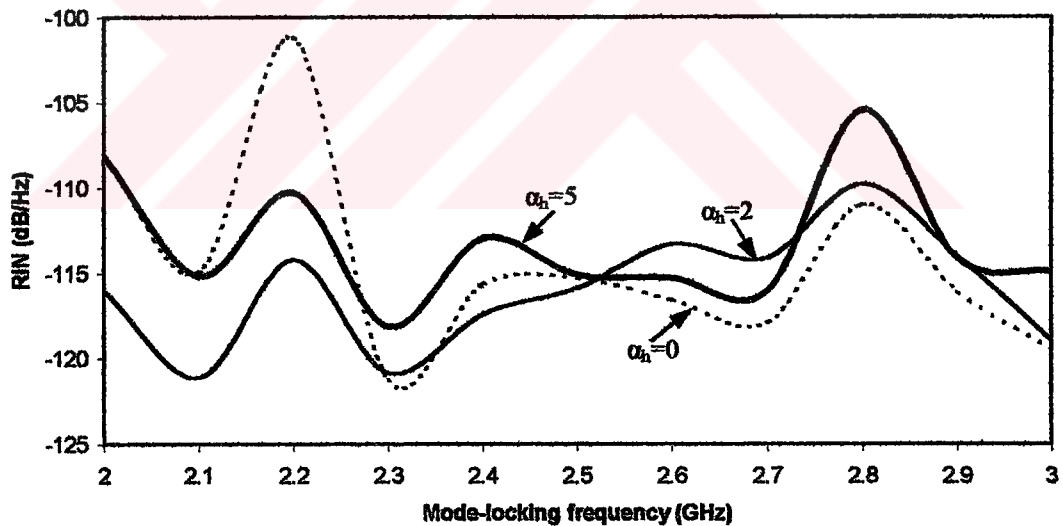


Figure 6.28 RIN spectrum of HSPS with uniform FBG for different  $\alpha_h$  with both spontaneous and carrier noise

All of these results show that  $\alpha_h$  is an important parameter for mode-locked and noise analysis and it affects the system operation with and without noise as seen in Table 6.1 and 6.2. Therefore, suitable value of  $\alpha_h$  should be used and 2 are the best choice in our analysis.

## 6.4.2 Gain Compression Factor

Gain compression ( $\varepsilon$ ) (also referred to as gain saturation) is an important phenomenon for semiconductor lasers, especially for InGaAsP based systems which exhibits very high gain compression. Gain compression is caused by several mechanisms such as spatial hole burning (in both lateral and longitudinal directions), spectral hole burning and other nonlinearities. Spatial hole burning can be neglected in high speed InGaAsP lasers due to the more dominant effect of the spectral hole burning. Spectral hole burning give rise power-dependent gain. The power dependent gain has been used to explain the experimental results wherein the dominant mode shifts towards longer wavelengths with an increase in device current.

In our simulations, we observed that if  $\varepsilon$  increases, noise peak shifts towards to the lower frequency and its value increases for HSPS with linearly chirped Gaussian apodized and linearly chirped uniform FBGs as shown in Figures 6.29-6.32. The reason for this the wavelength dependent gain gives a wavelength dependence of the number of photons. An increasing  $\varepsilon$  leads to a decreasing gain and increasing refractive index. An increasing refractive index means a decreasing frequency (or increasing wavelength) as explained before in the previous paragraph since resonance condition has to be maintained.

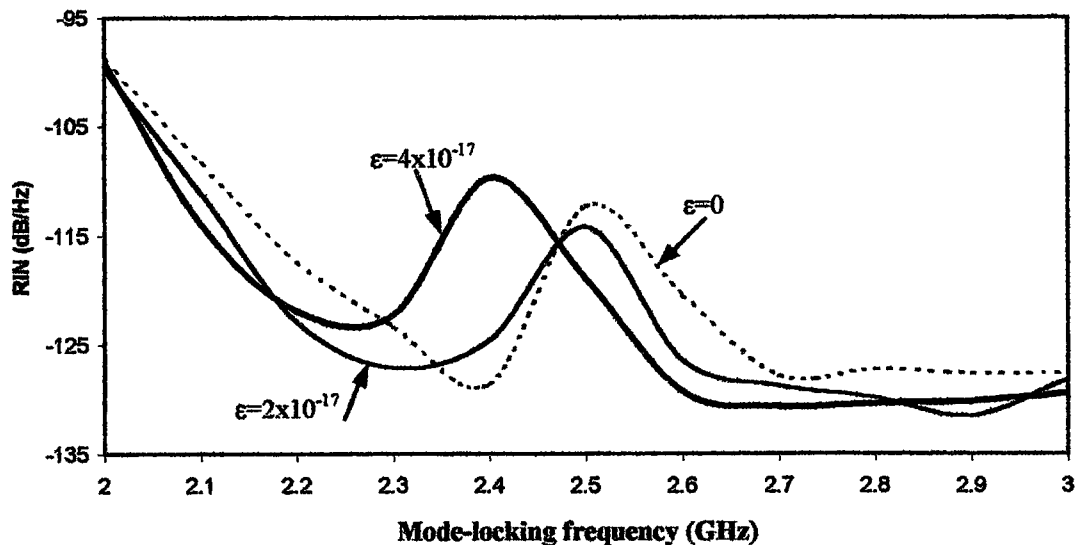


**Figure 6.29** RIN spectrum of HSPS for linearly chirped Gaussian apodized FBG for different  $\varepsilon$  with spontaneous noise



The effect of this parameter on the RIN of HSPS with linearly chirped Gaussian apodized FBG is given in Figure 6.29 and 6.30. Transform-limited pulses are generated over a wide frequency range of 2-3 GHz with spontaneous noise for zero and  $4 \times 10^{-17}$  value of  $\epsilon$  in addition the standard value of its. As seen in Figure 6.29 noise peak shifts to the 2.4 GHz for  $4 \times 10^{-17}$  and it is observed that for large value of  $\epsilon$  RIN increases and transform-limited pulses are not obtained at the mode-locking frequency where noise peak locates. On the other hand, transform-limited pulses are not generated at the mode-locking frequency of 2.5 GHz for zero value of  $\epsilon$  that has a RIN value of  $-99.11$  dB, at mode-locking frequency of 2.5 GHz for  $2 \times 10^{-7}$  that has a RIN value of  $-102.903$  dB and at mode-locking frequencies of 2.4 and 2.5 GHz for  $4 \times 10^{-17}$  that has a RIN values of  $-102.87$  dB and  $-106.49$  dB with both spontaneous and carrier noise. Also, noise peak shifts to the mode-locking frequency of 2.4 as seen in Figure 6.30.

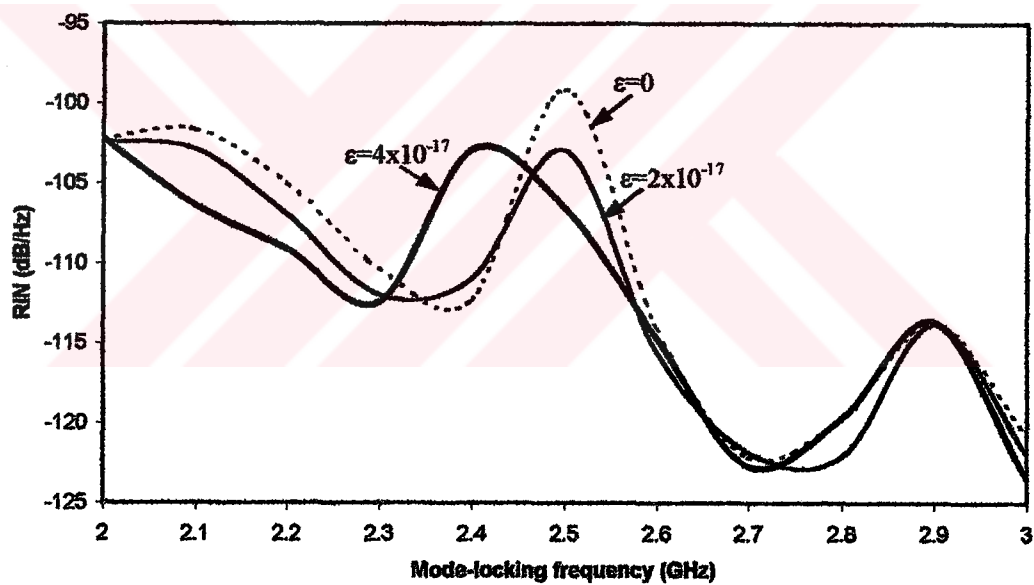


**Figure 6.30** RIN spectrum of HSPS for linearly chirped Gaussian apodized FBG for different  $\epsilon$  with both spontaneous and carrier noise

Figure 6.31 shows the effect of this parameter on the RIN for linearly chirped uniform FBG with spontaneous noise. As seen in figure there is a noise peak at the mode-locking frequency of 2.5 GHz for zero value of  $\epsilon$  and its RIN value is  $-103.34$  dB. For  $4 \times 10^{-17}$  noises peak locates at the mode-locking frequency of 2.4 GHz and it has a RIN value of  $-100.24$  dB. Transform-limited pulses are not generated only at these frequencies. If both of noise is considered, in this case, transform-limited

pulses are not generated only at the mode-locking frequency of 2.4 GHz for  $4 \times 10^{-17}$  and as seen in Figure 6.32 noise peak locates at this frequency giving a RIN value of  $-98.07$  dB.

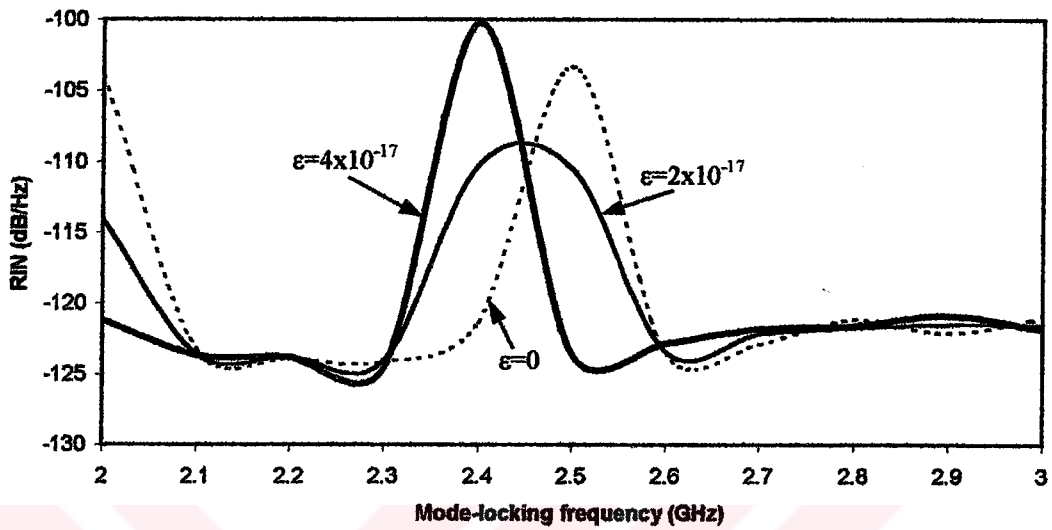


Figure 6.31 RIN spectrum of HSPS for linearly chirped uniform FBG for different  $\epsilon$  with spontaneous noise

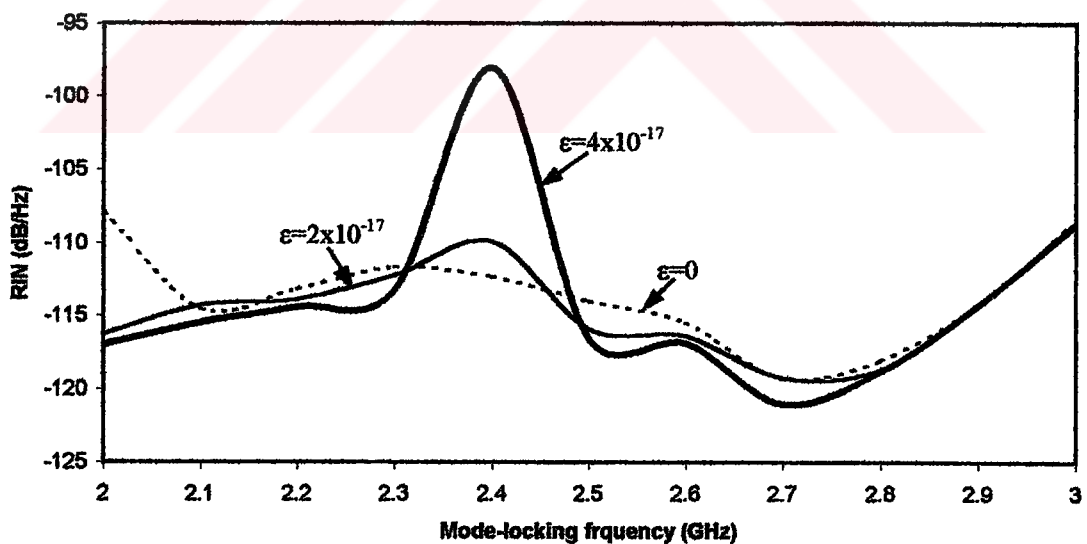


Figure 6.32 RIN spectrum of HSPS for linearly chirped uniform FBG for different  $\epsilon$  with both spontaneous and carrier noise

It is also found that although pulsewidth and TBP are slightly sensitive to this parameter except the mode-locking frequency that noise peak locates, effect of  $\epsilon$  on spectral width is very low with and without noise.

Figure 6.33-6.36 shows RIN spectrums of HSPS with Gaussian apodized and uniform FBGs for different value of  $\epsilon$  when HSPS includes spontaneous and both spontaneous and carrier noise. As seen in figures all of  $\epsilon$  values RIN is approximately same for these gratings. Transform limited pulses are only generated at the mode-locking frequencies of 2.1, 2.2 and 2.3 GHz for Gaussian apodized FBG and 2.6 and 2.7 GHz for uniform FBG with all of case.

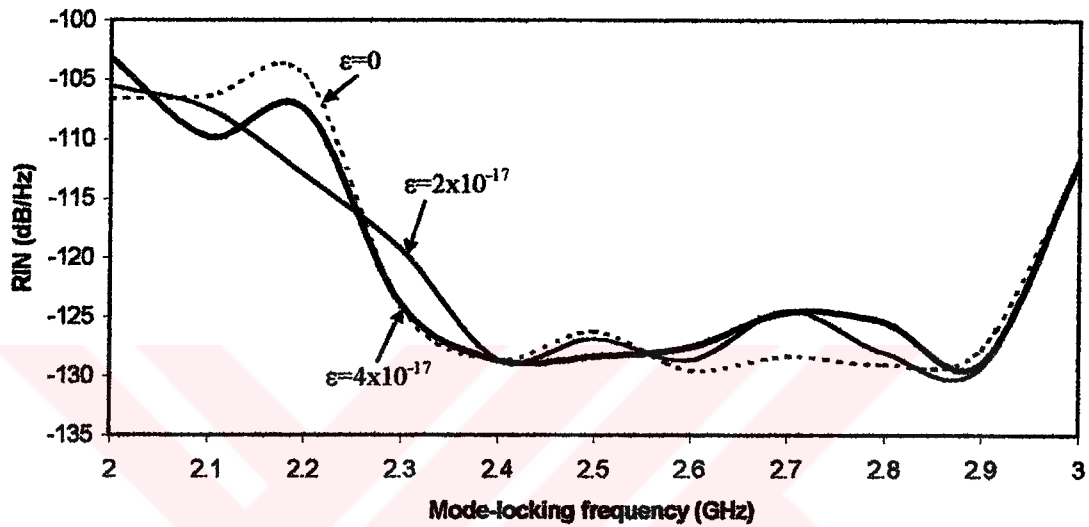


Figure 6.33 RIN spectrum of HSPS for Gaussian apodized FBG for different  $\epsilon$  with spontaneous noise

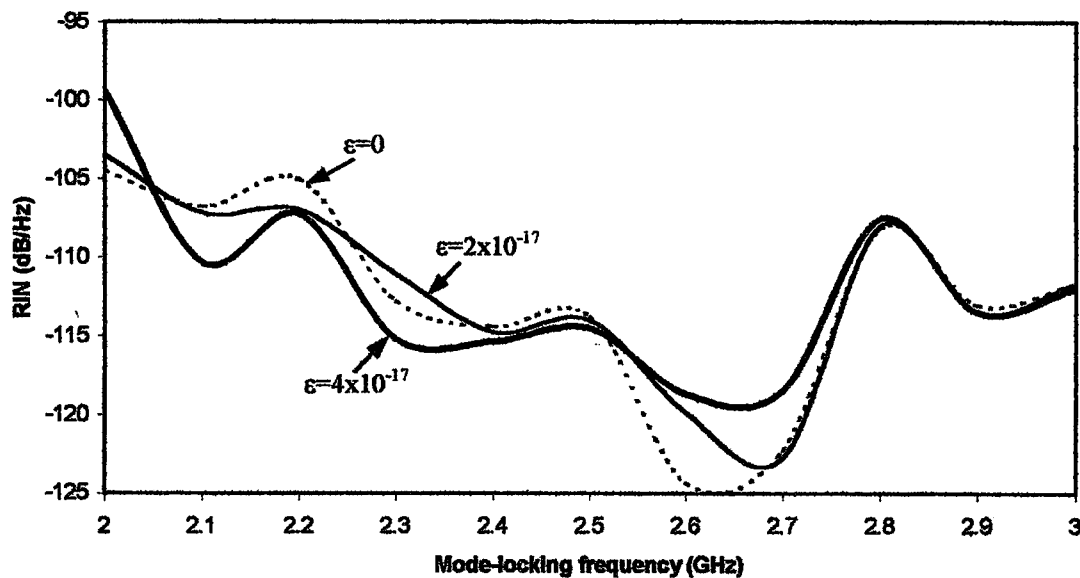


Figure 6.34 RIN spectrum of HSPS for Gaussian apodized FBG for different  $\epsilon$  with both spontaneous and carrier noise

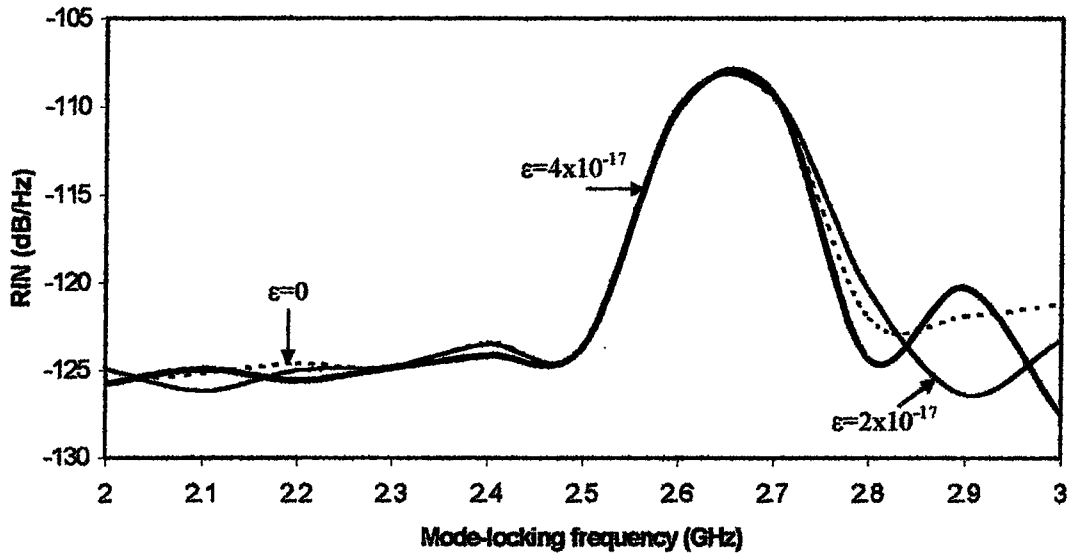


Figure 6.35 RIN spectrum of HSPS for uniform FBG for different  $\epsilon$  with spontaneous noise

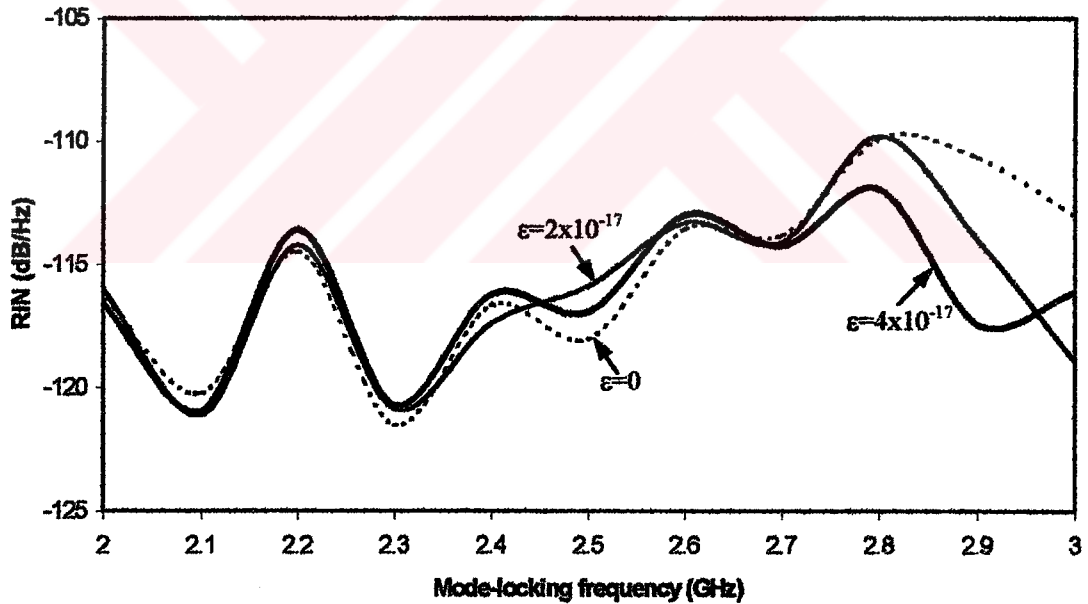


Figure 6.36 RIN spectrum of HSPS for uniform FBG for different  $\epsilon$  with both spontaneous and carrier noise

It is expected that with  $\epsilon=0$  the calculated resonance RIN peak would be much higher, but it is not as seen in the figures.

### 6.4.3 Spontaneous Coupling Factor

Spontaneous recombination events happen to supply a photon into the lasing field a fraction of spontaneous coupling factor ( $\beta_{sp}$ ). This term is important for the dynamic behavior; without this term with  $P=0$  at  $t=0$ ,  $P$  would remain 0.

Figure 6.37 and 6.38 show RIN of HSPS for linearly chirped Gaussian apodized FBG with spontaneous and both spontaneous and carrier noise and as shown in figures RIN increases with increasing  $\beta_{sp}$ . With spontaneous noise RIN is high for  $20 \times 10^{-5}$  at the fundamental mode-locking frequency of 2.5 GHz as seen in Figure 6.37 and it gives a RIN value of -106.37 dB. Transform-limited pulses are not generated only at this frequency giving a TBP of 0.036 as seen in Table 6.3. Transform-limited pulses are generated over a wide frequency range of 1 GHz (2-3 GHz) other values of  $\beta_{sp}$ .

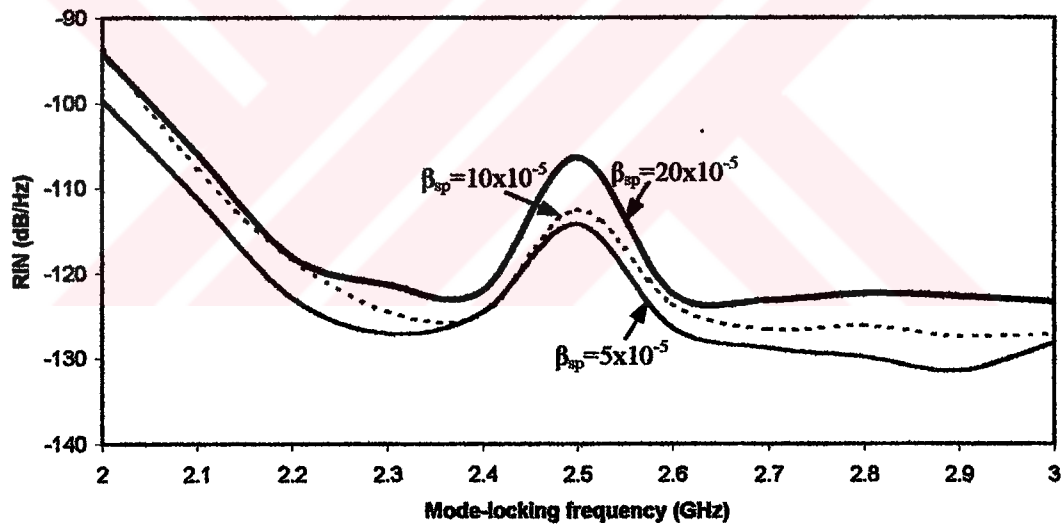


Figure 6.37 RIN spectrum of HSPS for linearly chirped Gaussian apodized FBG for different  $\beta_{sp}$  with spontaneous noise

Table 6.3 Effects of varying  $\beta_{sp}$  for linearly chirped Gaussian apodized FBG

$\beta_{sp}$	Pulsewidth (ps)	Spectral width (GHz)	TBP
$5 \times 10^{-5}$	45.38/40.55*/1.278**	8.68/8.60*/8.80**	0.394/0.349*/0.011**
$10 \times 10^{-5}$	45.47/32.53*/0.963**	8.71/8.68*/8.81**	0.396/0.282*/0.008**
$20 \times 10^{-5}$	45.60/3.99*/0.775**	8.73/8.98*/8.69**	0.398/0.036*/0.007**

\* with spontaneous noise, \*\* with both spontaneous and carrier noise

RIN spectrum is given in Figure 6.38 if both spontaneous and carrier noise is considered. As seen in figure RIN spectrum has peaks at the fundamental frequency of 2.5 GHz and it gives minimum RIN peak value of -102.90 dB for standard value of this parameter. Transform-limited pulses are not generated at this frequency for all of values of  $\beta_{sp}$  as seen Table 6.3. Transform-limited pulses are also not generated at the mode-locking frequencies of 2 GHz for  $10 \times 10^{-5}$  and 2 and 2.4 GHz for  $20 \times 10^{-5}$  values of  $\beta_{sp}$ .

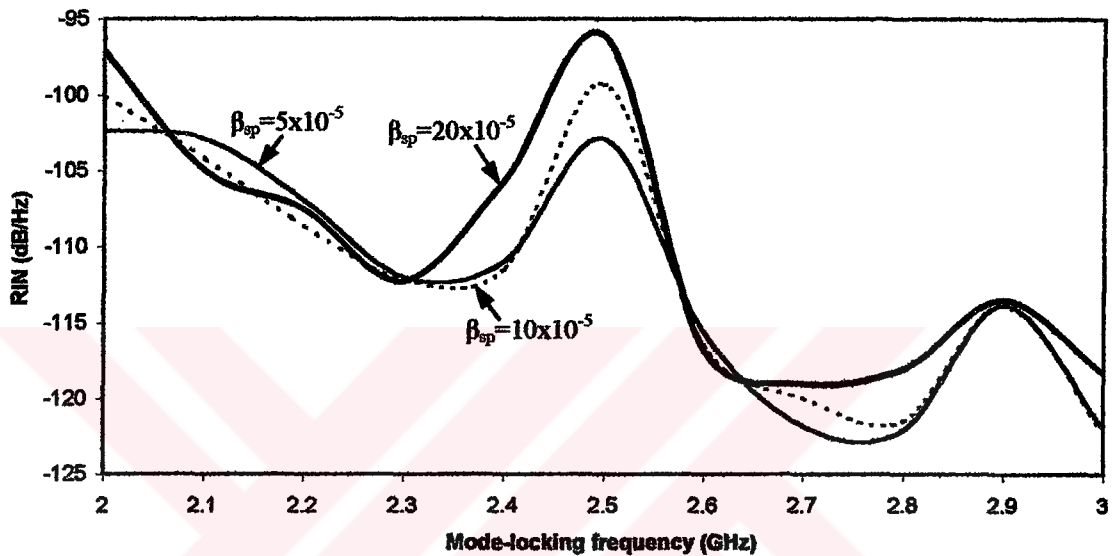
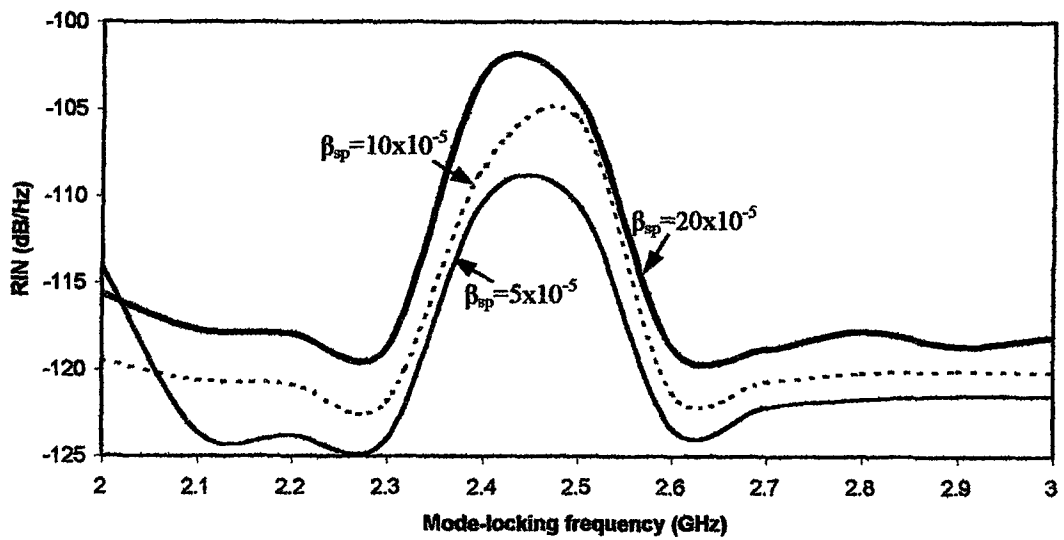


Figure 6.38 RIN spectrum of HSPS for linearly chirped Gaussian apodized FBG for different  $\beta_{sp}$  with spontaneous and carrier noise

As seen in the Table 6.3 pulsewidth and TBP is slightly sensitive to  $\beta_{sp}$  without noise and this parameter becomes especially effective at the fundamental mode-locking frequency with noise. Effect of this parameter on spectral width is very low with and without noise as seen in table.

RIN spectrum of linearly chirped uniform FBG is given in Figure 6.39 and 6.40. As seen in figures RIN increases with increasing  $\beta_{sp}$  as in linearly chirped Gaussian apodized FBG. Transform-limited pulses are not generated only at the mode-locking frequencies of 2.4 and 2.5 GHz with spontaneous noise and corresponding RIN values are -102.88 dB and -104.50 dB as seen in Figure 6.39 for  $20 \times 10^{-5}$  value of  $\beta_{sp}$ . As seen in Table 6.4 and 6.5 pulsewidth and TBP is not suitable for soliton transmission systems at these frequencies. For  $10 \times 10^{-5}$  transform-limited pulses are

not obtained only at the mode-locking frequency of 2.5 GHz giving a TBP of 0.212 as seen in Table 6.4 and it gives a RIN value of  $-105.65$  dB as shown in Figure 6.39.



**Figure 6.39** RIN spectrum of HSPS for linearly chirped uniform FBG for different  $\beta_{sp}$  with spontaneous noise

If both spontaneous and carrier noise is taken into account, as seen in Figure 6.40 RIN value is very high at the mode- locking frequency of 2.4 GHz for  $20 \times 10^{-5}$  and it has a RIN value of  $-103.73$  dB. Transform-limited pulses are not obtained only at this frequency giving a TBP of 0.042 as seen in Table 6.5. However, other values of  $\beta_{sp}$  transform-limited pulses are generated at all of mode-locking frequencies.

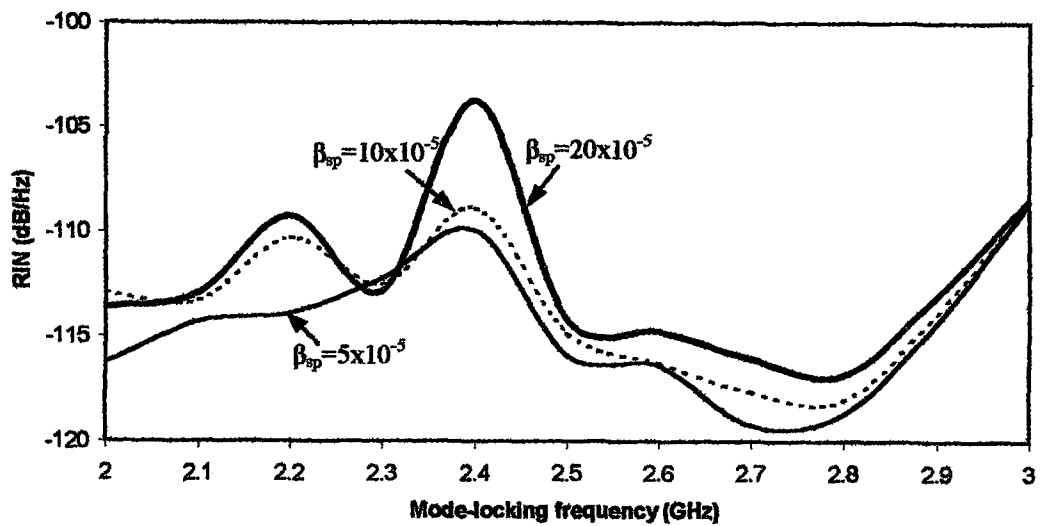


**Figure 6.40** RIN spectrum of HSPS for linearly chirped uniform FBG for different  $\beta_{sp}$  with both spontaneous and carrier noise

**Table 6.4** Effects of varying  $\beta_{sp}$  for linearly chirped uniform FBG at the mode-locking frequency of 2.5 GHz

$\beta_{sp}$	Pulsewidth (ps)	Spectral width (GHz)	TBP
$5 \times 10^{-5}$	45.69/34.23*/37.66**	8.73/9.07*/9.03**	0.399/0.310*/0.340**
$10 \times 10^{-5}$	44.57/23.33*/35.61**	8.73/9.07*/9.01**	0.389/0.212*/0.321**
$20 \times 10^{-5}$	42.84/18.92*/35.39**	8.73/8.80*/8.99**	0.374/0.167*/0.318**

**Table 6.5** Effects of varying  $\beta_{sp}$  for linearly chirped uniform FBG at the mode-locking frequency of 2.4 GHz

$\beta_{sp}$	Pulsewidth (ps)	Spectral width (GHz)	TBP
$5 \times 10^{-5}$	46.98/34.28*/38.39**	8.42/8.41*/8.13**	0.396/0.288*/0.312**
$10 \times 10^{-5}$	47.22/31.49*/36.97**	8.43/8.39*/8.12**	0.398/0.264*/0.300**
$20 \times 10^{-5}$	46.61/5.23*/5.193**	8.43/8.22*/8.07**	0.393/0.043*/0.042**

\* with spontaneous noise, \*\* with both spontaneous and carrier noise

Again as seen in Table 6.4 and 6.5 effect of  $\beta_{sp}$  on pulsewidth and TBP is little without noise and it becomes effective at the mode-locking frequencies of 2.4 and 2.5 GHz with noise. Spectral width is slightly sensitive to this parameter with and without noise as seen in tables.

HSPS with Gaussian apodized FBG is not affected by this parameter and all of case RIN spectrum is approximately same as seen in Figure 6.41 and 6.42. For different values of this parameter transform-limited pulses are generated only at the mode-locking frequencies of 2.1, 2.2 and 2.3 GHz with spontaneous noise and both of noise.

If uniform FBG is considered, transform-limited pulses are obtained only at the mode-locking frequency of 2.5 GHz for  $10 \times 10^{-5}$  and 2 GHz for  $20 \times 10^{-5}$  with spontaneous noise. RIN values are  $-109.81$  dB and  $-107.85$  dB at these frequencies as seen in Figure 6.43. With spontaneous and carrier noise transform-limited pulses are generated only at the mode-locking frequency of 2.6 and 2.7 GHz and RIN has a value of  $-112.45$  dB and  $-114.13$  dB as seen in Figure 6.44 for  $10 \times 10^{-5}$ . For  $20 \times 10^{-5}$  these pulses are obtained only at the mode-locking frequency of 2.6 GHz and RIN value is  $-111.51$  dB as seen in Figure 6.44.



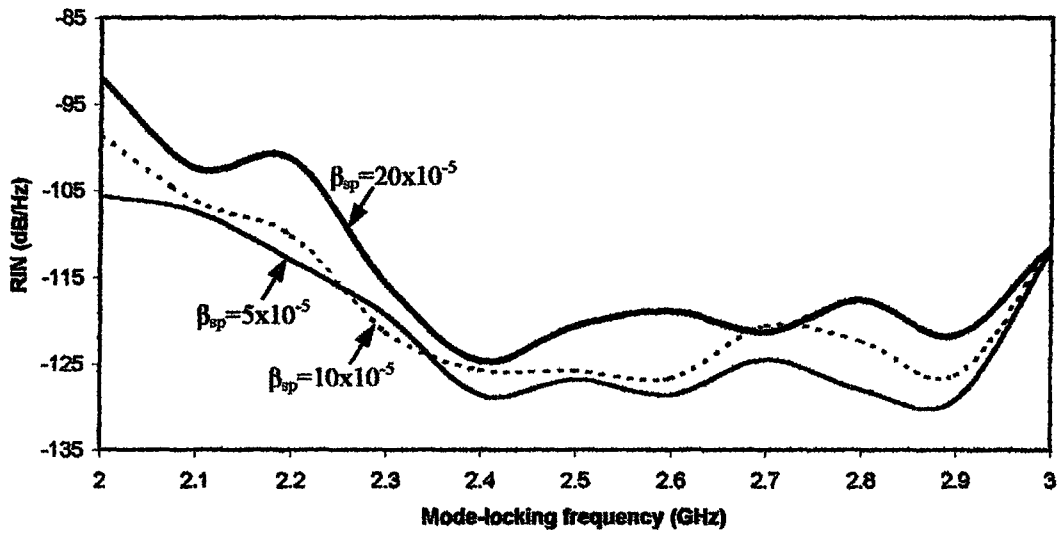


Figure 6.41 RIN spectrum of HSPS for Gaussian apodized FBG for different  $\beta_{sp}$  with spontaneous noise

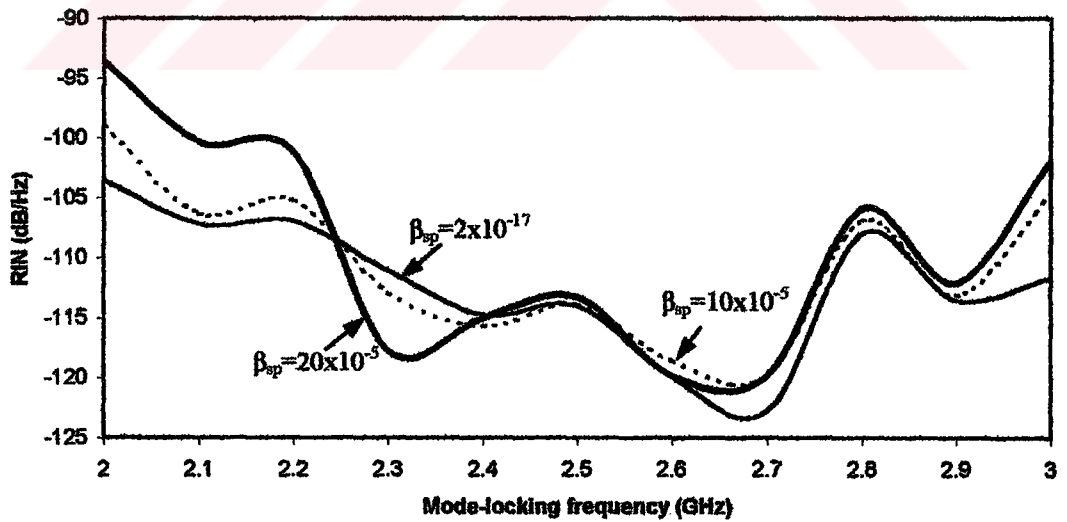


Figure 6.42 RIN spectrum of HSPS for Gaussian apodized FBG for different  $\beta_{sp}$  with both spontaneous and carrier noise

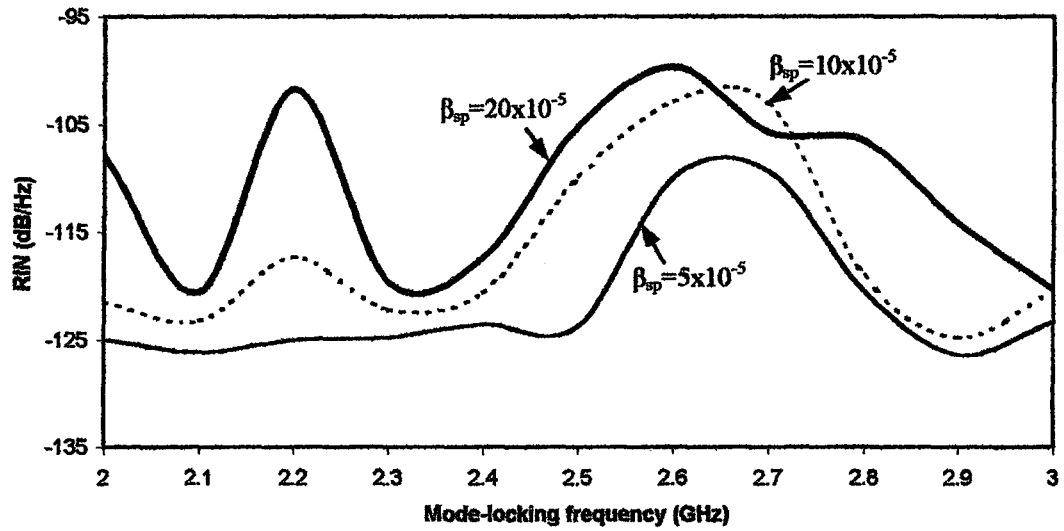


Figure 6.43 RIN spectrum of HSPS for uniform FBG for different  $\beta_{sp}$  with spontaneous noise

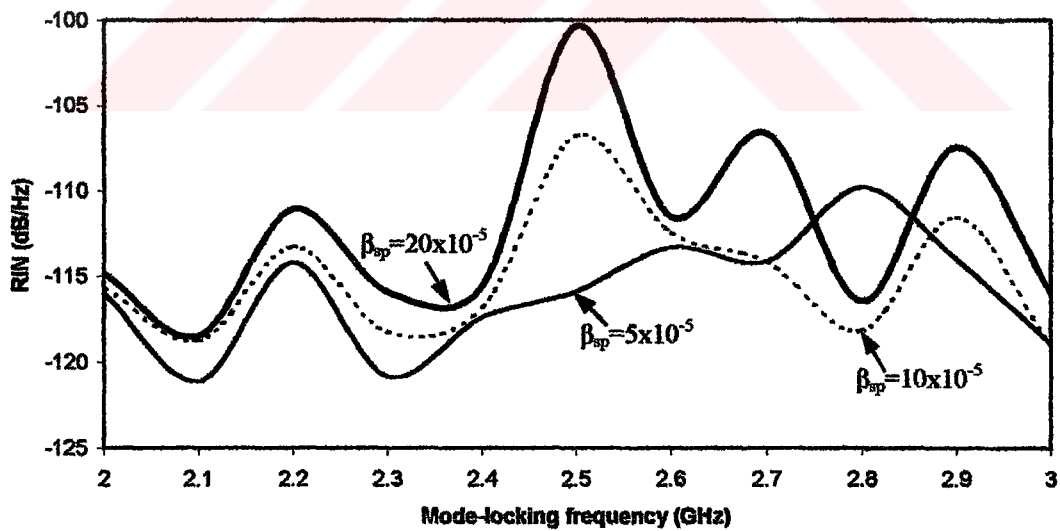


Figure 6.44 RIN spectrum of HSPS for uniform FBG for different  $\beta_{sp}$  with both spontaneous and carrier noise

Briefly, as seen the results although even  $\alpha_h$  affects the pulsewidth and TBP of HSPS without noise,  $\epsilon$  and  $\beta_{sp}$  becomes effective only with noise. Noise increases with increasing value of these parameters. For a large amount of mode-locking frequencies transform-limited pulses are not generated with increasing  $\alpha_h$ . However,  $\beta_{sp}$  is mainly effective at the fundamental mode-locking frequency of 2.5 GHz for linearly chirped Gaussian apodized FBG and 2.4 and 2.5 GHz for linearly chirped uniform FBG. Transform-limited pulses are not obtained at these corresponding frequencies. Noise peak shifts to the lower frequencies with large value of  $\epsilon$  and transform-limited pulses are not generated at the mode-locking frequencies that noise peak locates.

## 6.5 RIN Reduction in Mode-locked HSPS

Up to now we have considered effect of spontaneous and carrier noise on mode-locked HSPS and RIN. In this section, it will be showed that RIN reduction is possible for the mode-locked HSPS by selecting a suitable apodization function such as Gaussian and linear chirp rate. For that reason all of gratings are compared with low and high noise at the mode-locking frequency where transform-limited pulses are generated.

If spontaneous noise is only taken into account and its value is low, mode-locking of HSPS with Gaussian apodized FBG generates transform limited pulses only at the mode-locking frequencies of 2.1, 2.2, and 2.3 GHz and it gives RIN values of -107.45, -113.02, -119.28 dB at these frequencies as shown in Figure 6.45. Mode-locking of HSPS with uniform FBG only gives transform-limited pulses at the mode-locking frequencies of 2.6 GHz and 2.7 GHz, and corresponding RIN values are -109.8 dB and -110 dB as shown in Figure 6.45. If RIN values of mode-locked HSPS with these gratings are compared at the mode-locking frequencies where transform-limited pulses are generated, RIN of mode-locked HSPS with uniform FBG is higher than mode-locked HSPS with Gaussian apodized FBG although HSPS with Gaussian apodized FBG is mode-locked at low mode-locking frequencies. These results show that using Gaussian apodized FBG instead of uniform FBG can reduce RIN in mode-locked HSPS.

Mode-locked HSPS with linearly chirped FBG gives RIN values of -123.4 dB and -122 dB, respectively, as shown in Figure 6.45 at the corresponding mode-locking frequencies of HSPS with uniform FBG that generates transform limited pulses. Comparison of RIN values shows that mode-locked HSPS with linearly chirped FBG has lower RIN value than mode-locked HSPS with uniform FBG. Mode-locked HSPS with linearly chirped uniform FBG also gives low RIN values when the results are compared at the mode-locking frequencies of HSPS with Gaussian apodized FBG that transform-limited pulses are generated. As a result, introducing suitable linear chirp value into uniform FBG can reduce RIN of mode-locked HSPS.

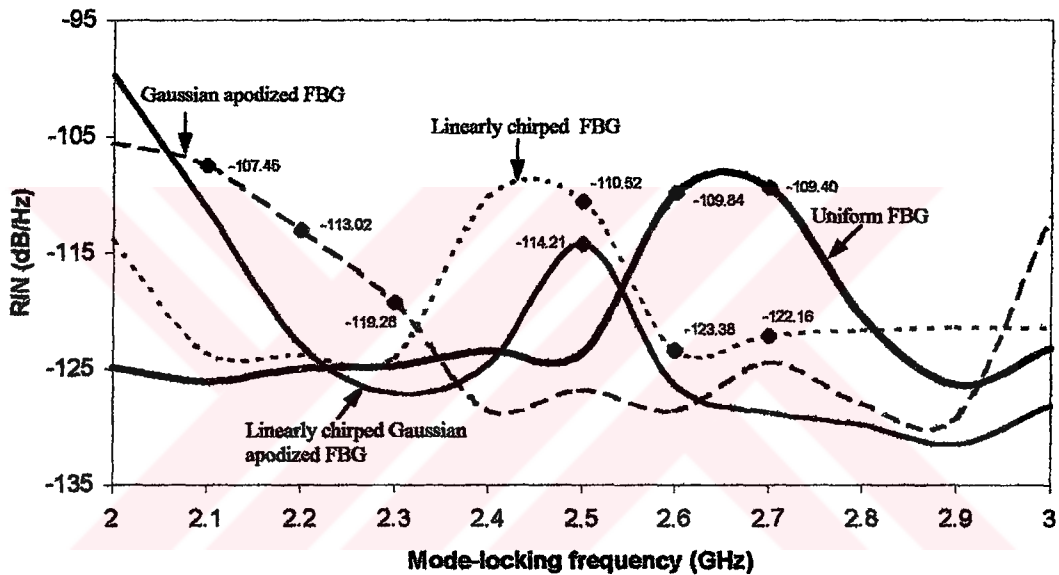


Figure 6.45 RIN spectrum of HSPS with low spontaneous noise ( $\beta_{sp}=5 \times 10^{-5}$ )

Transform limited pulses are obtained from mode-locked HSPS with linearly chirped uniform and linearly chirped Gaussian apodized FBGs over a wide tuning range as explained before. RIN value of mode-locked HSPS with linearly chirped Gaussian apodized FBG is approximately 4 dB lower than mode-locked HSPS with the linearly chirped uniform FBG at the fundamental mode-locking frequency of 2.5 GHz as seen in Figure 6.45. In addition to this, mode-locked HSPS with linearly chirped Gaussian FBG has lower RIN values than mode-locked HSPS with Gaussian apodized, uniform and linearly chirped uniform FBGs when the comparison is done at the respective mode-locking frequencies that transform-limited pulses are generated. Results show that linear chirp rate introduced into Gaussian apodized FBG further reduces RIN values of mode-locked HSPS.

If high spontaneous noise level is considered, in this case, transform-limited pulses are generated only at the mode-locking frequency of 2 GHz for uniform FBG and at the mode-locking frequencies of 2.1, 2.2, 2.3 and 2.6 GHz for Gaussian apodized FBG as explained before. Transform-limited pulses are not generated only at the mode-locking frequency of 2.5 GHz for linearly chirped Gaussian apodized FBG and 2.4 and 2.5 GHz for linearly chirped uniform FBG. If comparison is done only at the mode-locking frequency of 2.6 GHz, RIN value has approximately  $-118.695$  dB for Gaussian apodized and linearly chirped uniform FBGs as seen in Figure 6.46. RIN is  $-122.367$  dB for linearly chirped Gaussian apodized FBG as seen in Figure 6.46. Results show that linearly chirped Gaussian apodized FBG is approximately 4 dB lower than Gaussian apodized and linearly chirped uniform FBGs.

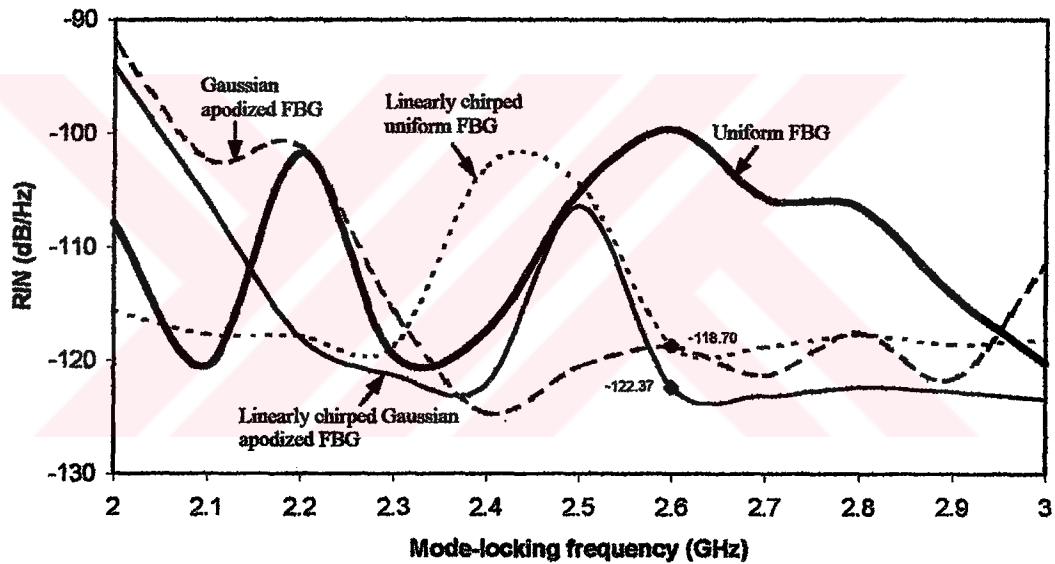
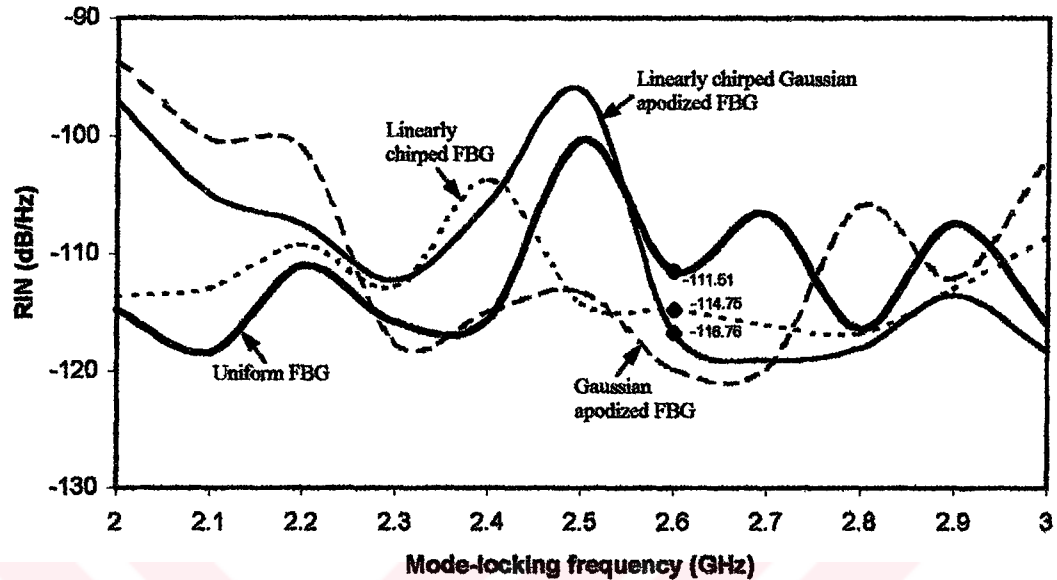


Figure 6.46 RIN spectrum of HSPS with high spontaneous noise ( $\beta_{sp}=20 \times 10^{-5}$ )

If high level of both spontaneous and carrier noise is included in HSPS, for this case, transform limited pulses are generated only at the mode-locking frequency of 2.6 GHz for uniform FBG and 2.2 and 2.3 GHz for Gaussian apodized FBG. Again results are compared only at the mode-locking frequency of 2.6 GHz. RIN is  $-111.507$  dB for uniform FBG,  $-114.747$  dB for linearly chirped uniform FBG and  $-116.764$  dB for linearly chirped Gaussian apodized FBG at the corresponding frequency as shown in Figure 6.47. Although linearly chirped Gaussian apodized FBG has lower RIN value than the linearly chirped uniform FBG between the

frequency ranges of 2.6-3 GHz, it has higher RIN value between the frequency ranges of 2-2.3 GHz as seen in figure.



**Figure 6.47** RIN spectrum of HSPS with high noise including spontaneous and carrier ( $\beta_{sp}=20 \times 10^{-5}$ )

From the obtained results, it is found that the use of a suitable apodization function and linear chirp rate in FBGs leads to RIN reduction in mode-locked HSPS that uses these gratings as external cavity. M. McAdams *et al.* [63] has showed that at lower frequencies RIN reduction is possible using an appropriate apodized grating for CW laser and they demonstrated 5 dB of RIN reduction. We obtained at least 4 dB of RIN reduction by using linearly chirped Gaussian apodized FBG in mode-locked HSPS under the condition that HSPS is mode locked and produces transform-limited pulses.

The main conclusion is that Gaussian apodized or uniform FBGs that are used as an external cavity in mode-locked HSPS are not suitable to obtain transform-limited pulses over a wide tuning range around the fundamental mode-locking frequency. Linear chirping of these gratings that will compensate the chirp in the laser is necessary to obtain transform-limited pulses over a wide tuning range from mode-locked HSPS. It is also found that using a suitable window function such as Gaussian apodized and introducing appropriate linear chirp value into these gratings RIN can be reduced in mode-locked HSPS.

## 6.6 Conclusions

In this chapter, RIN spectrum of HSPS with all gratings is given for different values of bias currents,  $\alpha_h$ ,  $\epsilon$ , and  $\beta_{sp}$  to show the effect of these parameters on output pulse of HSPS and RIN.

From the obtained results, for linearly chirped Gaussian apodized and linearly chirped uniform gratings noise increases with increasing  $\alpha_h$ ,  $\epsilon$ ,  $\beta_{sp}$  and some value of RF and DC currents. High value of noise generates a noise peak in the RIN spectrum making transform-limited pulses unobtainable. Therefore, transform-limited pulses are not generated over a wide tuning range. For Gaussian apodized and uniform gratings generated transform-limited pulses are not directly related to magnitude of noise. Transform-limited pulses are obtained only at a limited frequency range with these gratings with and without noise.

$\alpha_h$  affects the output pulse and TBP of HSPS with and without noise. For zero value of this parameter noise is very low but in this case TBP is greater than 0.5 at the some mode-locking frequencies. Therefore, proper mode-locking range that transform-limited pulses are generated reduces. However,  $\epsilon$ , and  $\beta_{sp}$  becomes effective only with noise especially at the fundamental mode-locking frequency of 2.5 GHz for linearly chirped Gaussian apodized gratings and at the mode-locking frequencies of 2.4 and 2.5 GHz for linearly chirped uniform gratings. Spectral width is slightly sensitive to these parameters and change in spectral width is very small with and without noise. It is also observed that if  $\epsilon$  increases, noise peak shifts to the lower frequencies.

In this section, it is also found that RIN reduction is possible for the mode-locked HSPS by selecting a suitable apodization function such as Gaussian and linear chirp rate. In this work, 4 dB of RIN reduction is obtained by using linearly chirped Gaussian apodized FBG in mode-locked HSPS

## **CHAPTER 7**

### **SUMMARY, CONCLUSIONS AND FUTURE WORK**

In this chapter, the results obtained in this thesis work are summarized and concluded. Also, some proposals future work are given.

#### **7.1 Summary**

In this thesis, "Effect of noise on mode-locked HSPS and RIN" was presented for different FBGs such as uniform, Gaussian apodized, linearly chirped uniform and linearly chirped Gaussian apodized.

First, output pulses of HSPS were investigated with spontaneous, carrier and both of these noises. Then, RIN spectrum was described with these noises and also different DC and RF currents,  $\alpha_h$ ,  $\beta_{sp}$ ,  $\epsilon$ . Finally, it was explained that how the RIN reduction is possible for mode-locked HSPS.

In Chapter 2, derivation of coupled-mode equations was made for uniform, chirp and apodized gratings. These equations were converted into the transfer matrix form by using the piecewise-uniform approach [37]. Solutions of coupled-mode equations for gratings were also explained in this chapter.

Chapter 3 was devoted to the results of FBGs. Reflection and group delay characteristics of all FBGs was explained for 0.5 and 0.99 peak reflectivity. Results show that chirping makes both the spectrum wider and the group delay linear and apodization suppresses the side-lobes in the reflection spectrum and ripples on the group delay curve [54].

A complete mathematical model of the mode-locked HSPS was explained in Chapter 4. In this chapter, it was shown that in order to model the complete HSPS, each section must be modeled separately. For example, coupled-mode equations include



gain, loss and noise for the laser section whereas they include only coupling for the grating section.

Results of output pulse of mode-locked HSPS with spontaneous and carrier noise was shown in Chapter 5. In this chapter it was found that when standard laser diode parameters are used, transform-limited pulses are generated over a wide tuning range around the fundamental frequency from the mode-locked HSPS with linearly chirped uniform and linearly chirped Gaussian apodized FBGs. Linear chirp introduced into FBGs plays an important role for the generation of mode-locked transform-limited pulses over a wide tuning range around the fundamental mode-locking frequency from HSPS with these gratings. Low spontaneous level does not affect these results. Carrier noise affects the output pulse of HSPS especially at the lower frequencies and at these frequencies transform-limited pulses are not generated. Both spontaneous and carrier noise may be effective at the fundamental mode-locking frequency of 2.5 GHz.

In Chapter 6, RIN spectrum of mode-locked HSPS was obtained for the different RF and DC currents, and also different value of  $\alpha_h$ ,  $\epsilon$ ,  $\beta_{sp}$ . It was observed that noise increases with increasing value of  $\alpha_h$ ,  $\epsilon$ ,  $\beta_{sp}$  and some value of RF and DC currents. High value of noise introduce noise peak in the RIN spectrum at the mode-locking frequency that transform-limited pulses are not generated. Therefore, proper mode-locking range where transform-limited pulses are generated reduces. How the RIN reduction is possible for mode-locked HSPS was also shown in this chapter.

## **7.2 Conclusions**

The results obtained in FBG model are concluded as follows:

1. The pitch of the grating must be linearly chirped in order to have a linear group delay characteristics and a single-lobed spectrum.
2. The grating must be apodized. The aim of using apodization is to reduce or to completely kill the side-lobes in the reflection spectrum of the grating. The transform-limited posing functions are suitable for this purpose.

Conclusions of the results of mode-locked HSPS are given below:

1. Carrier noise is as important as spontaneous noise and that inclusion of noise source  $F_N$  in the rate equations is necessary for accurate analysis of the noise.
2. Transform-limited pulses are generated only a limited tuning ranges for uniform and Gaussian apodized FBGs with and without noise. The generated transform-limited pulses with these FBGs are not related to magnitude of RIN.
3. Transform-limited pulses are generated over a wider frequency range with linearly chirped uniform and linearly chirped Gaussian apodized FBGs without noise and low noise level does not affect these results.
4. Noise increases with increasing value of  $\alpha_h$ ,  $\beta_{sp}$ , and  $\epsilon$ . A high level of noise affects the operation of device and it introduces noise peak in the RIN spectrum making transform-limited pulses unobtainable at the mode-locking frequency where noise peak locates. Therefore, mode locking range that transform-limited pulses are generated reduces.
5. Even  $\alpha_h$  affects the pulsewidth and TBP of mode-locked HSPS without noise,  $\beta_{sp}$  and  $\epsilon$  becomes effective only with noise. If  $\alpha_h$  increases, pulsewidth and TBP decreases with and without noise and TBP takes a value of less than 0.3 with noise.  $\beta_{sp}$  is mainly effective around the fundamental frequency of 2.5 GHz with noise and pulsewidth and TBP decrease with increasing value of this parameter. Also, if  $\epsilon$  increases, noise peak shifts to the lower frequency that transform-limited pulses are not generated.
6. RIN value is also extremely sensitive to DC and RF bias currents and noise increases for some value of these bias currents.
7. Using a suitable window function such as Gaussian apodized and introducing appropriate linear chirp value into gratings RIN can be reduced in mode-locked HSPS. Results show that linearly chirped Gaussian apodized FBG is approximately 4 dB lower than linearly chirped uniform FBGs.

All of these results show that the most suitable value of laser diode parameters should be used to generate transform-limited pulses over a wide frequency range and also to obtain low RIN.

### **7.3 Future Work**

As a future work, the following investigations and modifications can be considered:

- The effects of FBGs parameters on the RIN of mode-locked HSPS can be investigated.
- Intensity modulation of HSPS with FBGs can be considered.
- The effects of FBGs and laser diode parameters on the intensity modulation response of the HSPS can be identified.

## REFERENCES

1. Salethe, R. P. (1979). Diode laser coupled to external resonators. *Appl. Phys.*, **20**, pp. 1-18.
2. Kitaoka, Y., Sato, H., Mizuuchi, K., Yamamoto K. and Kato, M. (1996). Intensity noise of laser diodes with optical feedback. *IEEE J. Quantum Electron.*, **32**, no. 5, pp. 822-828.
3. Schunk, N. and Petermann, K. (1988). Numerical analysis of the feedback regimes for a single-mode semiconductor laser with external feedback. *IEEE J. Quantum Electron.*, **24**, no. 7, pp. 1242-1247.
4. Kallimani K. I. and O' Mahony, M. J. (1998). Relative intensity noise for laser diodes with arbitrary amounts of optical feedback. *IEEE J. Quantum Electron.*, **34**, no. 8, pp. 1438-1446.
5. Cartaxo, A. V. T. and Morgado, J. A. P. (2000). Analysis of semiconductor laser frequency noise taking into account multiple reflections in the external cavity. *IEE Proc. Opt.*, **147**, no. 5, pp. 335-344.
6. ——— (1987). Minimum bit rate of DPSK transmission for semiconductor laser with a long external cavity and strong linewidth reduction. *J. Lightwave Technol.*, **5**, pp. 1309-1314.
7. Langley, L. N., Turovets, S. I., and Shore, K. A. (1995). Targeting in nonlinear dynamics of laser diodes. *Proc. Ins. Elect. Eng.*, **142**, pp. 157-161.
8. Fujita, T., Ishizuka, S., Fujito, K., Serizawa, H. and Sato, H. (1984). Intensity noise suppression and modulation characteristics of a laser diode coupled to an external cavity. *IEEE J. Quantum Electron.*, **20**, pp. 492-499.
9. Fujita, T., Ohya, J., Serizawa, H. and Sato, H. (1985). Correlation between intensity noise and longitudinal modes of a semiconductor laser coupled to an external cavity. *J. Appl. Phys.*, **57**, pp. 1753-1756.

10. Tkach, R. W. and Chraplyvy, A. R. (1986). Regimes of feedback effects in 1.5- $\mu\text{m}$  distributed feedback lasers. *J. Lightwave Technol.*, **4**, pp. 1655-1661.
11. Wyatt, R. and Devlin, W. J. (1983). 10 kHz linewidth 1.5  $\mu\text{m}$  InGaAsP external cavity laser with 55 nm tuning range. *Electron. Lett.*, **19**, pp. 110-112.
12. Kazanirov, R. F., Henry, C. H., and Olsson, N. A. (1987). Narrow-band resonant optical reflectors and resonant optical transformers for laser stabilization and wavelength division multiplexing. *IEEE J. Quantum Electron.*, **23**, pp. 1419-1425.
13. Olsson, N. A., Henry, C. H., Kazanirov, R. F., Lee, H. J. and Orlowsky, K. J. (1988). Performance characteristics of a 1.5  $\mu\text{m}$  single frequency semiconductor laser with an external waveguide Bragg reflector. *IEEE J. Quantum Electron.*, **24**, pp. 143-147.
14. Ferreira, M. F., Rocha, J. F. and Pinto, J. L. (1990). Noise and modulation performance of Fabry-Perot and DFB semiconductor lasers with arbitrary external optical feedback. *Proc. Inst. Elect. Eng.*, **137**, pp. 361-369.
15. Zorabedian, P., Trutna, W. R., and Cutler, L. S. (1987). Bistability in grating-tuned external-cavity semiconductor lasers. *IEEE J. Quantum Electron.*, **23**, pp. 1855-1860.
16. Binder, J. O., Cormack, G. D., and Pinto, J. L. (1990). Intermodal tuning characteristics of an InGaAsP laser with optical feedback from an external grating reflector. *IEEE J. Quantum Electron.*, **26**, pp. 1191-1198.
17. Ahmed, Z. and Tucker, R. S. (1995). Small-signal IM response of grating terminated external cavity semiconductor lasers. *IEEE J. Select. Topics. Quantum Electron.*, **1**, pp. 505-515.
18. Morton, P. A., Mizrahi, V., Andrekson, P. A., Tanbun-Ek, T., Logan, R. A., Lemaire, P., Coblenz, D. L., Sergent, A. M., Wecht, K. W. and Sciortino Jr., P.

- F. (1993). Mode-locked hybrid soliton pulse source with extremely wide operating frequency range. *IEEE Photon. Tech. Lett.*, **5**, pp. 28-31.
19. Mollenauer, L. F., Lichtman, E., Neubelt, M. J. and Harvey, G. T. (1993). Demonstration, using sliding-frequency guiding filters, of error free transmission over more than 20 Mm at 10 GBit/s, single channel, and over more than 13 Mm at 20 GBit/s in a two channel WDM. *Electron. Lett.*, **29**, pp. 910.
20. Harvey, G. T. and Mollenauer, L. F. (1993). Harmonically mode-locked fiber ring laser with an internal Fabry-Perot stabilizer for soliton transmission. *Optics Lett.*, **18**, pp. 107.
21. Olsson, N. A., Andrekson, P. A., Simpson, J. R., Tanbun-Ek, T., Logan, R. A and Wecht, K. W. (1990). Opt. Fiber Commun. Conf., San Francisco, PD6.
22. Ozyazici, M. S., Morton, P. A., Zhang, L. M., Mizrahi, V. (1995). Theoretical model of the hybrid soliton pulse source. *IEEE Photon. Tech. Lett.*, **7**, pp. 1142-1144.
23. Sayin, M. (1999). *Theoretical Model of the Mode-Locked Hybrid Soliton Pulse Source*. Ph. D. Thesis, University of Gaziantep, Gaziantep.
24. Pittoni, F., Gioannini M. and Montrosset, I. (2001). Time-domain analysis of fiber grating semiconductor laser operation in active mode-locking regime. *IEEE J. Select. Topics. Quantum Electron.*, **7**, no. 2, pp. 280-286.
25. Premaratne, M., Lowery, A. J., Ahmed, Z. and Novak, D. (1997). Modeling noise and modulation performance of fiber grating external cavity lasers. *IEEE J. Quantum Electron.*, **3**, no. 2, pp. 290-303.
26. Hill, K. O., Fujii, Y., Johnson, D. C. and Kawasaki, B. S. (1978). Photosensitivity in optical fiber waveguides: Application to reflection filter fabrication. *Appl. Phys. Lett.*, **32**, pp. 647-649.
27. Lemaire, P. J., Atkins, R. M., Mizrahi, V. and Reece, W. A. (1993). High pressure H<sub>2</sub> loading as a technique for achieving ultrahigh UV photosensitivity

- and thermal sensitivity in GeO<sub>2</sub> doped optical fibers. *Opt. Lett.*, **29**, pp. 1191-1193.
28. Meltz, G., Morey, W. W. and Glenn, W. H. (1989). Formation of Bragg gratings in optical fibers by a transverse holographic method. *Opt. Lett.*, **14**, pp. 823-825.
29. Hill, K. O. and Meltz, G. (1997). Fiber Bragg grating technology: Fundamentals and overview. *J. Lightwave Technol.*, **15**, pp. 1263-1276.
30. Asseh, A., Storoy, H., Sahlgren B. E, Sandgren, S. and Stubbe, R. (1997). A writing technique for long fiber Bragg gratings with complex reflectivity profiles. *J. Lightwave Technol.*, **15**, pp. 1419-1423.
31. Williams, J. A. R., Bennion, K. S. I. and Doran, N. J. (1997). Fiber dispersion compensation using a chirped in-fiber Bragg grating. *Electron. Lett.*, **30**, pp. 985-987.
32. Baumann, I., Seifert, J., Nowak, W. and Sauer, M. (1996). Compact all-fiber add-drop multiplexer using fiber Bragg gratings. *IEEE Photon. Technol. Lett.*, **8**, pp. 1331-1333.
33. Hjelm, D. R., Storoy, H. and Skaar, J. (OSA, 1998) in *Trends in Optics and Photonics Series*. pp. 280-284.
34. Kersey, A. D., Davis, M. A., Patrick, H. J., LeBlanc, M., Koo, K. P., Askins, C. G., Putnam, M. A. and Friebele, E. J. (1997). Fiber grating sensors. *J. Lightwave Technol.*, **15**, pp. 1442-1463.
35. Yariv, A. (1973). Coupled-mode theory for guided-wave optics", *IEEE J. Quantum Electron.*, **9**, pp. 919-933.
36. Kogelnik, H. (1976). Filter response of nonuniform almost-periodic structures. *Bell System Tech. J.*, **55**, pp. 109-126.

37. Yamada, M. and Sakuda, K. (1987). Analysis of almost-periodic distributed feedback slab waveguides via a fundamental matrix approach", *Appl. Optics*, **26**, pp. 3474-3478.
38. Kogelnik H. and Shank, C. V. (1972). Coupled-wave theory of distributed feedback lasers. *J. Appl. Phys.*, **43**, no. 5, pp. 2327-2335.
39. Kazarinov, R. and Henry, C. H. (1985). Second-order distributed feedback lasers with mode selection provided by first-order radiation losses. *IEEE J. Quantum Electron.*, **21**, no. 2, pp. 144-150.
40. McCall, S. L., and Platzman, P. M. (1985). An optimized  $\pi/2$  distributed feedback laser. *IEEE J. Quantum Electron.*, **21**, no. 12, pp. 1899-1904.
41. Glinski, J. and Makino, T. (1987). Yield analysis of second-order DSM DFB lasers and implications for design. *IEEE J. Quantum Electron.*, **23**, no. 6, pp. 849-859.
42. Kikuchi, K. and Tomofuji, H. (1990). Analysis of oscillation characteristics of separated-electrode DFB lasers diodes. *IEEE J. Quantum Electron.*, **26**, no. 10, pp. 1717-1727.
43. Vankwikelberge, P., Morthier, G. and Baets, R. (1990). CLADISS-A Longitudinal multimode model for the analysis of the static, dynamic, and stochastic behavior of diode lasers with distributed feedback. *IEEE J. Quantum Electron.*, **26**, no. 10, pp. 1728-1741.
44. Lowery, A. J. (1991). Integrated mode-locked laser design with a distributed-Bragg reflector. *IEE Proc.-J*, **138**, no. 1, pp. 39-46.
45. Zhang, L. M. and Carrol, J. E. (1992). Large-signal dynamic model of the DFB laser. *IEEE J. Quantum Electron.*, **28**, no. 3, pp. 604-611.
46. Zhang, L. M., Yu, S. F., Nowell, M. C., Marcenac, D. D., Carrol, J. E. and Plumb, R. G. S. (1994). Dynamic analysis of radiation and side-mode



- suppression in a second-order DFB laser using time-domain large-signal traveling wave model. *IEEE J. Quantum Electron.*, **30**, no. 6, pp. 1389-1395.
47. Zhang, L. M. and Carrol, J. E. (1994). Semiconductor 1.55  $\mu\text{m}$  laser source with gigabit/second integrated electroabsorptive modulator. *IEEE J. Quantum Electron.*, **30**, no. 11, pp. 2573-2577.
  48. Zhang, L. M. and Carrol, J. E. (1995). Dynamic response of colliding-pulse mode-locked quantum-well lasers. *IEEE J. Quantum Electron.*, **31**, no. 2, pp. 240-243.
  49. Erdogan, T. (1997). Fiber grating spectra. *J. Lightwave Technol.*, **15**, pp. 1277-1294.
  50. Mizrahi, V. and Sipe, J. E. (1993). Optical properties of photosensitive fiber phase gratings. *J. Lightwave Technol.*, **11**, pp. 1513-1517.
  51. Oulette, F., Cliche, J. and Gagnon, S. (1994). All-fiber devices for chromatic dispersion compensation based on chirped distributed resonant coupling. *J. Lightwave Technol.*, **12**, pp. 1728-1738.
  52. Carballar, A. and Muriel, M. A. (1997). Phase reconstruction from reflectivity in fiber Bragg gratings. *J. Lightwave Technol.*, **15**, pp. 1314-1322.
  53. Othonos, A. and Kalli, K. (1999). *Fiber Bragg Gratings*, Artech House, Boston.
  54. Kashyap, R., Swanton, A. and Arnes, D. J. (1996). Simple technique for apodising chirped and unchirped fibre Bragg gratings. *Electron. Lett.*, **32**, pp. 1226-1228.
  55. Tucker, R. S., Eisenstein, G. and Korotky, S. K. (1988). Optical time-division multiplexing for every high bit-rate transmission. *J. Lightwave Technol.*, **6**, pp. 1737.
  56. Valdmanis, J. A., Mourou, G. A. and Gabel, C. W. (1982). Picosecond electro-optic sampling system. *Appl. Phys. Lett.*, **41**, pp. 211.

57. Demokan, M. S. (1982). *Mode-locking in solid state and semiconductor lasers*, Research studies press, Chichester.
58. Eisenstein, G., Tucker, R. S., Koren, U. and Korotky, S. K. (1986). *IEEE J. Quantum Electron.*, **22**, pp. 142.
59. Tucker, R. S., Korotky, S. K., Eisenstein, G., Koren, U., Stulz, L. W. and Vesalka, J. J. (1985). *Electron. Lett.*, **21**, pp. 239.
60. Morton, P. A., Mizrahi, V., Kosinski, S. G., Mollenauer, L. F., Tanbun-Ek, T., Logan, R. A., Coblenz, D. L., Sargent, A. M. and Wecht, K. W. (1992). Hybrid soliton pulse source with fiber external cavity and Bragg reflector. *Electron. Lett.*, **28**, pp. 561-562.
61. Morton, P. A., Mizrahi, V., Tanbun-Ek, T., Logan, R. A., Lemaire, P., Presby, H. M., Erdogan, T., Woodward, S. L., Sipe, J. E., Philips, M. R., Sargent, A. M. and Wecht, K. W. (1994). Stable single mode hybrid laser with high power and narrow linewidth," *App. Phys. Lett.*, **64**, no. 20, pp. 2634-2636.
62. Tromborg, B., Lassen, H. E. and Olesen, H. (1994). Traveling wave analysis of semiconductor lasers: modulation responses, mode stability and quantum mechanical treatment of noise spectra. *IEEE J. Quantum Electron.*, **30**, no. 4, pp. 939-956.
63. McAdams, M., Provenzano, D., Peral, E. and Yariv, A. (1997). Effect of transmission through -fiber gratings on semiconductor laser intensity noise. *Appl. Phys. Lett.*, **71**, pp. 3341-3343.

## VITA

Nuran Dogru was born in Gaziantep in 1970. She was received her BSc and MSc degrees in electrical and electronics engineering from University of Gaziantep, Turkey, in 1994 and 1997, respectively. She has worked on her doctoral research in relative intensity noise of mode-locked hybrid soliton pulse sources where fiber Bragg gratings are used as external cavity. She has the following publications:

### Journals

1. Nuran Dogru and M. Sadettin Ozyazici (2002). Noise in mode-locked hybrid soliton pulse source. *Pakistan Journal of Applied Sciences*, 2, no. 1, pp. 74-76.
2. Nuran Dogru and M. Sadettin Ozyazici (2003). Effect of spontaneous noise on mode-locked fiber grating external cavity lasers. *Optical Engineering*, 42, no. 1, pp. 18-22. (Selected for the January 2003 issue of the *Virtual Journal of Ultrafast Science*)
3. Nuran Dogru and M. Sadettin Ozyazici (2003). Intensity noise of mode-locked fiber grating external cavity semiconductor lasers. *Optical and Quantum Electronics*, 35, no. 2, pp. 169-178.
4. Nuran Dogru and M. Sadettin Ozyazici (2003). Relative intensity noise of mode-locked fiber grating external cavity semiconductor lasers, *Optics and Laser Technology*, 35, no. 3, pp. 163-168.
5. Nuran Dogru and M. Sadettin Ozyazici (2003). Effect of intensity noise on mode-locked hybrid soliton pulse source, *Optics Communications*, 220, no.1-3, pp. 97-104.

## **International Conferences**

1. Nuran Dogru and M. Sadettin Ozyazici (2001). Relative intensity noise for mode-locked hybrid soliton pulse source. *International Conference on Electrical and Electronics Engineering (ELECO' 01)*, pp. 337-339, Bursa, Turkey, 7-11 November.
2. Nuran Dogru and Muhittin Sayin (2001). Effect of noise on mode-locked hybrid soliton pulse source. *International Conference on Electrical and Electronics Engineering (ELECO' 01)*, pp. 349-351, Bursa, Turkey, 7-11 November.
3. Nuran Dogru and M. Sadettin Ozyazici (2001). Noise in mode-locked hybrid soliton pulse source. *International Symposium on High Performance Electron Devices For Microwave & Optoelectronic Applications (EDM0' 01)*, Vienna, Austria, 15-16 November, pp. 49-54.
4. Nuran Dogru and M. Sadettin Ozyazici (2001). Noise in mode-locked hybrid soliton pulse source. *Australasian Conference on Optics, Lasers, and Spectroscopy (ACOLS' 01)*, Queensland, Australia, 3-6 December, pp. T29 139.
5. Nuran Dogru and M. Sadettin Ozyazici (2002). Effect of spontaneous noise on mode-locked hybrid soliton pulse source utilizing chirped grating. *International Conference on Indium Phosphide and Related Materials (IPRM' 02)*, Stockholm, Sweden, 12-16 May, PI-44 pp. 265-268.
6. Nuran Dogru and Muhittin Sayin (2002). Mode-locked and noise characteristics of fiber grating semiconductor laser. *International Congress on Laser Advanced Materials Processing (LAMP 2002)*, Proc. of SPIE, vol. 4830, Osaka, Japan, 27-31 May, pp.357-360.
7. Nuran Dogru and M. Sadettin Ozyazici (2002). Mode-locked and noise analysis of external cavity semiconductor lasers. *International Conference on Applications of Photonics Technology (ICAPT' 02)-Photonics North 2002*, Proc. of SPIE, vol. 4833, Quebec City, Canada, 2-6 June, pp. 915-921.

8. Nuran Dogru and M. Sadettin Ozyazici (2002). Spontaneous and carrier noise in mode-locked hybrid soliton pulse source. *International Workshops on Laser and Fiber-Optical Networks Modeling (LFNM' 02)*, Kharkiv, Ukraina, 3-5 June, pp. 5-7.
9. Nuran Dogru and M. Sadettin Ozyazici (2002). Relative intensity noise in mode-locked fiber grating external cavity laser. *Workshop on Fiber and Optical Passive Components (WFOPC' 02)*, Glasgow, Scotland, 5-6 June, pp. 104-108.
10. Nuran Dogru and M. Sadettin Ozyazici (2002). Spontaneous and carrier noise in mode-locked lasers. *Optoelectronics and Communications Conference (OECC' 02)*, Pacifico Yokohama, Yokohama Kanagawa, Japan, 8-12 July, 10P-65 pp. 316-317.
11. Nuran Dogru and Muhittin Sayin (2002). Mode-locked and noise characteristics of hybrid soliton pulse source utilizing uniform grating. *International Symposium on Optical Science and Technology SPIE' s Annual Meeting-Diode Laser and Applications in Atmospheric Sensing*, Proc. of SPIE, vol. 4817, Seattle, Washington USA, 7-11 July, pp. 241-248.
12. Nuran Dogru and M. Sadettin Ozyazici (2002). Noise analysis for mode-locked lasers. *General Assembly of URSI- International Union of Radio Science*, Maastricht, Netherlands, 17-24 August, CD-ROM, Commission D, p.54-paper no.92.
13. Nuran Dogru and M. Sadettin Ozyazici (2002). Carrier noise in mode-locked external cavity lasers. *Congress of the International Commission for Optics (ICO-19' 02)*, Proc. of SPIE, vol. 4829, Firenze, Italy, 25-30 August, pp. 657-658.
14. Nuran Dogru and M. Sadettin Ozyazici (2002). Carrier noise in mode-locked fiber grating external cavity lasers. *International Coonference on Advanced Semiconductor Devices and Microsystems (ASDAM' 02)*, Smolenice Castle, Slovakia, 14-16 October, pp.247-250.

15. Nuran Dogru and M. Sadettin Ozyazici (2002). Noise characteristics of mode-locked hybrid soliton pulse source. *International Conference on Optics-Photonics Design & Fabrication (ODF' 02)*, Tokyo, Japan, 30 October-1 November, pp.101-102.
16. Nuran Dogru and M. Sadettin Ozyazici (2002). Intensity noise reduction in mode-locked hybrid soliton pulse source. *International Conference on Optics-Photonics Design & Fabrication (ODF' 02)*, Tokyo, Japan, 30 October-1 November, pp.103-104.

### **National Conferences**

1. Nuran Dogru ve M. Sadettin Ozyazici (2001). Mod kilitli düzgün fiber ızgaralı lazerin bağıl şiddet gürültüsü. *Elektrik-Elektronik-Bilgisayar Mühendisliği 9. Ulusal Kongresi*, 2, pp. 449-451, Kocaeli, September.
2. Nuran Dogru ve M. Sadettin Ozyazici (2002). Mod kilitli karışık soliton darbe kaynağının bağıl şiddet gürültüsü. *URSI- Union Radio Science International 1. Ulusal Kongresi*, pp. 226-229, Istanbul, 18-20 September.
3. Nuran Dogru (2002). Gürültünün mod-kilitli lazerlere etkisi. *URSI- Union Radio Science International 1. Ulusal Kongresi*, pp. 230-233, Istanbul, 18-20 September.
4. Nuran Dogru ve M. Sadettin Ozyazici (2002). Spontane gürültünün mod kilitli doğrusal azalan adımlı Gaussian pozlu fiber ızgaralara etkisi. *Elektrik-Elektronik-Bilgisayar Mühendisliği Sempozyumu (ELECO' 02)*, Elektronik, pp. 299-301, Bursa, December.
5. Nuran Dogru ve M. Sadettin Ozyazici (2002). Mod-kilitli dış boşluklu lazerlerde taşıyıcı gürültü. *Elektrik-Elektronik-Bilgisayar Mühendisliği Sempozyumu (ELECO' 02)*, Elektronik, pp. 302-304, Bursa, December.

### **Awards**

1. Young Scientist Award of 27 th General Assembly of URSI-International Union of Radio Science, Maastricht, Netherlands, 2002.